3-11-2011

Investigation of YAG:Ce Scintillating Fiber Properties Using Silicon Photomultipliers

Bradley S. Jones

INVESTIGATION OF YAG:CE SCINTILLATING FIBER PROPERTIES USING SILICON PHOTOMULTIPLIERS

THESIS

Bradley S. Jones, 1st Lieutenant, USAF

AFIT/GNE/ENP/11-M11

DEPARTMENT OF THE AIR FORCE
AIR UNIVERSITY

AIR FORCE INSTITUTE OF TECHNOLOGY

Wright-Patterson Air Force Base, Ohio

AFIT/GNE/ENP/11-M11

INVESTIGATION OF YAG:CE SCINTILLATING FIBER PROPERTIES USING SILICON PHOTOMULTIPLIERS

THESIS

Presented to the Faculty

Department of Engineering Physics

Graduate School of Engineering and Management

Air Force Institute of Technology

Air University

Air Education and Training Command

In Partial Fulfillment of the Requirements for the

Degree of Master of Science in Nuclear Engineering

Bradley S. Jones, BS

1st Lieutenant, USAF

March 2011

AFIT/GNE/ENP/11-M11

INVESTIGATION OF YAG:CE SCINTILLATING FIBER PROPERTIES USING SILICON PHOTOMULTIPLIERS

Bradley S. Jones, BS

1st Lieutenant, USAF

Approved:

_____	_____
Maj Benjamin R. Kowash (Chairman)	Date
_____	_____
Lt Col Michael R. Hawks (Member)	Date
_____	_____
Abigail Bickley, PhD (Member)	Date

Abstract

The properties of thin, cerium activated, yttrium aluminum garnet (YAG:Ce), scintillating fiber-shaped crystals were investigated for particle tracking and calorimetric applications such as Compton imaging of Special Nuclear Material from remote platforms at standoff ranges. Silicon photomultipliers (SiPMs) are relatively new, efficient, single photon sensitive, solid-state photodiode arrays which are well suited for the readout of scintillating fibers. Using SiPMs, the scintillation decay time profiles of six 400 μm YAG:Ce fiber crystals were measured under alpha and gamma irradiation. Interestingly, the observed decay times in the thin fibers were substantially slower than values for bulk single crystal YAG:Ce reported in open scientific literature; possible explanations are explored. Both laser induced photoluminescence and alpha scintillation measurements were conducted to estimate the effective attenuation length of the YAG:Ce fibers. Using the measured attenuation lengths, position-of-interaction measurements were conducted to determine the achievable position resolution in YAG:Ce fibers using dual fiber end SiPM readouts. The measured results are compared to theoretical calculations and Monte Carlo simulations. Finally, improvements to the detector concept, including a formula to determine the best SiPM model based on device parameters and the Birks' figure of merit of the scintillating material, are presented.

Acknowledgements

First and foremost, I acknowledge the enormous privilege afforded me by my fellow countrymen who provided me with a world-class education; I pray that with it, I will serve you well. To the countless teachers, professors, and mentors who have presented me with the tools, challenges, and opportunities required to reach new potentials, I am truly indebted and forever grateful for your dedication, patience, and perseverance! Special thanks to the diligent professionals at the AFIT Model Shop, AFRL RX, and AFIT ENV laboratory; without their many hours of assistance this work would not have been possible. Thank you to my advisors, classmates, and friends at AFIT who have provided endless support. Finally, to my beautiful wife and wonderful son, your love is my sanctuary; I love you both very much!

-Bradley S. Jones

Table of Contents

Page

Abstract iv

Acknowledgements v

Table of Contents vi

List of Figures ix

List of Tables xix

List of Abbreviations xx

I. Introduction and Motivation 1

1. Objectives 3
2. Thesis Outline 3

II. Theory and Background 4

1. Compton Imaging 4

1. 1. Compton Scattering 5
1. 2. Compton Camera Directionality 7

2. Radiation Detection Using Scintillators 10

2. 1. Inorganic Scintillation Mechanisms 11
2. 2. Intrinsic Luminescence of Inorganic Scintillators 12
2. 3. Extrinsic Luminescence of Activated Inorganic Scintillators 13
2. 4. Light Yield of Inorganic Scintillators 14
2. 5. Scintillation Kinematics 16
2. 6. Photon Transport in Scintillators 18
2. 7. Physicochemical Properties of Inorganic Scintillators 23

3. Scintillating Fibers 23

3. 1. Light Formation and Propagation in Scintillating Fibers 24
3. 2. Estimating Energy and Position Resolution in Scintillating Fibers 31

4. Scintillator Materials Under Study 35

4. 1. Properties of Rare Earth Garnet Crystals 36

Page

4. 2. Properties of the YAG:Ce Scintillator 37
4. 3. Properties of Fiber Shaped YAG:Ce 46

5. Photon Detection Techniques 49

5. 1. Silicon Photomultipliers 50
5. 2. SiPM Photon Detection Efficiency 55
5. 3. SiPM Response Linearity 56
5. 4. Dark Counts, After pulses, and Cross-talk 57
5. 5. SiPM Amplitude Resolution Limitations 58

III. Experiments 64

1. Multi-Pixel Photon Counter Investigation 64

1. 1. MPPC Readout Circuit 65
1. 2. MPPC Readout Circuit Modeling and Simulation 66
1. 3. MPPC Calibration 69
1. 4. MPPC Scintillator Response Experiment and Simulation 71

2. YAG:Ce Fiber Crystal Investigation 74

2. 1. YAG:Ce Scintillation Properties Investigation 77
2. 2. YAG:Ce Energy Spectrum and Resolution Measurements 78
2. 3. YAG:Ce Position Resolution Measurements and Simulations 79

IV. Results and Analysis 86

1. MPPC Findings 86

1. 1. MPPC Breakdown Voltages and Cross-talk 86
1. 2. MPPC Pixel Gains 89
1. 3. MPPC Response to Scintillation 93

2. YAG:Ce Fiber Findings 99

2. 1. YAG:Ce Scintillation Properties 99
2. 2. YAG:Ce Energy Spectrum and Resolution Results 106
2. 3. YAG:Ce Fiber Photoluminescence Position Resolution Results 118
2. 4. YAG:Ce Fiber Scintillation Position Resolution Results 128
2. 5. Improving System Resolution 146

V. Conclusion, Summary, and Recommendations 155

Page

Appendix.....159

A1. LYSO:Ce DETECT2000 Code 160

A2. YAG:Ce DETECT2000 Code 161

A3. YAG:Ce Stopping and Range of Ions in Matter (SRIM) 162

A4. Source Beam Width Calculations.....164

A5. MCNP5 Code 165

A6. YAG:Ce Alpha Decay Profile Data.....167

Bibliography 171

List of Figures

Figure Page

1. Compton scatter angle and back projection illustration. When energy and interaction position information of a Compton scatter event is known, the scatter angle can be computed by (2.1). The source of the gamma ray is known to exist on the periphery of a cone about θ. As more observations are made, more conic frustums accumulate on a back-projected source plane to form an image. Correlated measurements result in intersections of these conic frustums which appear as bright pixels, representing the source location. 6

2. The differential scattering cross-sections as a function of angle are given by the Klein-Nishina formula, shown here for a Z=32 target at various gamma ray energies in the regime of interest. It is noteworthy that higher energy photons tend to preferentially scatter in a forward direction. This phenomenon can be exploited when designing the Compton camera for a standoff application. 9

3. A conceptual illustration of a fiber bundle Compton camera is shown. High energy gamma rays preferentially forward scatter, in accordance with the Klein-Nishina formula. Thus, directivity is gained by effectively increasing gamma path length in bulk detector material along the fiber axis. Notice how the hypothetical cosmic gamma ray passes through the detector without interacting while the source gamma ray Compton scatters and absorbs in two different scintillating fibers. 10

4. A generic band diagram of an inorganic crystal scintillator is illustrated. The electrons and holes can annihilate via at activator or self-trapped exciton (STE) sites which are responsible for the extrinsic and intrinsic luminescence, respectively, of the crystal. 12

5. The absorption or excitation (orange) and emission (red) properties of single crystal fiber YAG:Ce is shown. The overlap of emission and absorption curves indicates self-absorption. The data shown is adapted from [21]. 19

6. Fresnel reflections are shown for a typical inorganic scintillator interfacing with glass (top) and air (bottom). Notice the critical angles are shown as asymptotes. While glass interfaces result in nearly negligible Fresnel reflections for much of the angular spectrum, air interfaces have a minimum reflection intensity in excess of 8%. 22

7. Cross-sectional view of a scintillating fiber illustrates the effects of photon trapping and escape due to internal reflections. Mentally rotating the 2-D image 2π about the fiber axis gives the full picture. Note that refractions are not drawn to scale for illustrative purposes. 26

8. The effect of index matching fluid, n_1, on the escape efficiency of light trapped in a scintillating fiber, n_0. Recall that the maximum escape efficiency for a single fiber end is 50% of the total *trapped* light. 28

9. The results of a scintillation event in a bundle of organic fibers modeled in GEANT4 [26] are shown. Green tracks represent primary ionizing radiation. Red tracks are secondary electrons which produce yellow scintillation photons. This also shows the efficacy of Compton recoil electron tracks being observed in neighboring organic scintillating fibers. 30

10. Double end fiber readout parameters are illustrated. The position of interaction occurs at a distance x from end #1 and a position l -x from end #2. The resulting light yields are N1 and N2, respectively. 33

11. YAG:Ce energy level diagram adapted from [20]. 39

12. Data adapted from Chewpraditkul illustrating the superior achievable energy resolution of YAG:Ce to a brighter scintillator, LYSO:Ce [34]. 42

13. Data from Chewpraditkul illustrating the intrinsic resolution of YAG:Ce [34]. 43

14. The fast electron stopping powers in YAG:Ce calculated using the Bethe-Bloch is plotted over the energy regime of interest. 45

15. The ranges of fast electrons in YAG:Ce calculated using the Bethe-Bloch formula is plotted over the energy regime of interest. The range values show good agreement and provide an expected range of tens to hundreds of microns for typical Compton recoil electrons. 45

16. Radial concentration of cerium dopant atoms in YAG crystals grown by µ-PD. Data adapted from [39]. 47

17. Independent results confirming the concave radial distribution cerium dopant atoms in YAG crystals grown by µ-PD. Image adapted from [21]. No absolute, quantitative values of concentration were reported. 48

18. Confocal photoluminescence spectroscopy results of cerium activator radial concentration in LuAG:Ce fibers as presented by Dujardin, *et al.*, are shown [40] 49

19. The spectral response of a photodiode is superior to that of a PMT. Even a bialkali PMT is poorly matched to the emission spectrum of YAG:Ce, peaked at 550 nm. Figure adapted from [8]. 50

20. Readout circuit of a Geiger-mode APD is shown; image is adapted from [4]. V_a is the bias voltage, R_L is the ballast resistor, R_S is the load resistor across which V_{out} is measured. 51

21. Circuit model of a passively quenched G-APD is shown with substrate and storage capacitances. The image is adapted from [44]. Here, the diode

array is modeled as a current source using the diode breakdown voltage, V_{br}, and the resistance, $R_{D,Nf}$, in series. The capacitors are the stray capacitances associate with the diode substrate. 52

22. Hamamatsu Multi-Pixel Photon Counter is a trademarked line of 1x1 mm SiPMs with APD pixel densities ranging from 100-1600 mm^{-2}. Hamamatsu claims timing resolutions of 200-500 ps, gain factors up to $2*10^6$, and photon detection efficiency of 25-65% depending on model [45]. 53

23. Sensl's Scalable Silicon Photomultiplier Arrays are constructed using 4x4 individual SiPMs. These devices are conveniently designed for scalability. The Sensl SPMMatrix (not shown) is a prefabricated, fully electronically integrated, commercially available 16x16 SiPM array with 256 analog channels [46]. 54

24. Passive circuit model for a Hamamatsu S10362-11-02C, adapted from [42]. For details, the reader is refered to [42]. 55

25. The number of pixels which fire is a non-linear function of the number of photons incident upon the SiPM. Higher pixel densities offer greater dynamic ranges and less saturation. 57

26. The overall intrinsic resolution (FWHM) of an ideal SiPM is graphed as a function of the mean number of photoelectrons produced per pixel, shown here for a SiPM with 1600 pixels. Poisson statistics dominate the resolution limit when σ_N / N is large. While relative dispersion due to Poisson statistics improves at higher photon fluxes, eventually the SiPM becomes saturated and the dominating source of signal dispersion and degraded resolution. 60

27. The overall intrinsic resolutions (FWHM) of SiPMs with various array sizes are shown. Interestingly, the minimum resolution is independent of the mean number of photoelectrons, thus the number of incident photons. However, minimum resolution improves as the square root of the number of pixels. 61

28. The Hamamatsu model S10362-025C MPPC is shown. The photosensitive area in the center of the ceramic package is 1x1 mm^2, contains 1600 active G-APD pixels, and lies underneath a layer of protective optical epoxy. 65

29. The MPPC readout circuit used during the experiments is shown. The MPPC is typically biased a few volts above breakdown, nominally 71-72 V. 66

30. The passive circuit model of an MPPC first developed by Wangerin, *et al.*, has been expanded as shown. Additional features include scalable and selectable parameterized component values which allow modeling pixel

firing across the dynamic range of the device as well as the capability to model repetitive pixel firings or after pulses. 67

31. The simulated response of a single pixel within a MPPC firing is shown. The maximum amplitude is less than the noise floor of the Tektronix DPO7104 oscilloscope. 69

32. The dark count pulse height spectrum from MPPC#1 is shown at four different bias voltages. There are three distinct sets of peaks which correspond to the single, two, and three pixel events which result from dark counts and pixel cross-talk. The cross-talk probability and pixel gain clearly increases with bias voltage. 71

33. A typical digitized LYSO:Ce gamma scintillation pulse as measured directly using the MPPC readout circuit and 1GSa/s oscilloscope is shown. 72

34. The custom manufactured MPPC and YAG:Ce fiber vice mount is illustrated 75

35. Photograph of the photoluminescence experimental setup. 81

36. A 973x SEM image of a YAG:Ce fiber shows surface imperfections such as micro bubbles, protrusions, and pits. 82

37. An illustration of the YAG:Ce position resolution experimental setup using a collimated alpha source is shown. 83

38. MPPC#2 dark count pulse height spectrum is shown for four bias voltages. The amplitude of the pulses is linearly dependent on excess bias. As shown, cross-talk probability increases with bias voltage. 87

39. The single pixel response amplitude of MPPC#1(left) and MPPC#2 (right) as a function bias voltage. The breakdown voltage determined by the x-intercept is 68.6 V and 68.9V, respectively. The error bars are the standard deviation of the measured single pixel response data. 88

40. Single pixel cross-talk probabilities are plotted versus bias voltage for both MPPCs. The error bars give the uncertainty due to counting statistics. 89

41. The simulated waveform of a single pixel firing event is shown compared to the measured response of 25 of single pixel waveforms (and their mean) from MPPC#1 at 73 V bias. 91

42. MPPC response of LYSO:Ce scintillation pulses due ^{22}Na gamma irradiation is shown. The waveforms are measured directly from the MPPC readout without any amplification. Only the largest pulses were used to analyze the time decay of the scintillator to minimize jitter from amplitude walk. 94

43. LYSO:Ce scintillation decay curve as measured by the MPPC is shown normalized. The decay time constant is determined by the negative

inverse of the slope of the exponential fit reported by ROOT [56], an open source C++ data analysis toolkit. A single exponential decay with a 47.1 ns time constant (black line) provides an excellent fit to the measured data (black dots)..... 94

44. MPPC pulse height spectrum of LYSO:Ce in response to ^{22}Na γ radiation in terms of approximate number of pixels firing. The 511 keV photopeak is centered near 240 pixels. The gap in the Compton continuum is due to the high threshold value set to discriminate dark counts. The events at the very left are due to dark counts or spurious trigger events. 96

45. A fully simulated 511 keV LYSO:Ce scintillation waveform is shown compared to a 511 keV LYSO:Ce scintillation waveform measured by an MPPC. 98

46. A fully simulated 511 keV LYSO:Ce scintillation MPPC waveform is compared to the mean of 25,000 measured 511 keV scintillation MPPC waveforms. 99

47. The fluorescence decay profile measurements for six YAG:Ce fibers are shown after summing and normalizing over hundreds of scintillation pulses. The tails show slightly differing decay times. 100

48. The fluorescence time decay profile of YAG:Ce fiber F6 under gamma excitation is shown compared to alpha excitation. Interestingly, the fast and slow decay constants are nearly identical for both gamma and alpha excitation, but the intensities flip. 102

49. A fully simulated 5.4 MeV alpha scintillation waveform in a YAG:Ce fiber as readout using an MPPC is compared to a measured event waveform. 105

50. A fully simulated 5.4 MeV alpha scintillation waveform in a YAG:Ce fiber as readout using an MPPC is compared to the mean of 8,000 measured waveforms. 105

51. ^{22}Na gamma energy spectrum using MPPC readout, NIM spectroscopy electronics, and a YAG:Ce scintillating fiber. Noise integration can be seen near Channel 75 indicating very noisy electronics. A feature resembling a Compton edge appears around Channel 200. 106

52. ^{241}Am alpha spectrum shown using the same readout and settings as the ^{22}Na spectrum in Fig. 51. Noise integration can be seen around Channel 75 indicating very noisy electronics. The alpha peak appears around Channel #667. 107

53. The gamma energy spectra of a YAG fiber simulated using MCNP5 are shown for beams of monoenergetic 511 keV and 2.6 MeV gamma rays at two angles of incidence. Side illumination means the beam was incident

orthogonal to the fiber axis. End illumination means the beam incidence was along the fiber axis. The reported efficiencies are the total number of interactions out of the 100 million incident gamma particles. 109

54. An image of a 100 µm thick cross-sectional slice of YAG:Ce fiber taken using a UV microscope is shown. The radial dispersion of the cerium activator is evident by the increase in luminous intensity at the rim of the fiber. The dark spots are most likely carbon deposits from the diamond saw blade used to cut the fiber. 111

55. The green channel from an image of a YAG:Ce fiber cross-section under UV fluorescence is shown on the left. On the right, the channel intensity is shown as a function of radial position for the three different diameter vectors shown in blue, red, and magenta. Notice that the CCD's 8-bit ADC is saturated even at the lowest UV illumination setting. 112

56. Intensity data from YAG:Ce fluorescence has been linearly transformed and normalized (to 0.1 at.%) to indicate relative cerium activator concentration (left). The spike at 50 µm in magenta is from a deposit of material, see Fig. 55. The data is comparable to that shown by Dujardin, *et al.*, in [40] for 0.1 at.% cerium doped LuAG:Ce (right). 113

57. Electron trajectory results from CASINO v2.42 simulations of 1000, 340 keV electrons in bulk YAG:Ce are shown. Red tracks are events which backscatter and eventually escape the sample, while blue tracks show full energy deposition events. The results agree nicely with 100-200 µm range for 340 keV electrons in YAG:Ce calculated using the Bethe-Bloch formula and presented in Fig. 15. 115

58. Energy deposition distribution from CASINO v2.42 simulations of 340 keV electrons in bulk YAG:Ce is shown. 115

59. Electron trajectory results from CASINO v2.42 simulations of 1000, 2360 keV electrons in bulk YAG:Ce are shown. Red tracks are events which backscatter and eventually escape the sample, while yellow (high energy electron) and blue (down scattered, low energy electron) tracks show full energy deposition events. The results agree nicely with the ~1-2 mm range for 2360 keV electrons in YAG:Ce calculated using the Bethe-Bloch formula and presented in Fig. 15. 116

60. Energy deposition distribution from CASINO v2.42 simulations of 2360 keV electrons in bulk YAG:Ce is shown. 116

61. The attenuation length of F1 can be determined by the slope of the line of $\log\left(\overline{N}_2 / \overline{N}_1\right)$ vs. interaction position. The measurements were repeated five times for each fiber. The slope of the lines should be the same for a given attenuation length. Repeatability of optical coupling is measured by the y-intercept. The error bars are computed by (4.4). 120

62. Damage done to the acrylic window of MPPC#2 by over-tightening in the vice mount is shown. Extreme caution should be applied when handling the photosensitive surfaces of the MPPCs. The acrylic is soft and easily cracks and scratches; it is not intended for pressure coupling with extremely hard surfaces such as thin garnet crystals. 121

63. Using measured attenuation length data, the photoluminescence position-of-interaction in F1 can be estimated. The error bars on the blue dots represent the position resolution (i.e. sample standard deviation) at that point. The red squares represent the true position-of-interaction. The size of the red squares is equal to the FWHM of the laser beam, 2.6 mm. 123

64. The plot of $\log(N_2 / N_1)$ is not a straight line for F2. Shown are five independent and repeatable measurements. The exponential attenuation model does not provide an accurate description of the light propagation in F2. The error bars are computed by (4.4). R^2 is the coefficient of determination calculated by the square of the correlation coefficient. R^2 = 0.848 indicates a poor linear fit. 124

65. Using an exponential attenuation model provides a poor reconstruction of the position-of-interaction in F2. The response is suspected to be due to a local imperfection near x=30 mm which causes disproportionate distribution of light intensity at the fiber end readouts due to reflection or absorption. The average χ^2 goodness-of-fit statistic is over 40 times higher than in F1 as shown in Fig. 63, indicating very poor position estimates. 125

66. Fiber F3 shows a position-of-interaction reconstruction slightly better than that of F1 as evidenced by the average χ^2=2.18. The size of the red squares is equal to the FWHM of the laser beam, 2.6 mm. 126

67. The position-of-interaction reconstruction of F4, while better than F2, suffers from bias due to the faulty assumption that light propagation within the fiber follows an exponential attenuation model. The red squares represent the true position-of-interaction. The size of the red squares is equal to the FWHM of the laser beam, 2.6 mm. 126

68. Fiber F5 generally follows the exponential attenuation model for reconstructing position-of-interaction. The goodness-of-fit is better than F2 and F4, but not as good as either F1 or F3. The error bars on blue dots represent the position resolution at that point. The red squares represent the true position-of-interaction. The size of the red squares is equal to the FWHM of the laser beam, 2.6 mm. 127

69. The mean number of simulated MPPC pixels firing is shown as a function of interaction location along a YAG:Ce fiber with an attenuation length of 10 cm. The error bars indicate the standard deviation of the number of pixels based on counting statistics. 129

70. The mean number of simulated MPPC pixels firing is shown as a function of interaction location along a YAG:Ce fiber with an attenuation length of 20 cm. The error bars indicate the standard deviation of the number of pixels based on counting statistics. 130

71. The mean number of simulated MPPC pixels firing is shown as a function of interaction location along a YAG:Ce fiber with an attenuation length of 30 cm. The error bars indicate the standard deviation of the number of pixels based on counting statistics. 130

72. Simulated results of the position-of-interaction reconstruction using a Monte Carlo method to model the stochastic process of MPPC pixels firing are shown for three crystals of different attenuation lengths. In aggregate, the simulated results accurately reconstruct the position-of-interaction. The spread in data is due solely to the random nature of the MPPC response, in accordance with binomial statistics. The different colors are associated with the different attenuation lengths of the crystals: blue is 10 cm, red 20cm, and green 30 cm. 132

73. The simulated position-of-interaction reconstruction data from the 30 cm attenuation is shown as a histogram. The different colors indicate different true positions-of-interaction. The spread in the data (i.e. the standard deviation) is the ideal position resolution..... 132

74. Ideal position resolution of a 1 MeV (gamma equivalent) scintillation pulse in three YAG:Ce fibers of different attenuation lengths using dual fiber end MPPC readout is shown. The lines represent the analytical position resolution which is described by (2.21). The squares represent the results of Monte Carlo simulations of the MPPC pixel firing process given a simulated scintillation photon flux modeled in DETECT2000..... 133

75. Ideal energy resolution of a 1 MeV (gamma equivalent) scintillation pulse in three YAG:Ce fibers of different attenuation lengths using dual fiber end MPPC readout is shown. The lines represent the analytical energy resolution which is described by (2.19). The squares represent the results of Monte Carlo simulations of the MPPC pixel firing process given a simulated scintillation photon flux modeled in DETECT2000. 134

76. The mean number of MPPC pixels firing in response to alpha scintillation in F1. The error bars represent the standard deviation of the measured pixel response data. It is important to recall that low energy events are not discriminated in the collection or processing of these data. The lack of symmetry is due to the damaged, less efficient MPPC#2..... 136

77. The reconstruction of alpha particle position-of-interaction within F1 is shown. The blue circles are the mean of the position-of-interaction estimates using (2.13) with position resolution as error bars. The red

squares represent true source positions; the size of the squares is equal to the 2.4 mm beam width of the collimated alpha source. 138

78. The discrepancy between the light propagation in F2 and the expected exponential attenuation which was observed in the photoluminescence experiments is repeatable in the scintillation experiment. Here, the fiber has been flipped so the disjoint due to suspected optical defects is observed by the change in slope near 70 mm rather than 30 mm. The defective fiber is on the side closest to the damaged MPPC#2 resulting in low numbers of fired pixels and consequently terrible position resolution. 139

79. The accuracy and resolution of the alpha position-of-interaction reconstruction in F2 is very poor due to the low number of fired MPPC pixels. Additionally, the light propagation discrepancy observed for F2 during the photoluminescence experiments is again observed in scintillation experiments and is responsible for the over 10 times worse χ^2 compared to F1. 140

80. The reconstruction of the alpha particle position-of-interaction within F3 is shown. The blue circles are the mean of the position-of-interaction estimates using (2.13) with position resolution as error bars. The red squares represent true source positions; the size of the squares is equal to the 2.4 mm beam width of the collimated alpha source. 140

81. The reconstruction of the alpha particle position-of-interaction within F4 is shown. The blue circles are the mean of the position-of-interaction estimates using (2.13) with position resolution as error bars. The red squares represent true source positions; the size of the squares is equal to the 2.4 mm beam width of the collimated alpha source. 141

82. The reconstruction of alpha particle position-of-interaction within F5 is shown. The blue circles are the mean of the position-of-interaction estimates using (2.13) with position resolution as error bars. The red squares represent true source positions; the size of the squares is equal to the 2.4 mm beam width of the collimated alpha source. 141

83. The poor optical coupling of the scintillator and MPPC and the damage to MPPC#2 was simulated and compared to the measured MPPC response. The photon detection efficiencies of MPPC#1 and MPPC#2 were reduced from 15% to 11% and 9%, respectively. Only the means of the measured data are shown; the data are presented without error bars for clarity. The error bars can be found in Fig. 76. 145

84. The position resolution of the asymmetric simulation is shown with an excess noise factor of 1.7, chosen to match the measured position resolution of F1. 145

85. The number of simulated pixels which fire using the more efficient S10362-11-100C 100 pixel Hamamatsu MPPC is drastically increased over the 1600 pixel MPPC used in this research when coupled to a YAG:Ce fiber with a simulated attenuation length of 10 cm. 147

86. The achievable position resolution of a 1-MeV (gamma equivalent) scintillation event in a YAG:Ce fiber is significantly improved when readout using a more efficient 100 pixel MPPC as opposed to the inefficient 1600 pixel MPPC used in this research. Any effects of saturation are ignored. Lines indicate the analytical solution and squares indicate the results of Monte Carlo simulations. 148

87. The achievable energy resolution of a 1-MeV (gamma equivalent) scintillation event in a YAG:Ce fiber is significantly improved when readout using a more efficient 100 pixel MPPC as opposed to the 1600 pixel MPPC used in this research. Any effects of saturation are ignored. Lines indicate the analytical solution and squares indicate the results of Monte Carlo simulations. 148

88. The intrinsic amplitude resolutions of the 100, 400, and 1600 pixel MPPCs in response to a 1 MeV (gamma equivalent) scintillation event in a 400 µm diameter YAG:Ce fiber were computed using (2.28) and are shown from top to bottom. The contribution from saturation is R_0 while the contribution from counting statistics is Rstat. Note that the resolution values are reported as $\left(\sigma_E / E\right) = R_{FWHM} / 2.35$, not the FWHM. 150

89. The intrinsic amplitude resolutions of the 100 MPPC in response to a 1 MeV (gamma equivalent) scintillation event in 400 µm and 1 mm diameter YAG:Ce fibers were computed using (2.28). The top plot shows the effect from saturation resulting from fewer available pixels due to the surface area mismatch between a 400 µm fiber to a 1 mm^2 MPPC. The bottom plot shows the improvement of matching scintillator and MPPC areas. The contribution from saturation is R_0 while the contribution from counting statistics is Rstat. Note that the resolution values are reported as $\left(\sigma_E / E\right) = R_{FWHM} / 2.35$, not the FWHM. 152

List of Tables

Table Page

1. Scintillation Properties of YAG:Ce from [30] and [32] 38

2. Temperature dependent decay kinetics of YAG:Ce as reported in [20].....41

3. Alpha Particle Scintillation Decay Properties of YAG:Ce Fibers 100

4. Attenuation lengths and position resolution of five YAG:Ce fibers measured using 405 nm laser induced photoluminescence 123

5. Attenuation lengths and position resolutions measured in five YAG:Ce fibers using scintillation from a 5.4 MeV alpha source 138

List of Abbreviations

µ-PD	Micro-Pulling-Down crystal growth method
ADC	Analog-to-Digital Converter
APD	Avalanche Photodiode
CCD	Charge Coupled Device
COMPTEL	Imaging Compton Telescope
CMOS	Complementary Metal-Oxide Semiconductor
FWHM	Full Width at Half Maximum
G-APD	Geiger mode Avalanche Photodiode
GEANT4	Geometry And Tracking simulation toolkit, version 4
GdYAG	Gadolinium Yttrium Aluminum Garnet crystal
GSO	Gadolinium Oxyorthosilicate crystal
HPGe	High Purity Germanium diode
KS-Test	Kolmogorov-Smirnov Test
LuAG	Lutetium Aluminum Garnet crystal
LuAP	Lutetium Aluminum Perovskite crystal
LSO	Lutetium Oxyorthosilicate crystal
LYSO	Lutetium Yttrium Oxyorthosilicate crystal
MCNP5	Monte Carlo N-Particle code version 5
MEGA	Medium Energy Gamma-ray Astronomy telescope
MPPC	Multi-Pixel Photon Counter, trademark by Hamamatsu
NIM	Nuclear Instrumentation Module
NIST	National Institute for Standards and Technology
PCB	Printed Circuit Board
PDE	Photon Detection Efficiency
QE	Quantum Efficiency
SEM	Scanning Electron Microscope
SiPM	Silicon Photomultiplier
SNM	Special Nuclear Material
SPECT	Single Photon Emission Computed Tomography
TCP/IP	Transmission Control Protocol
YAG	Yttrium Aluminum Garnet crystal
YAP	Yttrium Aluminum Perovskite crystal
YSO	Yttrium Oxyorthosilicate crystal

Investigation of YAG:Ce Scintillating Fiber Properties

Using Silicon Photomultipliers

I. Introduction and Motivation

In 1946, when asked by a congressional panel how to detect a uranium weapon being smuggled into New York harbor, Dr. J. Robert Oppenheimer, director of the Manhattan Project, famously replied, "Well, you might get a screwdriver and open up every crate and every suitcase and inspect it." Oppenheimer believed that there was no defense against nuclear terrorism and that there never would be. Since that time, advancements in the detection of ionizing radiation have revolutionized medical and scientific fields of study. Yet, the fundamental problems with detecting even large quantities of special nuclear material (SNM) at ranges of even a few meters remain. As the risks of nuclear proliferation and nuclear terrorism continue to grow at alarming and compounding rates, the need for effective monitoring of illicit nuclear trafficking has become increasingly apparent and is a national security priority [**1**].

Detection of SNM gamma ray emission at standoff ranges (i.e. distances greater than or equal to 1 km) requires the capability to both spectroscopically identify its particular isotopes and form an estimate of its spatial location. Due to the low activity of SNM, these estimates are inherently based on observation of very few characteristic gamma ray photons in an otherwise noisy background environment. Present spectroscopic methods rely on massive, bulky, inefficient, and power consuming technologies which prevent implementation on modern-day remote sensing platforms

such as a fleet of unmanned aerial vehicles which could patrol borders and major shipping lanes. Any viable remote detector must be compact, rugged, efficient, robust, reliable, and capable of discerning and extracting signal information from a complex environment.

Unlike collimated imaging techniques (e.g. mechanical modulation or coded aperture imaging), Compton cameras can provide high resolution images without blocking essential gamma ray photons. By using a densely packed matrix of thin fiber scintillators optically coupled to a pixilated detector, an efficient Compton camera with exceptional inherent spatial resolution can be achieved [**2**]. The use of thin fibers may allow recoil electrons from Compton scatter events to escape one fiber and deposit energy in another allowing even faster image acquisition times.

Recent developments in micro-pulling-down crystal growth technology has allowed for the growth of shaped single crystal inorganic scintillators, such as cerium activated multi-component oxides (e.g. yttrium aluminum garnet, YAG). Inorganic fiber shaped scintillators as thin as 400 μm in diameter and as long as 3 m have been commercially produced for particle tracking experiments [**3**]. A variety of position sensitive scintillation photon readouts are available (e.g. position sensitive photomultiplier tubes, charged coupled device cameras, etc.) and can provide inherently precise 2-D particle tracking in a bundle of scintillating fibers.

A relatively new solid-state photosensor, the silicon photomultiplier, is sensitive to single visible light photons and produces very fast, very large electronic signals while consuming little power at low operating voltages [**4**]. Arrays of silicon photomultipliers are ideally suited for the readout of a matrix of thin inorganic scintillating fibers for

Compton imaging applications. Such a sensor is a promising concept for remote standoff or aerial detection of SNM.

1. Objectives

The objective of this research is to investigate the properties of thin inorganic scintillating fibers when coupled to silicon photomultipliers. This knowledge is required prior to implementation and optimization of a compact, deployable Compton camera prototype capable of detecting SNM. Compton cameras require precise spatial position and spectroscopic information in order to reconstruct images from gamma ray interactions. Therefore, the achievable position and energy resolution of cerium activated yttrium aluminum garnet (YAG:Ce) scintillating fibers is studied, modeled, and measured. Results from theoretical calculations, idealized simulations, and empirical experiments are presented and discussed in this work.

2. Thesis Outline

This thesis presents the background, theory, methodology, and results pertaining to calorimetric and position-of-interaction experiments using inorganic scintillating fibers with silicon photomultiplier readouts. Chapter 2 discusses the background information relevant to Compton imaging, scintillation detection, scintillating fiber materials of interest, and silicon photomultipliers. Chapter 3 discusses the experimental and computational objectives and the methodology, tools, and equipment to be used in achieving them. Chapter 4 discusses the results from modeled and empirical experiments as well as the data analysis methodology applied. Chapter 5 summarizes the significant findings and conclusions, and lists recommendations for future research.

II. Theory and Background

This chapter discusses the theory relevant to designing a novel Compton camera using inorganic scintillating fibers and silicon photomultipliers. First, Compton imaging theory is briefly presented and provides the context for the calorimetric and position-of-interaction experiments. Next, theory of inorganic scintillation is discussed. Fiber optic theory is introduced and position-of-interaction estimation in scintillating fibers is reviewed. Then, a summary of the silicon photomultiplier properties is provided. Finally, the chapter concludes with a discussion of signal dispersion and sources of uncertainty in scintillation photon counting experiments using silicon photomultipliers.

1. Compton Imaging

The vast majority of SNM detection systems employed today merely detect the presence of radioactivity. This capability is not particularly useful in standoff detection if no spatial or spectroscopic information about the source is preserved. In typical operating environments, expected count rates from an expected source are low and background from terrestrial and cosmic sources is high; the result is high false alarm rates using current methods. For example, the anthracene doped polyvinyl toluene based Advanced Spectroscopic Portals currently used as radiation monitors at ports and border crossing are frequently triggered by shipments of benign, naturally radioactive materials such as bananas, kitty litter, and granite tiles [**5**]. Unlike simpler spectrometers, Compton cameras can not only identify radioisotopes based on the energy of characteristic gamma rays, but also form 2-D, 3-D, and even 4-D images of the spatial location of the source

[**6**]. Consequently, Compton imaging has seen wide application in the medical and astrophysics imaging communities (e.g. SPECT, MEGA, and COMPTEL) [**7**].

1. 1. Compton Scattering

Compton cameras reconstruct images of gamma ray source locations by exploiting the kinematics of scattering interactions between gamma rays and atomic orbital electrons. This interaction, known as Compton scattering, is the dominant mechanism for material interactions for the gamma ray spectrum of interest in SNM detection (i.e. 100 keV to 10 MeV). The angle of gamma ray scatter can be calculated by the Compton scatter- formula derived from [**8**] and given by

$$\cos(\theta) = 1 - \frac{m_e c^2 E_1}{E_0 (E_0 - E_1)}, \tag{2.1}$$

where m_e is the mass of an electron, c is the speed of light, E_0 is the energy of the incident gamma ray (which can be estimated or known a priori depending on application) and E_1 is the energy transferred to the electron by the scatter. If information about the location and the amount of energy deposited by Compton scatter interactions is known, then the gamma ray source is known to exist on the periphery of a cone of angle θ as shown in Fig. 1.

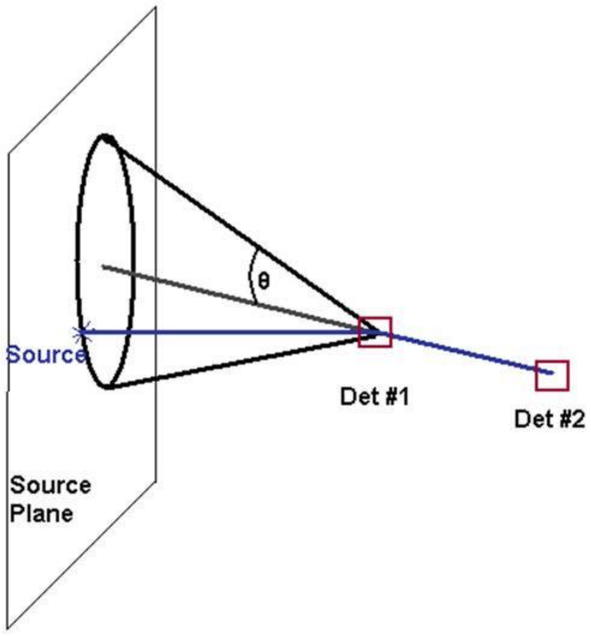

Fig. 1. Compton scatter angle and back projection illustration. When energy and interaction position information of a Compton scatter event is known, the scatter angle can be computed by (2.1). The source of the gamma ray is known to exist on the periphery of a cone about θ. As more observations are made, more conic frustums accumulate on a back-projected source plane to form an image. Correlated measurements result in intersections of these conic frustums which appear as bright pixels, representing the source location.

Typically, Compton cameras are constructed using multiple detectors in well characterized geometries. The first Compton scatter interaction occurs in the primary detector. The recoil electron from this interaction will deposit its energy in a short distance by further ionization of the detector material, producing a measurable signal proportional to the energy lost by the incident gamma ray. Under optimal circumstances, the scattered gamma ray will then deposit its remaining energy in a second detector via the photoelectric absorptive process which can be measured similarly to the recoil electron. By (2.1), the source is known to exist on the periphery of a backprojected conic frustum about θ. As more source gamma rays are observed, backprojected conic frustums accumulate and intersect on the image plane, thereby forming an image of the

source. Advanced Compton imaging methods can reconstruct images from multiple scattering interactions [**6**]. Interestingly, if the recoil electron's direction can be measured, the source location can be back projected to a particular arc segment of the periphery of the cone shown in Fig. 1 and therefore reduce the number of gamma rays required to generate a source image [**9**]. This phenomenon, if exploitable, proves valuable in SNM detection problems at standoff distances, where relatively few source photons are available.

Various types of radiation detectors can be used in Compton imaging (e.g. pixilated high purity germanium diodes, cadmium-zinc-telluride arrays, scintillator arrays, etc.). However, the recent advances in inorganic fiber scintillator and pixilated solid-state photosensor technologies provide a unique opportunity to develop efficient and inherently precise particle tracking detectors. An inorganic scintillating fiber based camera has the potential to be extremely robust in terms of both physicochemical stability and operational implementation. Coupled with new, low power solid-state silicon photomultipliers, scintillating fibers provide an inexpensive, lightweight, modular, and potentially revolutionizing detector system which could be deployed on a variety of platforms (e.g. unmanned aerial vehicles, oil rigs or ocean buoys, portal monitors, etc.) for remote sensing of SNM. For a more detailed treatment of Compton imaging, the reader is referred to [**6**].

1. 2. Compton Camera Directionality

In addition to inherently precise 2-D position-of-interaction resolution, a Compton camera made from scintillating fibers can be arranged to exploit preferential scattering directions of the particular gamma rays of interest. Although any scattering angle can

satisfy (2.1), the gamma ray scattering angles are heavily dependent upon incident gamma ray energy and are anisotropic in distribution. The Compton scattering angular distribution, known as the differential scattering cross-section, is described by the Klein-Nishina formula,

$$\frac{d\sigma}{d\Omega} \propto \left(\frac{1}{1+\alpha\left[1-\cos(\theta)\right]} \right)^2 \left(\frac{1+\cos^2(\theta)}{2} \right) \left(1+\frac{\alpha^2\left[1-\cos(\theta)\right]^2}{\left[1+\cos^2(\theta)\right]\left[1+\alpha\left[1-\cos(\theta)\right]\right]} \right), \quad (2.2)$$

where $d\sigma / d\Omega$ is the differential scattering cross-section, α is the ratio of incident gamma ray energy to the rest mass energy of the electron, and θ is the angle between the incident and scattered gamma ray. The Klein-Nishina formula, as presented here, assumes scattering with free electrons at rest. In reality, bound atomic electrons are in motion with some small (i.e. relative to the gamma energy) kinetic energy; the result is Doppler broadening of the scattering interactions. Ignoring this effect, the distribution of scattering angles is shown for a variety of incident gamma ray energies in Fig. 2.

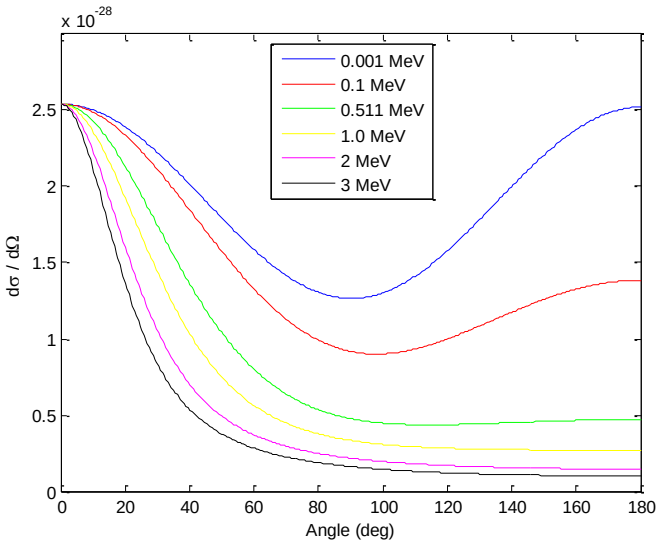

Fig. 2. The differential scattering cross-sections as a function of angle are given by the Klein-Nishina formula, shown here for a Z=32 target at various gamma ray energies in the regime of interest. It is noteworthy that higher energy photons tend to preferentially scatter in a forward direction. This phenomenon can be exploited when designing the Compton camera for a standoff application.

Importantly, higher energy gamma rays tend to scatter in a forward direction while lower energy gamma rays scatter forward and backward with near equal probability. Using long narrow scintillating fibers in a clever configuration, the Compton camera may exploit these properties for gamma ray energies of interest. That is, the camera can be arranged with some directionality, essentially providing gain by increasing the likelihood of measuring signal while reducing noise from background counts. A conceptual illustration of this effect in a scintillating fiber bundle Compton camera is shown in Fig. 3.

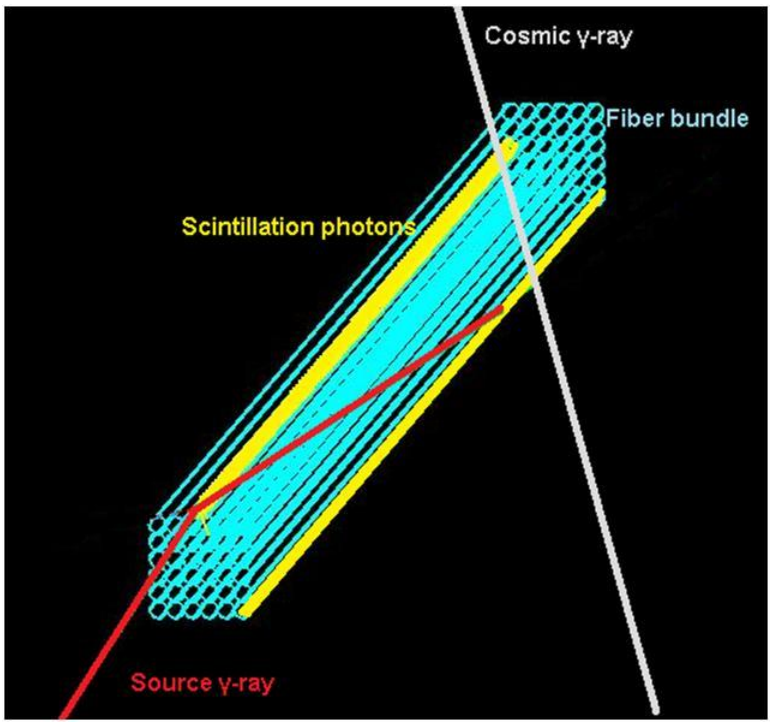

Fig. 3. A conceptual illustration of a fiber bundle Compton camera is shown. High energy gamma rays preferentially forward scatter, in accordance with the Klein-Nishina formula. Thus, directivity is gained by effectively increasing gamma path length in bulk detector material along the fiber axis. Notice how the hypothetical cosmic gamma ray passes through the detector without interacting while the source gamma ray Compton scatters and absorbs in two different scintillating fibers.

2. Radiation Detection Using Scintillators

This section discusses scintillators, their mechanisms, and their use as radiation detectors. The process of scintillation is the conversion of energy from an incident ionizing quantum (e.g. an X or gamma ray, a high energy particle, or even an ultraviolet photon of sufficient energy to ionize atoms) into a large number of visible photons. The two main classes of scintillators, organic and inorganic, are separated by their chemical structure and, thus, their scintillation mechanisms. Fundamentally, both types of scintillators behave similarly. Atoms are ionized by incident radiation via photoelectric, Compton, pair-production (i.e. gamma conversion), and Auger effects or by elastic

scattering with charged or neutral particles. The fast secondary electrons (e.g. δ-rays) produce an avalanche of tertiary electrons which thermalize and de-excite via fluorescence and phosphorescence. The details of these processes, however, in the two scintillator classes are somewhat different and more complex. Although organic scintillators offer some useful properties (e.g. fast decay times and inexpensive, quality fiber packaging), the focus of this research is on the latter of these two scintillator classes due to their greater stopping power, larger light yields, and novelty as a detection medium.

2. 1. Inorganic Scintillation Mechanisms

The physical mechanisms of scintillation in inorganic materials are best explained using models derived from the solid-state physics of crystal lattice structures. That is, unlike the organic materials, inorganic scintillators have wide energy gaps between the valence and conduction electron bands which are characteristic of the crystal constituents and their lattice structure. Between these bands is a forbidden region in which no electronic states can exist in a pure crystal lattice. As incident radiation and the subsequent δ-rays ionize the atoms in the crystal, electrons are excited into the conduction band leaving behind an equal number of holes in the valence band. Both electrons and holes are free to migrate within the lattice [**10**]. In reality, impurities, activators (i.e. intentional impurities) and defects (e.g. missing or misplaced atoms) alter the energy band gap structure of the crystal by forming charge carrier traps; their presence alters the luminescence properties of the crystal. An illustration of the band gap and luminescence processes of an inorganic scintillating crystal is shown in Fig. 4.

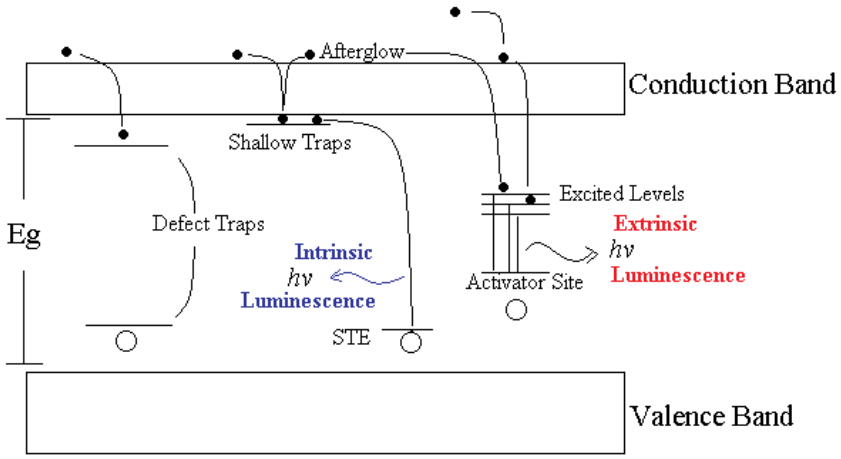

Fig. 4. A generic band diagram of an inorganic crystal scintillator is illustrated. The electrons and holes can annihilate via at activator or self-trapped exciton (STE) sites which are responsible for the extrinsic and intrinsic luminescence, respectively, of the crystal.

2. 2. Intrinsic Luminescence of Inorganic Scintillators

In an ideal pure crystal, these electron-hole pairs would eventually thermalize, thereby forming free excitons (i.e. electron-hole pairs which migrate together through the crystal attracted by Coulomb forces) which eventually annihilate producing a characteristic photon with energy equal to the band-gap energy. By the nature of the wide band-gap, this photon is in the ultraviolet spectrum and would be absorbed and re-emitted many times before eventually being transported out of the crystal. Measurement of these UV photons would require special materials (e.g. fused silica or quartz glass) to extend the spectral range of most PMTs [**8**].

In a real crystal, even one with no impurities, point defects (e.g. lattice vacancies and misplaced atoms called anti-site defects) cause charge carrier traps. These traps are problematic for several reasons and, of course, their effects are only exacerbated when crystal impurities are introduced. For example, deep traps can form stable color centers which cause optical absorption in otherwise clear crystals. Additionally, shallow traps

may release carriers by thermal processes, but can slow the luminescence decay of the scintillator. This slow decay is commonly referred to as "afterglow."

In ionic crystals where electron-phonon interactions are strong, free exciton migration can cause lattice distortions in their vicinity [**11**]. If sufficiently high in energy, these distortions immobilize excitons which become "self-trapped" and decay via radiative (e.g. UV photon emission) or non-radiative processes (e.g. thermal heating due to phonon interactions, sometimes called "quenching") [**8**] [**11**] [**12**] [**13**].

Self-trapped exciton sites play an important role in the "intrinsic luminescence" of pure inorganic scintillators. For example, pure NaI has exceptionally intense and fast intrinsic luminescence properties, especially at low temperatures, due to the stability of these recombination centers [**14**]. As another example, the alkaline-earth halides such as the XF_2 (where X can be Ca, Sr, or Ba) scintillators exhibit relatively high intrinsic and remarkably fast light yields due to a large number of meta-stable self-trapped exciton recombination centers [**10**]. Additionally, the role of self-trapped exciton luminescence has also been shown to affect the "extrinsic luminescence" of *activated* inorganic scintillators [**13**].

2. 3. Extrinsic Luminescence of Activated Inorganic Scintillators

In order to produce significant visible light yields, impurities known as activators are intentionally added during crystal growth. The presence of these activators serves to locally modify the forbidden gap of the pure lattice. As excitons (i.e. electrons and holes) drift through the crystal lattice, they preferentially recombine at the local activator sites known as "luminescence centers". The specific type and concentration of activators are carefully chosen to optimize the emission properties of various materials. The type of

activator and crystal structure alters the emission spectrum by shifting it into the visible region; this property is known as "extrinsic luminescence". The quantity of activators in the crystal affects its scintillation efficiency. If too few recombination centers exist, excitons saturate the activator sites and are more likely to be quenched (i.e. decay non-radiatively). Similarly, the presence of too many activator ions can result in aggregates of activator sites which can also form deep carrier traps, effectively increasing the probability for quenching and removing the carriers from the scintillation process [**11**]. Additionally, excess activator ions can increase the self-absorption property of the crystal which results in a Stokes shift and reduces overall intensity of the detected luminescence spectrum [**15**].

Finally, the extrinsic luminescence of the scintillator occurs upon recombination at the luminescence centers as a result of the either direct electronic transitions of the activator or transitions between the activator and crystal. Of particular interest is the rapid 5d-4f interconfiguration transition of the Ce^{3+} ion. Cerium is used in self-activated crystals (e.g. CeF_3) and is a popular activator in many recent oxide based inorganic scintillators because of this transition which produces high light yields with short decay times [**10**].

2. 4. Light Yield of Inorganic Scintillators

The scintillation properties of principal importance to the experimentalist include, first and foremost, light yield, conversion efficiency, fluorescence decay time, afterglow, optical clarity, refractive index, chemical attributes (e.g. effective Z of the material, stability in atmosphere, etc.), and physical attributes (e.g. density, achievable size, mechanical stability, etc.). All of these properties are important in selecting the

appropriate scintillator for the experiment; however, the most essential property is obviously the efficient conversion of ionizing energy into visible light. The light yield, L, is normally reported as the number of photons, N_{ph}, per unit of ionizing energy, E_γ. For a full discussion of the efficiency of scintillation conversion including its relationship to the band gap energy, the reader is referred to [**10**].

The process of converting ionizing radiation to visible light is non-linear in inorganic scintillators due to variations in secondary electron production near atomic K and L shells at X-ray energies (i.e. below 100 keV) in many inorganic scintillators. This property was first observe and studied in NaI:Tl as early as the 1960's [**16**]. Dorenbos summarizes the energy dependent, non-linear response of scintillators and its effect on energy resolution in [**17**]. Indeed, some materials which produce exceptional light yields suffer from performance degradation as a result of the statistical fluctuations caused by their inherent non-linear response (e.g. LSO:Ce, NaI:Tl, CsI:Na). Other inorganic scintillating materials do not seem to suffer from these non-linearities and can have superior intrinsic energy resolution compared to brighter scintillators (e.g. BaF_2, YAP:Ce) [**17**]. Interestingly, this phenomenon has been shown to affect chemically similar materials differently (e.g. YAP:Ce compared to YAG:Ce) suggesting proportionality is lattice structure dependent. Yet, chemically different, but structurally similar lattices have also shown the same behavior (e.g. LuAP:Ce vs YAP:Ce) [**18**]and [**19**]. Non-linearity in scintillator response is an ongoing area of research.

2. 5. Scintillation Kinematics

The fluorescence decay time, the next important property of a scintillator, is most often described by a simple exponential or a summation of multiple exponential decays which typically correspond to the radiant transition times of the activator. A typical scintillator with a single dominant emission flux profile, $\varphi(t)$, can be described by

$$\varphi(t) = \varphi(0)\exp\left(-\frac{t}{\tau}\right), \tag{2.3}$$

where τ is the decay time constant of the luminescence center.

Often, however, the decay kinetics are more complicated and depend on parameters such as temperature and type of incident radiation [**20**]. In most applications, fast decay times are desirable to facilitate high count rates and increase signal-to-noise ratios. Luminescence theory states that the electric dipole transitions are the most probable mode of de-excitation with a radiative rate

$$R = \frac{1}{\tau} = \frac{8\pi e^2}{cm_e}\frac{f \cdot n}{\lambda^2}\left(\frac{n^2+2}{3}\right)^2, \tag{2.4}$$

where c is the vacuum speed of light, m_e and e are the mass and charge of an electron, λ is the wavelength of the transition, n is the refractive index of the material, and f is the oscillator strength of the transition [**10**]. From (2.4) it can be seen that the decay time constant, τ, is proportional to the square of the emission wavelength. This indicates that higher energy photons are emitted faster from the electric dipole transitions which explains the extremely fast decay associated with intrinsic luminescence of crystals in the UV.

Since the emission wavelength can be assumed to be inversely proportional to the band gap energy, E_g, it can be shown that $L \propto 1/E_g$ and $\tau \propto 1/E_g^{\,2}$ [**10**]. Since L is desired to be large and τ small, it is obvious that these properties are in competition. In search of an optimal balance between yield and decay time, Birks proposed a figure of merit,

$$M = \frac{L_S}{\tau} = \frac{\frac{1}{E_\gamma}\int_0^\infty \varphi(t)\,dt}{\tau} = \frac{\varphi(0)}{E_\gamma}. \tag{2.5}$$

Birks' figure of merit is the ratio of total scintillation light output, L_S, to τ. By definition, M is equivalent to the ratio of peak scintillation intensity (i.e. the peak number of scintillation photons per second) to incident ionizing energy for simple decay profiles. This figure of merit is essentially a measure of signal-to-noise.

If a scintillator has multiple decay components, it might be described by a series of weighted sums of exponential decays. However, it is important to note that as higher order decay kinematics influence scintillation time profiles, such mathematical descriptions may be less of a description of luminescence mechanisms than an empirical data fit and, thus, may lose their physical meaning. That is to say, physical conclusions should not be drawn from decay profile fits alone since the physical mechanisms of luminescence may be obscured by more complex physics. For example, the decay profile of a scintillator is heavily dependent on the role of thermal traps and temperature [**20**]. At room temperature, afterglow is caused by charge carriers which are released via thermal excitation from shallow traps from which they could not escape at lower temperatures. Similarly, at high temperatures, thermal quenching (i.e. non-radiative

decay) increases and drastically alters the time profile of scintillation and reduces overall scintillation yield.

2. 6. Photon Transport in Scintillators

At this point, the discussion shifts focus from the photon production mechanisms to the transport. As mentioned, the presence of the activators serves to increase scintillation yield but also to shift the emission spectrum to energies below the band gap where the crystal is essentially transparent. Of course, there is *some* optical absorption, mostly due to overlap between the activator emission and absorption spectra, see Fig. 5. However, in materials with a well engineered activator concentrations, self-absorption from the activator is limited and absorption results primarily from optical opacity due to impurities and point defects in the lattice which form color centers. Other optical defects include cracks, gaps (e.g. air bubbles), and roughened surfaces which cause unnecessary reflections and refractions. These factors which affect optical clarity are consequences of crystal growth techniques.

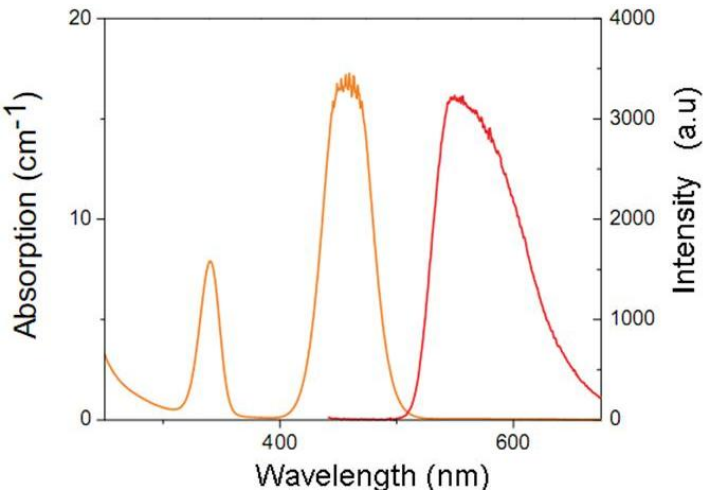

Fig. 5. The absorption or excitation (orange) and emission (red) properties of single crystal fiber YAG:Ce is shown. The overlap of emission and absorption curves indicates self-absorption. The data shown is adapted from [21**].**

Other factors are beyond the control of the crystal engineer. As mentioned, the activator emission can be absorbed by activator sites themselves, "particularly for Ce based and Eu doped crystals because of the overlap of the f-d and emission of the d-f bands" [**10**]. Efforts to control the attenuation of light within inorganic scintillators by varying types and amounts of dopants, as well as surface treatments, have proven successful for applications in depth-of-interaction experiments [**22**].

Scintillation photon transport can be treated using classical geometric optical theory; that is, the scintillation photons are treated as isotropically distributed and randomly polarized and are subject to refractions and reflections. Snell's Law,

$$n_1 \sin\theta_1 = n_0 \sin\theta_0 , \tag{2.6}$$

describes the refraction of light at interfaces between two materials, denoted by subscripts, of different refractive indices, n_i, where θ is angle from normal to the materials interface. By definition, the index of refraction of a material is the ratio

between the speed of light in a vacuum to the speed of light in that material. Since most activated inorganic scintillators have relatively high refractive indices, typically above 1.8, surface treatment is essential to efficient transport of scintillation photons to a photodetector [**8**].

High indices of refraction cause several problems for light collection. First, most photodetectors have some sort of optical coating (e.g. glass, $n \approx 1.5$) for protection. This change from higher to lower refractive index allows for the phenomenon of total internal reflection. The critical angle is the angle at which incident optical rays are totally reflected back into the material and is defined by

$$\theta_c = \arcsin \frac{n_1}{n_0}. \tag{2.7}$$

Note that the light must travel from material 0 to material 1, and n_0 must have a larger refractive index for total internal reflection to occur.

Internal reflection losses can be substantial if not mitigated. As an example, the critical angle for scintillating material with $n_0 = 1.8$ is approximately 56° when interfacing with glass and 33° when interfacing with air. Assuming uniform angular distribution of light on the interface, the loss incurred from total internal reflection is $\cos\theta_c$, or about 56% and 83% respectively. Consequently, index matching fluid such as highly viscous transparent silicon oil or optical epoxies are used to mitigate these total internal reflection losses.

In addition to refraction, optical photons undergo Fresnel reflections which occur at interfaces between materials of different refractive indices. In classical electromagnetic theory, Fresnel's equations describe the relative fraction of transmitted

and reflected s-polarized and p-polarized electromagnetic waves at dielectric interfaces. The overall reflection intensity, R, is given by quadrature sum of the reflection coefficients, r_s and r_p,

$$R = r_s^2 + r_p^2 = \left(-\frac{\sin(\theta_i - \theta_t)}{\sin(\theta_i + \theta_t)} \right)^2 + \left(\frac{\tan(\theta_i - \theta_t)}{\tan(\theta_i + \theta_t)} \right)^2, \tag{2.8}$$

where θ_i is the incident angle of the electromagnetic wave, and θ_t is the angle of transmission which follows Snell's law. In high refractive index materials and especially at large, but less than critical incident angles, Fresnel reflections can be significant as shown in Fig. 6.

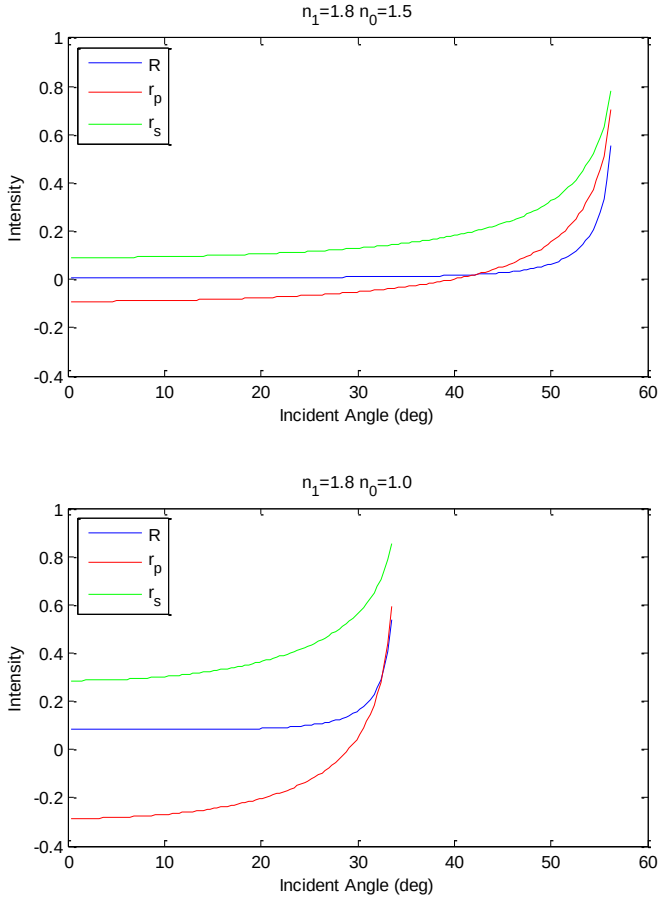

Fig. 6. Fresnel reflections are shown for a typical inorganic scintillator interfacing with glass (top) and air (bottom). Notice the critical angles are shown as asymptotes. While glass interfaces result in nearly negligible Fresnel reflections for much of the angular spectrum, air interfaces have a minimum reflection intensity in excess of 8%.

To aid in the efficient collection of photons which undergo many reflections within the scintillator, commercial inorganic scintillators are typically coated (on all but one surface) with a diffuse reflector such as Al_2O_3 or MgO powder which offer reflectivity coefficients up to 0.99 [**10**]. Diffuse reflectors follow Lambert's cosine law which states that the observed radiant reflection intensity is directly proportional to the cosine of the angle between the observer and the surface normal. This is in contrast to specular reflections which follows the familiar law of reflection. Somewhat against

intuition, diffuse reflection allows better scintillation photon collection because it breaks the symmetry which might otherwise trap optical rays in trajectories which would never be detected (e.g. internally reflected rays).

One final consideration should be given to high refractive index scintillators with long optical path lengths. Recalling that the refractive index is by definition a measure of the speed of the photons, light in a material with $n_0 = 1.8$ travels nearly twice as slowly as in vacuum. Therefore, it can take nearly a nanosecond for the photons to travel 15 cm. Considering the large numbers of reflections which the scintillation photons encounter before collection, there can be a non-negligible time delay which is dependent on the position of photon creation.

2. 7. Physicochemical Properties of Inorganic Scintillators

The final scintillator properties to be discussed are arguably the most important from an engineering and application perspective: the physical and chemical properties. Ideally, scintillator crystals should be rugged (i.e. mechanical and thermal shock resistant), hard, and chemically inert. Some crystals are hygroscopic and must be "canned" to avoid contact with water in the atmosphere. Crystals should be able to be grown in large dimensions and shaped, ground, and polished with conventional tools without cleaving. Above all, crystals should be dense and contain high-Z materials to increase the radiation stopping power of the scintillator.

3. Scintillating Fibers

Fiber optic theory is the study of light guidance in dielectrics and has been a widely studied field since as early as 1854 when John Tyndall demonstrated that light

curved within a stream of water. Like the water, optical fibers exploit the principle of internal reflection to trap light in a core of high refractive index material within a cladding of lower refractive index. This cladding is thin and can be any dielectric with a lower refractive index, including air. Fiber scintillators are a popular detection material in high-energy particle tracking experiments because of their inherently achievable two dimensional position resolution when coupled to pixilated detectors. Fiber scintillators are thin (e.g. 250-500 μm), shaped in convenient geometries for ray propagation (typically circular or square cross-sections), and are usually made from scintillating plastics or glass because of their optical properties [**8**]. Recently, inorganic crystal scintillators have been grown into thin fiber shapes using the micro-pulling-down growth technique [**3**].

3. 1. Light Formation and Propagation in Scintillating Fibers

When incident radiation causes scintillation within these fibers, a fraction of light (inversely proportional to the ratio of refractive indices between cladding and core) is trapped within the fiber and propagates toward either end. The total fraction of light trapped in a scintillating fiber is given by

$$\begin{aligned} F_T &= 2\cdot\frac{\Omega}{4\pi} = \frac{1}{2\pi}\int_0^{2\pi} d\phi \int_0^{\pi-\theta_c} \sin\theta d\theta \\ &= \left[1-\cos\left(\pi-\theta_c\right)\right] = 1-\sin\theta_c \\ &= 1-\frac{n_{clad}}{n_{core}} \end{aligned} \quad . \qquad (2.9)$$

From (2.9), it can be seen that a high core refractive index results in a high trapping efficiency. However essential, trapping scintillation light is not the goal. Rather, the goal is to "pipe" scintillation light to a photosensor. Therefore, the

scintillation light must be able to escape the fiber end rather than be totally internally reflected and forever trapped. Conventional scintillating fibers have relatively high cladding-to-core refractive index ratios (e.g. Saint-Gobain BCF plastic fiber scintillators, $n_{clad} / n_{core} \approx 1.5/1.6 = 0.94$) [**23**]. Consequently, the critical angles are quite large and trapping efficiencies are very low. The result is, disregarding propagation losses, fully efficient fiber end escaping efficiencies. However, for inorganic fiber crystals of much lower n_{clad} / n_{core} ratios, the escaping efficiencies can be quite low and can suffer from the same internal reflection losses as their bulk crystal counterparts.

Only light arriving at the fiber end at an incident angle that is less than the critical angle can escape the fiber and be detected. Assuming the fiber end plane is orthogonal to the fiber axis, not every trapped ray can escape, only rays propagating between 0° and θ_c about the fiber axis will be directly detected. This assumes that $\theta_c < 45°$; otherwise all trapped rays will escape as mentioned with regard to traditional scintillating fibers with poor trapping efficiencies. Rays propagating between $\vartheta_T = 90° - \theta_c$ and θ_c from the axis will be totally trapped in the fiber, as illustrated in Fig. 7. The majority of these totally trapped rays are lost through optical absorption in the material, but some may also undergo Rayleigh scattering (due to small, local density changes in the material) or experience reflections off rough surfaces, cracks, or defects and may be detected.

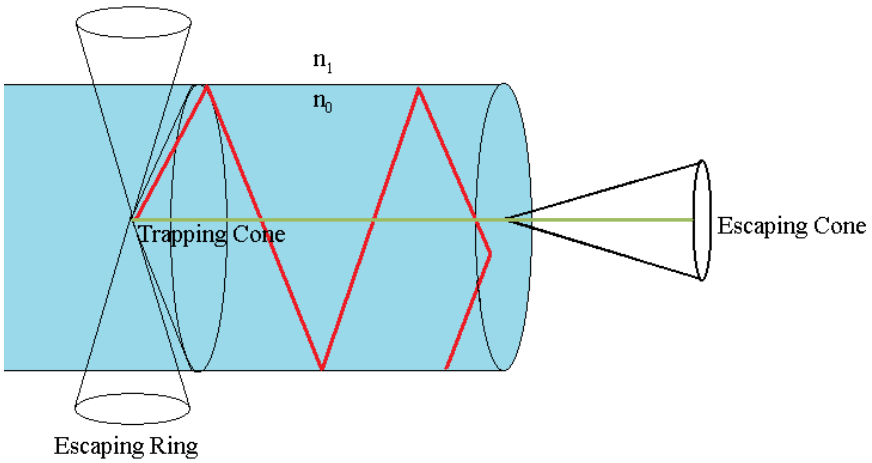

Fig. 7. Cross-sectional view of a scintillating fiber illustrates the effects of photon trapping and escape due to internal reflections. Mentally rotating the 2-D image 2π about the fiber axis gives the full picture. Note that refractions are not drawn to scale for illustrative purposes.

In Fig. 7, the escaping ring is drawn as cones for simplicity but are in reality a tapered ring about the fiber axis since the scintillation photons are not confined to a two dimensional plane. There is also, in reality, another trapping cone with opposite orientation along the fiber axis. It is important to note that the escaping angles at the original site and fiber ends are identical.

To quantify this escape efficiency, one can assume, by symmetry in the mean, that half of the trapped scintillation photons travel toward each fiber end and $\theta_c < 45°$. Then the fraction of photons which escape a single fiber end is given by

$$F_E = \frac{1}{2} F_T \frac{\Omega_{escape}}{\Omega_{trapped}} = \frac{1}{2} F_T \frac{\int_0^{2\pi} d\phi \int_{\vartheta_1=0}^{\vartheta_2=\theta_c} \sin\vartheta d\vartheta}{\int_0^{2\pi} d\phi \int_{\vartheta_1=0}^{\vartheta_2=\vartheta_T=\pi-\theta_c} \sin\vartheta d\vartheta}$$

$$= \frac{1}{2} F_T \frac{1-\cos\theta_c}{1-\sin\theta_c} = \frac{1}{2} F_T \frac{1-\cos\theta_c}{F_T} \quad . \qquad (2.10)$$

$$= \frac{(1-\cos\theta_c)}{2} = \frac{1-\sqrt{1-\left(\frac{n_{clad}}{n_{core}}\right)^2}}{2}$$

For $\theta_c < 45°$, the fraction of detectable light no longer depends on the quantity of light trapped in the fiber. However, if an index matching fluid were used at the fiber end, the critical angle could be increased to allow more photons to escape the fiber into a photosensor. Without the aid of index matching material, the absolute upper limit of escape efficiency for any fiber scintillator is 14.6% per fiber end. The graph in Fig. 8 shows the improvement in escape efficiency as the refractive indices are matched.

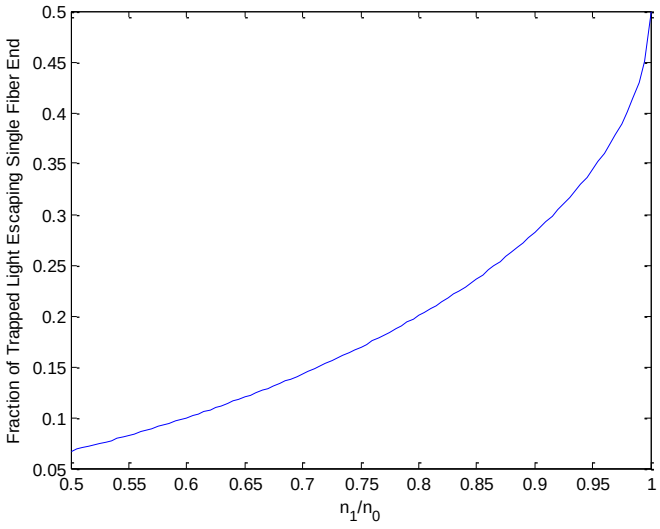

Fig. 8. The effect of index matching fluid, n_1, on the escape efficiency of light trapped in a scintillating fiber, n_0. Recall that the maximum escape efficiency for a single fiber end is 50% of the total *trapped* light.

Photons that do escape the fiber ends are refracted according to Snell's law. Due to their relatively high refractive index, light which exits scintillating fibers (indeed, optical fibers in general) is emitted in a cone about the half angle, θ_{launch}, which may also be called the "launch angle." A property closely related to the launch angle is the "numerical aperture" (NA) of the fiber which is described by

$$NA = n\sin\theta_{launch} = \sqrt{n_{core}^2 - n_{clad}^2} \tag{2.11}$$

where n is the refractive index of the external medium, typically air. Large values of NA represent large launch angles and, thus, larger acceptance cones. The NA of a scintillating fiber affects the direction of escaping photons at the fiber ends. Ideally, the launch angle would perfectly match the angle subtended by the photosensitive surface. For the case where a $n_{core} \geq \sqrt{2}$ and $n_{clad} \approx 1$, such as an inorganic fiber crystal using air for cladding, the NA value reaches its maximum. That is, the launch angle reaches 90°

which is the maximum for any fiber. This implies the escape efficiency is less than unity; in other words, these conditions result in some fraction of totally trapped light. In this case, very little of the escaping light will be normally incident on the photosensor. Under certain conditions, the use of an index matching fluid can, in addition to improving the escape efficiency, redirect the escaping rays toward normal incidence. Such is the case when moving from a high index fiber (e.g. n=1.8), to a moderately low index fluid (e.g. n=1.4), to a medium index detector window (e.g. n=1.5). Without the index matching fluid, the inevitable fiber-air interface would cause severe refraction and potential losses especially when using small active detector areas (e.g. a silicon photomultiplier).

Light propagates in two distinct modes within scintillating fibers. Meridional rays pass through the center of the fiber; these rays are only produced when the scintillation photon production occurs near the center. Meridional rays travel quickly and efficiently (i.e. without much loss). For these reasons, meridional rays are desired in fiber optic communication using single mode fibers. Skew rays originate away from the fiber center and propagate along spiral paths. Skew rays have much longer travel times and path lengths and tend to travel along the outer rim of the fiber. Therefore, the probability for loss due to absorption and scatter is increased, as is the light collection time.

Precision timing is often important for fiber scintillator readouts since it contains position information about the interaction. If the time difference of arrival at the two fiber ends is resolvable, it can be used to determine the position-of-interaction; such methods are known as “time-of-flight” and have been used in particle tracking experiments using long scintillating fibers [**24**][**25**].

Ray tracing Monte Carlo software (e.g. DETECT2000) can be a useful tool for modeling light propagation in scintillating fibers. The illustration shown in Fig. 9 depicts the results of a scintillation event in a bundle of organic scintillating fibers.

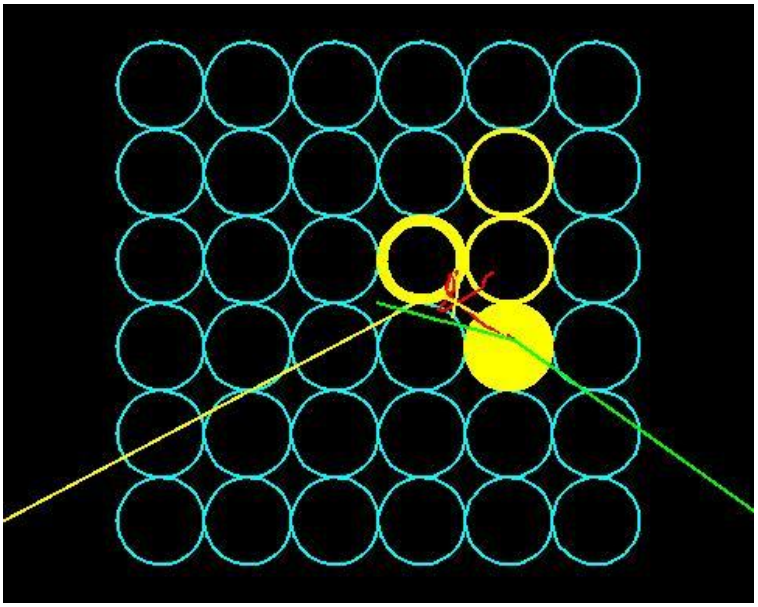

Fig. 9. The results of a scintillation event in a bundle of organic fibers modeled in GEANT4 [26] are shown. Green tracks represent primary ionizing radiation. Red tracks are secondary electrons which produce yellow scintillation photons. This also shows the efficacy of Compton recoil electron tracks being observed in neighboring organic scintillating fibers.

Meridional rays are seen in the lowest fiber where the interaction occurred in the center while all other fibers only contain skew rays which propagate along the outer rim of the fiber core. Since meridional rays can only be produced about the center of a round fiber, skew rays are more likely to be produced by scintillation. This presents a potentially problematic scenario for scintillation detection when using a silicon photomultiplier. The details of these devices are discussed in Section 5. 1. below, but for the continuity of this discussion they are briefly described here.

The silicon photomultiplier is a pixilated array of as many as 1600 avalanche photodiodes per mm^2 operating in the Geiger regime. Each pixel essentially discharges a binary output when struck by a visible light photon; the array pixels collectively act as proportional detector device. Pixels that fire upon detection of a photon must recharge (over the course of a few or few tens of ns), resulting in a paralyzable dead-time. This leads to one type of device saturation. If large quantities of light from skew rays are incident upon relatively few pixels in a short amount of time (e.g. the decay time of organic scintillators is typically less than the pixel dead-time), the device can saturate and the signal response will be non-proportional.

3. 2. Estimating Energy and Position Resolution in Scintillating Fibers

The time-of-flight method discussed above requires long, transparent fibers to determine position-of-interaction; this method is impractical for short and/or relatively high-loss scintillating fibers such as inorganic fiber-shaped crystals. However, another convenient method for obtaining position-of-interaction information in fiber scintillators is derived from self-attenuation within the material. Knoll describes this property (derived from Beer's Law) as "attenuation length" which relates the intensity of light (i.e. the number of photons) measured at one fiber end to the light yield at the interaction site using an exponential function such that

$$N = \frac{1}{2} N_0 \exp\left(-\frac{x}{\lambda}\right), \tag{2.12}$$

where N_0 is the estimate of the total amount of trapped scintillation light, x is the distance between the interaction and the readout which will be determined on a per event

basis, and λ is the known attenuation length of the material. Typical values for λ range from tens to hundreds of centimeters [**8**].

Due to the Stokes shift in most scintillating materials, as path lengths increase the spectral components will be red shifted. Inorganic crystals are typically quite transparent to optical wavelengths. However, the absorption and re-emission (i.e. isotropic emission) of scintillation photons by activator sites and impurities will undoubtedly distort the scintillation signal as it propagates through the fiber, potentially decreasing the crystal attenuation length. For inorganic crystals with short (i.e. relative to the optical path length to the detector) self-absorption attenuation lengths, other mechanisms such as scattering and absorption from crystal defects (e.g. cracks, micro-bubbles, gaps, color centers, etc.) can dominate the light attenuation process. These processes may be more difficult to model than simple exponential functions. For this reason, high quality crystals are important for position-of-interaction measurements. For the purposes of this research, these higher order effects are neglected.

Since the intensity of the measured scintillation pulse now depends on interaction position by (2.12), if λ and N_0 are known or can be measured, one can estimate the interaction location using dual fiber end readout by

$$x = \frac{1}{2}\left[\lambda \ln\left(\frac{N_2}{N_1}\right) + l\right], \tag{2.13}$$

where x is the one-dimensional estimate of the position-of-interaction as measured from the end nearest the first detector, l is the total fiber length as shown in Fig. 10, N_2 / N_1 is the ratio of relative signal amplitudes (i.e. the ratio of estimated number of photons) as

measured at the ends of the fiber. Likewise, the total trapped scintillation light, which is proportional to the energy deposited, can be estimated by

$$N_0 = \sqrt{N_1 N_2}\exp\left(\frac{l}{2\lambda}\right). \tag{2.14}$$

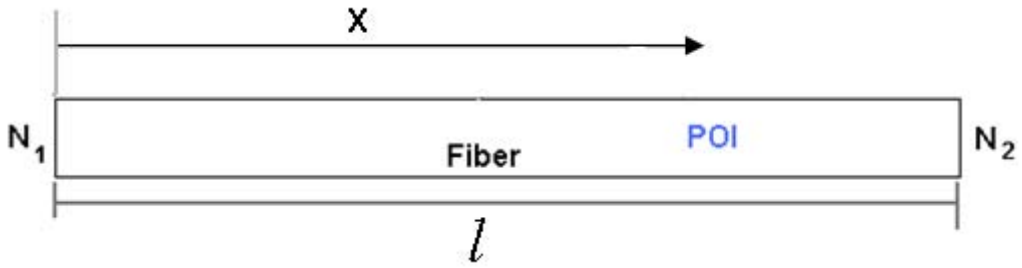

Fig. 10. Double end fiber readout parameters are illustrated. The position of interaction occurs at a distance x from end #1 and a position l -x from end #2. The resulting light yields are N1 and N2, respectively.

In reality, the true number of scintillation photons is a Poisson distributed random variable. As such, the energy deposited can never be known exactly and must be estimated by photon counting, typically involving secondary processes such as photoelectron multiplication. If the response function of the photosensor is linear (i.e. the number of photoelectrons produced is directly proportional to the incident number of scintillation photons), then $N_{1,2}$ can be understood as the number of photoelectrons instead of photons, although their statistics are not necessarily the same.

Using (2.13) and (2.14) and estimates of their uncertainties, the ideal energy and position resolution can be computed on an event-by-event basis. Let energy resolution be defined as the *relative* standard deviation of N_0, as defined by (2.14), which is directly related to the energy deposition of the interaction by $N_0 \propto L \cdot E$. Let position resolution be defined as the standard deviation of the axial position, as defined by (2.13). For

simplicity, it is assumed that λ is known and additional sources of noise (e.g. detector excess noise factor, electronics noise, etc.) are ignored here.

The variance of any function of multiple *independent* random variables with small and symmetric errors can be calculated using

$$\sigma_f{}^2 = \left(\frac{\partial f}{\partial x_1}\right)^2 \sigma_{x_1}{}^2 + \left(\frac{\partial f}{\partial x_2}\right)^2 \sigma_{x_2}{}^2 + ... \tag{2.15}$$

where $\sigma_{x_i}{}^2$ is the variance of the i^{th} independent variable [**8**]. Clearly, the values of N_1 and N_2 are related by N_0. However, the values are indeed random variables and do not *depend* on each other, hence N_1 and N_2 are *conditionally* independent and (2.15) can be applied to both (2.13) and (2.14) to solve for the ideal position and energy resolutions on an event-by-event basis. Doing so results in

$$\sigma_x{}^2 = \left(-\frac{\lambda}{2N_1}\right)^2 \sigma_{N_1}{}^2 + \left(\frac{\lambda}{2N_2}\right)^2 \sigma_{N_2}{}^2 \tag{2.16}$$

and

$$\sigma_E{}^2 = \left(\frac{\sqrt{N_2}\exp\left[\frac{l}{2\lambda}\right]}{2\sqrt{N_1}}\right)^2 \sigma_{N_1}{}^2 + \left(\frac{\sqrt{N_1}\exp\left[\frac{l}{2\lambda}\right]}{2\sqrt{N_2}}\right)^2 \sigma_{N_2}{}^2. \tag{2.17}$$

Dividing (2.17) by E^2 and taking the square root gives the energy resolution,

$$\left(\frac{\sigma_E}{E}\right) = \frac{1}{2}\sqrt{\frac{\sigma_{N_1}{}^2}{N_1{}^2} + \frac{\sigma_{N_2}{}^2}{N_2{}^2}}, \tag{2.18}$$

which can be further reduced to

$$\left(\frac{\sigma_E}{E}\right) = \frac{1}{2}\sqrt{\frac{1}{N_1} + \frac{1}{N_2}} \tag{2.19}$$

if $N_{1,2}$ are Poisson distributed. Likewise, further reduction of (2.16) under Poisson statistics gives

$$\sigma_x{}^2 = \frac{\lambda^2}{4}\left[\frac{1}{N_1} + \frac{1}{N_2}\right], \tag{2.20}$$

from which the position resolution (under the assumption of Poisson distributed $N_{1,2}$) in terms of the estimated total number of trapped scintillation photons is given by

$$\sigma_x = \frac{\lambda}{2\sqrt{N_0}}\sqrt{\exp\left[\frac{x}{\lambda}\right] + \exp\left[\frac{l-x}{\lambda}\right]}. \tag{2.21}$$

From (2.19) and (2.21) it is clear that increasing scintillation yield improves both the achievable position and energy resolutions. Another intuitive conclusion can be drawn from (2.19) and (2.21). As λ increases (i.e. the crystal become more opaque), the position resolution increases but only so long as there are sufficient photon intensities to predict N_0. Unfortunately, the energy resolution is degraded as more light is attenuated. These competing factors result in a challenging optimization problem in which the attenuation length (or fiber length) must be tuned for best energy and position resolution for the application at hand.

4. Scintillator Materials Under Study

Since the discovery of X-rays by Röntgen in 1895, various inorganic scintillating materials have been discovered in abundance. Some common crystals include alkali and alkaline-earth halides (e.g. NaI:Tl, BaF_2, etc.), chalcogenides (e.g. ZnS:Ag, CdS:Te), tungstates (e.g. $CdWO_4$), simple oxides (e.g. BeO, ZnO, etc.), and complex oxides (e.g.

aluminates, silicates, germinates, etc.). Rather than describe the properties of the various scintillator materials, the discussion will instead focus on materials used in this research, specifically cerium doped yttrium aluminum garnet (YAG:Ce) and other similar oxides. For a through description of the various scintillating materials the reader is referred to [**8**] and [**10**].

4. 1. Properties of Rare Earth Garnet Crystals

Garnet crystals are members of the neosilicate class which have been synthesized and widely used for their interesting optical and ferromagnetic properties in numerous fields of study. The relatively complex crystal structure of garnets was first solved by Menzer in 1926 [**27**]. He showed that garnet crystals follow the general formula $X_3Y_2(ZO_4)_3$ where X is a divalent cation (e.g. Mg, Mn, Ca, etc.), Y is a trivalent cation (e.g. Si), and ZO_4 is a large orthosilicate anion compound (e.g. SiO_4) [**28**]. In 1951, Yoder and Keith first synthesized a rugged, silicon-free garnet using yttrium and aluminum giving rise the enormously popular Nd-doped YAG lasing medium [**28**]. Other rare-earths such as gadolinium and lutetium are also substituted for or mixed with yttrium in garnets. Various garnet crystals can readily be grown using the Czochralski, Bridgman, or micro-pulling-down methods [**28**] [**29**].

Due in part to their role in the early development of lasing media, single rare-earth garnet crystals are grown with high purities and optical transparency using mature technology [**28**]. Such conditions provide an ideal arena for scintillator research. When doped with Ce^{3+} ions, rare-earth garnets scintillate quickly and relatively brightly due to the allowed 5d-4f electric dipole transitions of the activator [**17**]. The scintillation properties of the YAG:Ce were first studied by Moszynski, *et al* [**30**].

4. 2. Properties of the YAG:Ce Scintillator

The YAG:Ce scintillator has a fairly wide band gap (7 eV) but produces a unique emission spectrum peaked in the green at 550 nm which results from the activator's energy position within the band gap [**8**] [**30**]. Due to its relatively low density (4.55 g/cm^3) and low Z (e.g. Y=39, effective Z = 35), YAG:Ce is relatively inefficient for gamma spectroscopy. Reported values of the scintillation yield vary significantly (e.g. as low as 9,000 to as high as 23,000 photons per MeV, gamma equivalent) with cerium concentration, peaking around 0.2 mol% [**30**] [**31**]. The decay of the scintillator consists of two primary decay constants under gamma irradiation, a short component around 88 ns (72% intensity) and a long component around 302ns (28% intensity).

Interestingly, YAG:Ce light emission depends rather substantially on the type of excitation. Moszynski, *et al*., report several significant findings. First, the ratio of total scintillation intensity due to alpha particle interactionto that of gamma rays, the α/γ ratio, of YAG:Ce is equal to 21% (at 5.4 MeV). This is reasonably explained as a result of activator saturation due to the density of local exciton populations caused by heavy charged particle interactions. Surprisingly, the decay time constants not only decrease under alpha irradiation, but the intensities flip. In their later work Ledziejewski, *et al*., also note that the fast decay component of YAG:Ce under alpha irradiation more closely matches the value reported from laser excitation. Table 1 summarizes the findings of Ledziejewski, *et al*. [**32**].

Table 1. Scintillation Properties of YAG:Ce from [30] and [32]

Cerium Concentration	No. Photoelectrons	α/γ	Radiation	Rise Time	Fast Decay Component		Slow Decay Component	
% mol Ce	(#/MeV γ)	%	Type	(ns)	Time (ns)	Intensity (%)	Time (ns)	Intensity (%)
unknown	NA	21	Laser	-	58	100	NA	NA
	1200		γ	5	87.9	72	302	28
			α	NA	68.4	34	247	66
1.08	1270	21	γ	10	87.9	72	302	28
			α	NA	68.4	34	247	66
0.21	1420	21	γ	-	105.4	28.5	487.1	71.5
			α	-	88.9	14.9	458.5	85.1
0.015	1180	21	γ	-	115.3	9.2	651.2	90.8
			α	NA	89.5	11.6	666.4	88.4
0.012	1000	-	γ	-	-	-	-	-

Zorenko, *et al*, have observed that the decay kinetics phenomenon is only prevalent in single crystal and not single crystalline film YAG:Ce and suggest the behavior is due to the presence of Y_{Al} anti-site defects found in single crystal YAG [**13**]. They have shown that the slow UV emission from anti-site defects is strongly absorbed by the cerium sites which are often coupled to the anti-site defects. This radiative transfer of energy to the activator by intrinsic emission greatly influences both the rise and decay of the YAG:Ce luminescence. Independently, Selim, *et al*., have confirmed via positron annihilation spectroscopy that Al vacancies are indeed the dominant defects in YAG:Ce crystals and have shown significant improvement in energy resolution following O annealing and Al diffusion into YAG defect sites [**33**].

In order to explain the observed difference of luminescence decay between ionizing and optical radiation excitation, Zych, *et al*., conducted a series of measurements over a wide range of excitation conditions. They explain that the kinetics associated with non-ionizing radiation (i.e. energies less the the 7 eV band gap, such as 450nm laser light) differ from ionizing radiation because such low energies only deliver excitation

energy directly to the Ce activator ion. The energy level diagram for YAG:Ce is shown in Fig. 11, adapted from [**20**].

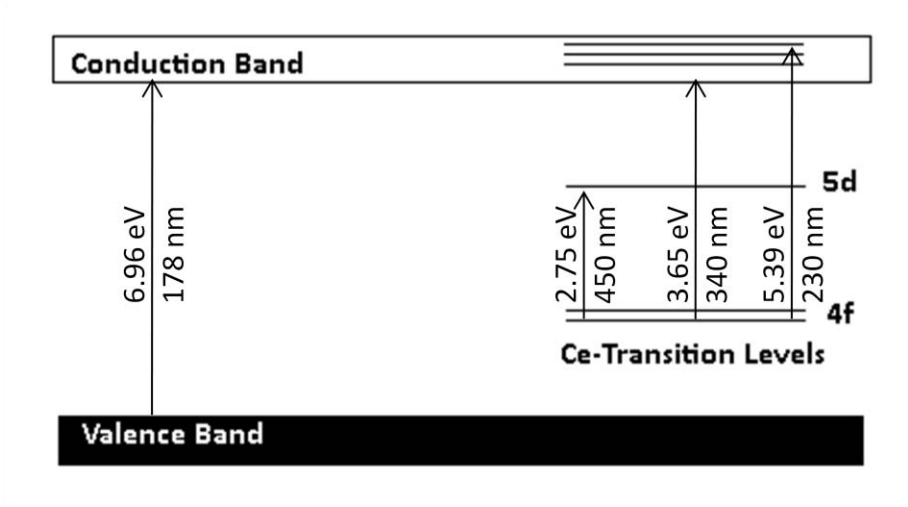

Fig. 11. YAG:Ce energy level diagram adapted from [20**].**

Such excitation results in a single exponential decay constant of 67 ns, in close agreement with the value reported by Moszynski, *et al*.. However, when excited by 178 nm optical radiation (above 7 eV), YAG:Ce shows the distinctive 320 ns slow component. Interestingly, the fast component is reduced to 85 ns, in agreement with excitation via gamma radiation [**20**]. Again, this can be explained by the strong Ce absorption of the intrinsic luminescence.

By exciting the crystal with increasing optical energy, Zych, *et al*., report an increasing probability for charge delocalization by observing an increase in fast component decay time beginning around 230 nm (5.4 eV) . Therefore, they attribute this time shift to the delocalization and migration of charge away from the excited Ce ions to

other sites. These results were confirmed by photoconductive experiments at the same excitation energies [**20**].

To explain the mechanism behind these kinetics, Zych, *et al*., turned to a series of time-resolved luminescence experiments over a wide range of temperatures (60-600K) during gamma and optical excitation. They discovered that the *radiative* decay constant (i.e. caused by optical excitation of the Ce ions) is constant across the temperature range. However, the *effective* decay constant (i.e. caused by ionizing excitation) shows complex low temperature behavior, decreasing to the radiative decay constant near 150 K before increasing to a maximum near 200 K then again decreasing monotonically back to the radiative decay constant near 400 K. The intensity of the fast component varies complexly as a function of temperature. Their results can be seen in Table 2. These behaviors are attributed to the trapping levels within the crystal which release or quench charge carriers depending on thermal conditions in the lattice. By mapping the thermoluminescence emission profile following X-ray irradiation, they identified as many as 11 shallow traps ranging from 0.129 to 0.634 eV. Thus, Zych, *et al*., have shown that the complex time decay profile of YAG:Ce luminescence is due to the release kinematics of shallow traps [**20**].

Table 2. Temperature dependent decay kinetics of YAG:Ce as reported in [20]

Temperature (K)	Eff. decay. const. at time zero (ns)	Amplitude of radiative term (%)	Amplitude of delayed term (%)	Radiative decay constant (ns)	Time const. of delayed decay (ns)
130	73.1	86.5	13.5	63.8	958.6
150	64.2	89.9	10.1	64.2	∞[b]
170	64.5	88.6	11.4	64.5	∞[b]
190	85.1	70.5	29.5	64.9	334.4
200	106.9	40.9	59.1	65.1	190.0
210	99.4	47.5	52.5	65.3	184.9
230	89.9	57.8	42.2	65.7	181.9
250	87.8	60.8	39.2	66.1	176.9
270	86.0	61.8	38.2	66.5	163.5
295	90.2	51.1	48.9	67.1	139.7
320	82.3	60.5	39.5	67.6	122.7
330	77.3	76.0	24.0	67.9	137.4
350	75.1	85.4	14.6	68.4	150.7
370	74.6	85.7	14.3	68.9	177.1
400	73.3	93.1	6.9	69.7	213.0
430	73.1	94.4	5.6	70.5	251.0
470	72.5	98.9	1.1	71.7	∞[b]
500	73.8	98.4	1.6	72.6	∞[b]

[a] Decays measured under irradiation from a ^{137}Cs source.
[b] Note: ∞ denotes a quasi-DC component, with a time constant greater than 2 μs.

This kinetic decay behavior has been observed in other rare-earth garnet scintillators (e.g. LuAG:Ce) which further confirms the presence of shallow electron traps in the garnet structure [**34**]. Chemically similar crystals such as yttrium aluminum pervoskite (YAP:Ce, $YAlO_3$) only exhibit one very fast, 25 ns, decay component [**35**].

The scintillation linearity (i.e. the proportionality of scintillation response) of YAG:Ce is a fairly good. A continuous increase in proportionality from 86-100% (with respect to light yield at 662 keV) is observed between 14 and 662 keV gamma ray energies. This is less impressive than the chemically similar cousin of YAG:Ce, YAP:Ce, which shows exceptional linearity, changing only 6% over the same range [**18**]. Yet, other contemporary Ce-doped multiple-component oxide scintillators such as

yttrium and/or lutetium oxyorthosilicates (e.g. YSO, LSO, and LYSO) suffer from significant non-linear responses (45% from 14-662 keV) [**18**] [**34**]. As a result, YAG:Ce offers superior energy resolution compared to other brighter scintillators such as (e.g. LYSO:Ce, $L \approx 27{,}000$ photons/MeV) [**36**]. Evidence for this is presented by Chewpraditkul, *et al*., who report the data shown in Fig. 12 and Fig. 13 [**34**].

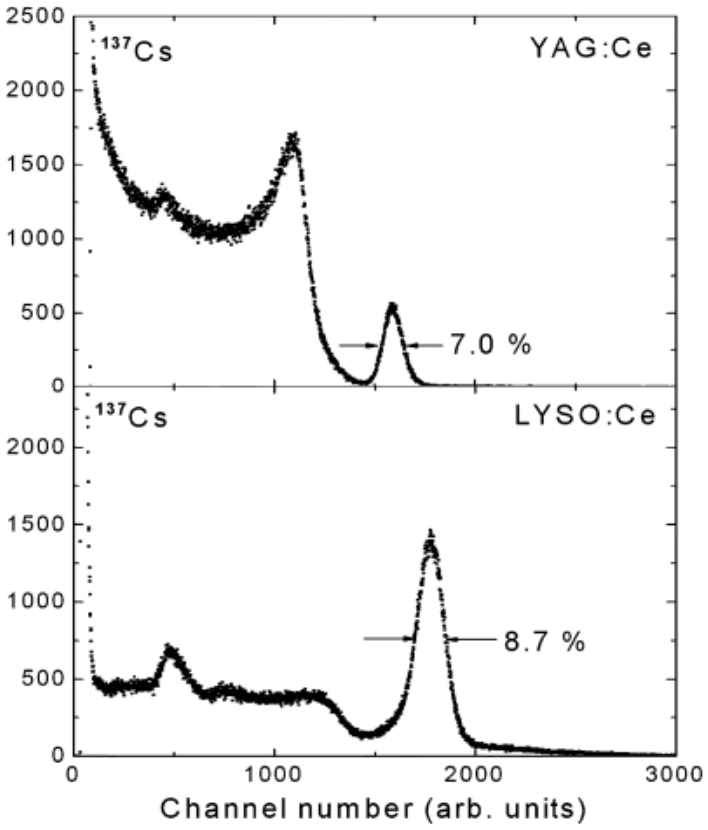

Fig. 12. Data adapted from Chewpraditkul illustrating the superior achievable energy resolution of YAG:Ce to a brighter scintillator, LYSO:Ce [34].

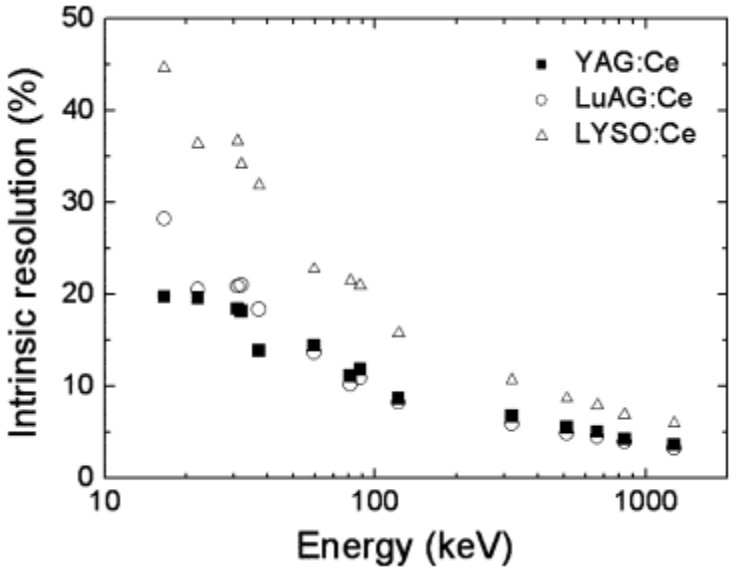

Fig. 13. Data from Chewpraditkul illustrating the intrinsic resolution of YAG:Ce [34**].**

As previously discussed, this intrinsic energy resolution limitation results from absorption processes near L and K-shell energies, and is particularly prominent for higher Z atoms, such as lutetium. This explains the lower energy resolution offered by lutetium based oxide scintillators.

From the intensity of the photopeak in comparison to the Compton edge in Fig. 12, it can be concluded that YAG:Ce is an inefficient scintillator. This is due to its low density and low effective Z, which result in a low stopping power. A similar scintillating crystal, LuAG:Ce, has higher light yields, higher effective Z, and higher densities than YAG:Ce; thus LuAG:Ce has several key advantages over YAG:Ce. However, in addition to the poor intrinsic resolution shown in Fig. 13, LuAG:Ce, as with all lutetium based scintillators, suffers from intrinsic background radiation from the naturally occurring isotope ^{176}Lu which produces about 50 counts/s/g of natural lutetium.

Despite resulting in an overall inefficient scintillator material, the low stopping power (i.e. low electron density) of YAG:Ce may prove useful in particle tracking experiments. This property may allow tracking of a Compton recoil electron in thin scintillating YAG:Ce fibers. According to the Bethe-Bloch formula for specific energy loss, the sum of the collisional (i.e. ionizing and exciting) and radiative losses yield the total linear stopping power of a material. The collisional loss in a material is described in [**37**] by

$$\left(-\frac{dE}{dx}\right)_{Coll}^{\pm} = \frac{5.08\times10^{-31} n}{\beta^2}\left[G^{\pm}(\beta) - \ln I_{eV}\right] \quad \text{units}\left[\frac{MeV}{cm}\right]$$
$$G^{\pm}(\beta) = \ln\left(3.61\times10^{5}\tau\sqrt{\tau+2}\right) + F^{\pm}(\beta)$$
$$F^{-}(\beta) = \frac{1-\beta^2}{2}\left[1+\frac{\tau^2}{8}-(2\tau+1)\ln 2\right] \qquad , \qquad (2.22)$$
$$F^{+}(\beta) = \ln 2 - \frac{\beta^2}{24}\left[23+\frac{14}{\tau+2}+\frac{10}{(\tau+2)^2}+\frac{14}{(\tau+2)^3}\right]$$

where n is the material electron density in m^{-3}, β is the ratio of the particle velocity to the speed of light, I_{ev} is the mean ionization potential of the material, and τ is the ratio of particle energy to its rest mass energy. The initial constant is a reduction of the natural constants as defined by Turner in [**37**]. The radiative loss term is approximated by

$$\left(-\frac{dE}{dx}\right)_{rad} \approx \frac{Z_{eff}E}{800}\left(\frac{dE}{dx}\right)_{Coll} \qquad (2.23)$$

where Z_{eff} is the effective atomic number of the material.

The fast electron total stopping power and range in YAG:Ce has been calculated over the energy regime of interest using (2.22) and (2.23) . The calculations are shown graphically in Fig. 14 and Fig. 15 as a function of electron energy.

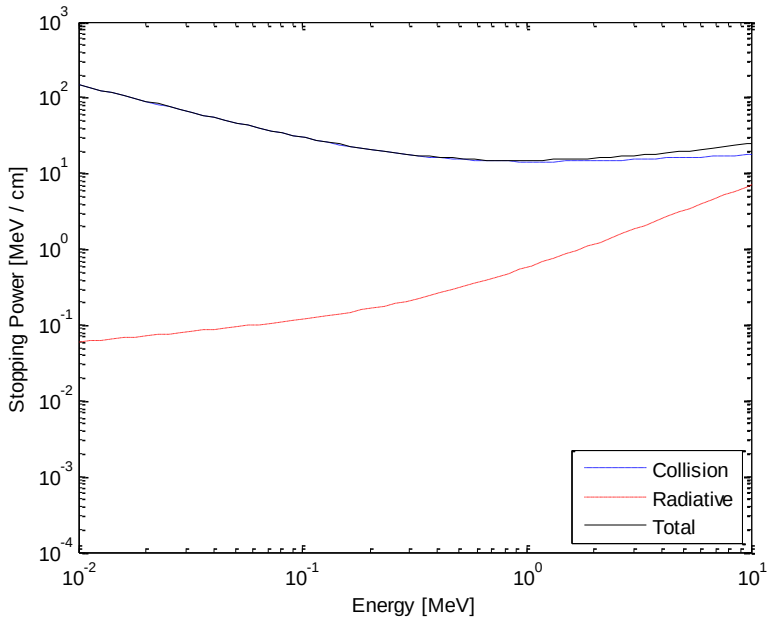

Fig. 14. The fast electron stopping powers in YAG:Ce calculated using the Bethe-Bloch is plotted over the energy regime of interest.

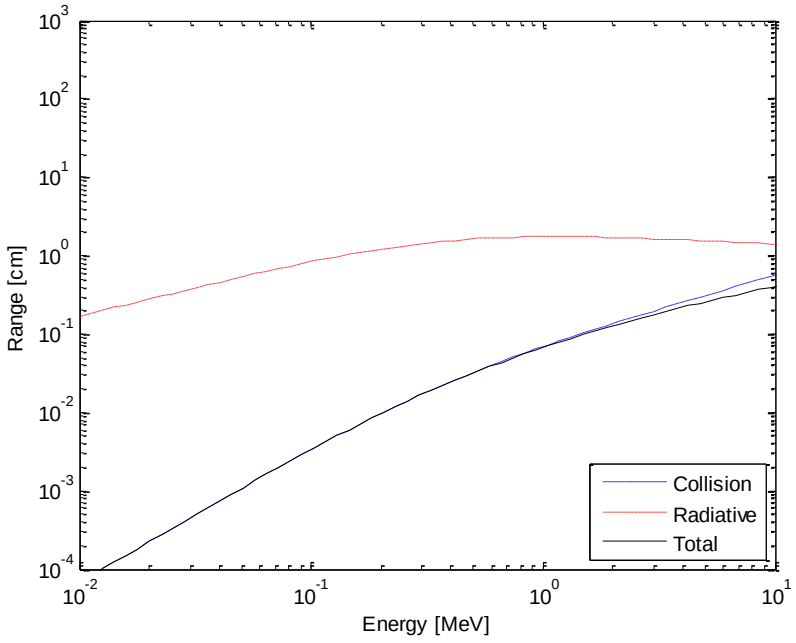

Fig. 15. The ranges of fast electrons in YAG:Ce calculated using the Bethe-Bloch formula is plotted over the energy regime of interest. The range values show good agreement and provide an expected range of tens to hundreds of microns for typical Compton recoil electrons.

From Fig. 15, it is clear that a range of tens to hundreds or even thousands of microns can be expected from Compton recoil electrons in YAG:Ce. Certainly, there is reasonable probability that such electrons can escape thin fibers (e.g. 400 μm diameter fibers which are commercially available [**3**]). Tightly packed bundles of fibers may allow the tracking of recoil electrons in neighboring fibers. Of course, this tracking capability may have negative implications for energy resolution if electron energy is lost in cladding material. Nonetheless, it is a promising area of research.

4. 3. Properties of Fiber Shaped YAG:Ce

Recent development of the micro-pulling-down (μ-PD) crystal growth technique has allowed the growth of shaped fiber single crystals [**28**]. This technique begins with the contact of a seed with the melt drop formed at the capillary die of an iridium crucible. The crystal is pulled down through a capillary tube in an argon atmosphere and directly annealed using an after heater just below the crucible [**38**]. The crystal is grown at a rate of between 0.1-0.5 mm/min under the control of a computer and CCD camera. The dimensions of the fibers can range from 0.3-3 mm in diameter and 10-100 cm in length [**21**]. These fiber crystals are commercially available in many popular materials such as LYSO:Ce, LuAG:Ce, and YAG:Ce [**3**].

Inorganic scintillating fibers have promising properties for medical imaging and particle physics applications because of their high light yields and achievable position and energy resolutions. Previous work conducted by Anfré shows excellent spatial resolution of particle interactions along fiber lengths using double end readout [**36**]. Anfré achieved under 1 cm in position resolution in alpha particle experiments using

YAG:Ce and under 5 mm in position resolution in gamma ray experiments using LYSO:Ce fibers [**36**] [**21**].

Anfré reported that the YAG:Ce fibers had a particularly weak scintillation yield of ~10,000 photons per MeV for gammas and ~800 photons per MeV alpha particles [**21**]. This light yield is low in comparison to other values in literature for gammas, but most surprisingly, shows an α/γ ratio of around 8%, much less than reported by Moszynksi, *et al.* [**30**]. While Anfré attributes this loss to the interaction mechanisms of alphas in the YAG crystal, another interesting characteristic of the fiber crystal may be to blame.

During the growth of fiber crystals, convective currents distribute the activator ions with a radial gradient over the cross-section of the crystal during cooling [**28**]. Simura, *et al*., observed this in experiments conducted with μ-PD growth of YAG doped with Nd, Cr, Yb, and Ce. The Ce doped YAG data collected by Simura *et al*. shown in Fig. 16 which agrees with the overall concentration reported by Anfré, shown in Fig. 17. Both, however, report excellent dopant concentration homogeneity along the length of the fiber crystal [**39**].

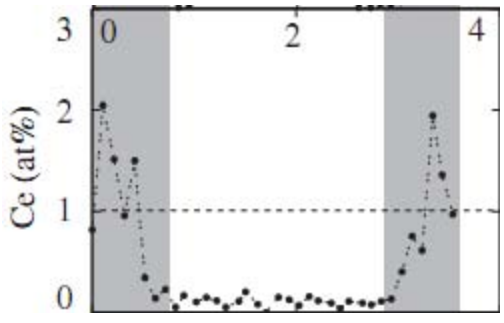

Fig. 16. Radial concentration of cerium dopant atoms in YAG crystals grown by μ-PD. Data adapted from [39**].**

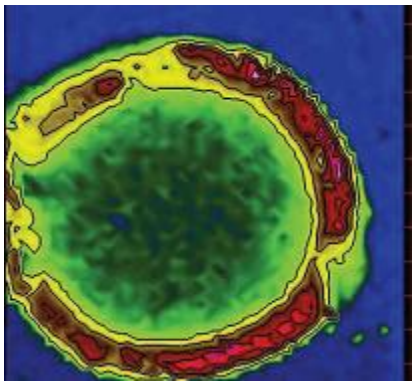

Fig. 17. Independent results confirming the concave radial distribution cerium dopant atoms in YAG crystals grown by µ-PD. Image adapted from [21**]. No absolute, quantitative values of concentration were reported.**

Simura, *et al*., claim that the data they present is misleading and that inhomogeneities of Ce concentrations are actually worse than reported due to the presence of inclusions near the rim of the fiber [**39**]. If this is the case, then perhaps an explanation for the lower than expected α/γ ratio observed in Anfré's fiber crystal is a result of the photon production near the fiber rim (due to the short range of alphas in YAG) which leads to skew optical rays that are confined to spiral trajectories along the outer rim of the fiber.

Similar results have been presented by Dujardin, *et al*., using confocal photoluminescence spectroscopy of 2 mm diameter LuAG:Ce fibers grown by Fibercryst [**40**]. Their results are shown in Fig. 18.

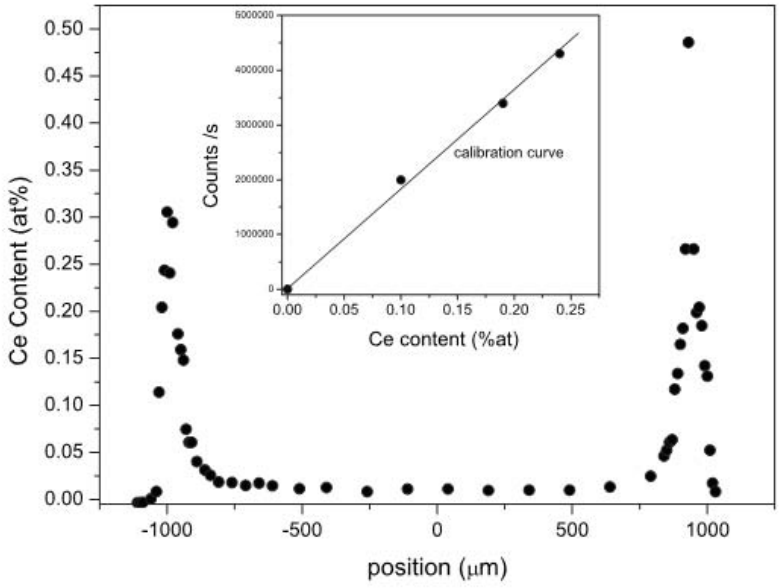

Fig. 18. Confocal photoluminescence spectroscopy results of cerium activator radial concentration in LuAG:Ce fibers as presented by Dujardin, *et al.*, are shown [40].

The evidence of strong radial dispersion of cerium activator sites in fiber crystals grown via μ-PD is abundant. If, indeed, there are inclusions, defects, impurities, or even rough surfaces near the rim of the fiber, these flaws undoubtedly will result in light attenuation, scattering, or escape as well as the absorption and non-radiative decay within other activator sites which could explain the poorer than expected performance of Anfré's fiber.

5. Photon Detection Techniques

Conventional photomultiplier tubes (PMTs) are the workhorse of scintillator readout. Despite their excellent gain factors, PMTs have fundamental limitations. Poor quantum efficiencies, large cathode work-functions, high operating voltages, and susceptibilities to magnetic fields demand the design of other high gain photon detectors for certain applications (e.g. hybrid positron emission tomography and magnetic

resonance imaging systems) [**41**]. The readout of thin inorganic scintillating fibers, such as YAG:Ce which emits in the green, may be well suited for the relatively new and promising new photosensor, the silicon photomultiplier. Fig. 19 shows the superior spectral response of photodiode based sensors compared to PMTs.

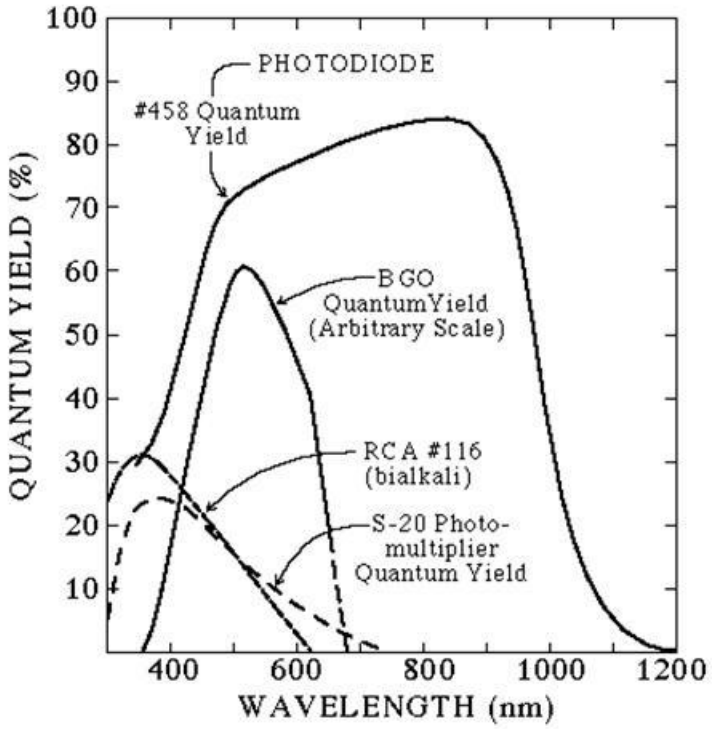

Fig. 19. The spectral response of a photodiode is superior to that of a PMT. Even a bialkali PMT is poorly matched to the emission spectrum of YAG:Ce, peaked at 550 nm. Figure adapted from [8**].**

5. 1. Silicon Photomultipliers

Photodiodes have long been used to detect visible light and operate using principles similar to diode based gamma ray spectrometers (e.g. HPGe detectors). Incident visible light photons create electron hole pairs which, in the presence of a strong electric field, can be swept apart forming measureable currents. Although they consume

little power, conventional photodiodes are insensitive and suffer from noisy performance, especially at room temperature. Consequently, they are typically operated in the continuous current mode.

Avalanche photodiodes (APDs) operate at higher bias voltages (100-200 V is typical but biases in excess of 1000 V are not unreasonable) causing the multiplication (or "avalanche") of ion pairs, in the depletion region, proportional to the number of photons incident upon the active region. Gain factors of several hundred are typically achieved in this process. Above a bias threshold known as the "breakdown voltage", an APD enters the Geiger operating region which results in the complete discharge of the APD. Geiger discharge will continue until the avalanche is quenched by reducing or removing the bias voltage across the diode. Typically, this quenching is achieved using a large (typically 50-100 kΩ) ballast resistor in series with the diode. The signal can be readout using a charge integrating pre-amplifier or directly across a load resistor [**4**]. A schematic is shown in Fig. 20.

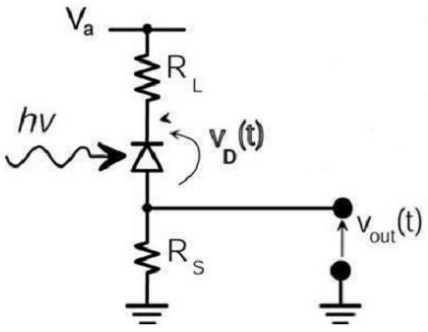

Fig. 20. Readout circuit of a Geiger-mode APD is shown; image is adapted from [4]. V_a is the bias voltage, R_L is the ballast resistor, R_S is the load resistor across which V_{out} is measured.

This breakdown occurs and can be quenched in a time on the order of a few nanoseconds. The rise and fall times of these current pulses are also influenced by the parasitic capacitances of the substrate. A more accurate circuit model for a Geiger APD (G-APD) is described in [**42**] and [**43**] and shown in Fig. 21.

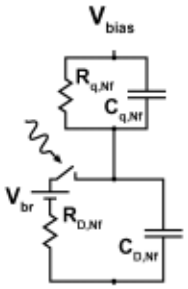

Fig. 21. Circuit model of a passively quenched G-APD is shown with substrate and storage capacitances. The image is adapted from [44]. Here, the diode array is modeled as a current source using the diode breakdown voltage, V_{br}, and the resistance, $R_{D,Nf}$, in series. The capacitors are the stray capacitances associate with the diode substrate.

In Fig. 21, the upper circuit loop depicts the ballast (a.k.a. quenching) resistor, R_q, in parallel with its associated stray capacitance, C_q. These values control the recharging rate and, thereby, the tail of the current pulse. Despite a desire for fast recharge times, the design is limited by the capacitance of the substrate and the high resistor values required to ensure quenching. The lower loop depicts the charge storage capacitance, C_D, of the reverse biased diode and a fast-switching, pulsed current source, V_{br} in series with R_D, which imitates the firing of the G-APD by instantly reducing the diode terminal voltage to its breakdown value allowing the flow of charge across C_D. The final component, R_D, is referred to as the "micro-plasma" series resistance of the diode during

discharge and slows the rise time of the pulse. This model is described in more detail in [**44**].

G-APD diodes are sensitive to single photon events (neglecting inefficiencies) and produce exceptionally high electron multiplication factors (order of 10^5-10^6) thereby producing fast and directly measurable signals. Arrays of G-APDs (known as silicon photomultipliers, solid-state photomultipliers, and a variety of other names) are made using complementary metal-oxide semiconductor (CMOS) fabrication techniques with pixel pitches as small as 25 μm [**45**] [**46**]. Recently, silicon photomultipliers (SiPMs) have become commercially available with high APD pixel densities (e.g. 1600 APD pixels/mm^2) and extremely low breakdown voltages, as low as 30-70 V[**45**] [**46**]. Arrays of SiPMs are also commercially available, some with custom electronic readout modules. Examples of individual various SiPMs and SiPM arrays are shown in Fig. 22 and Fig. 23.

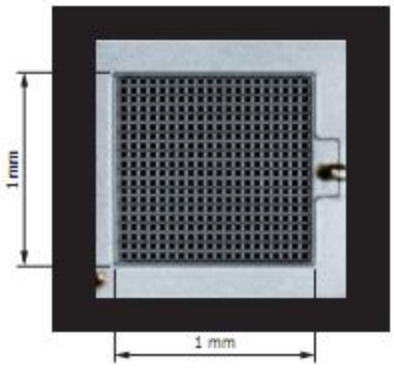

Fig. 22. Hamamatsu Multi-Pixel Photon Counter is a trademarked line of 1x1 mm SiPMs with APD pixel densities ranging from 100-1600 mm^{-2}. Hamamatsu claims timing resolutions of 200-500 ps, gain factors up to 2*10^6, and photon detection efficiency of 25-65% depending on model [45**].**

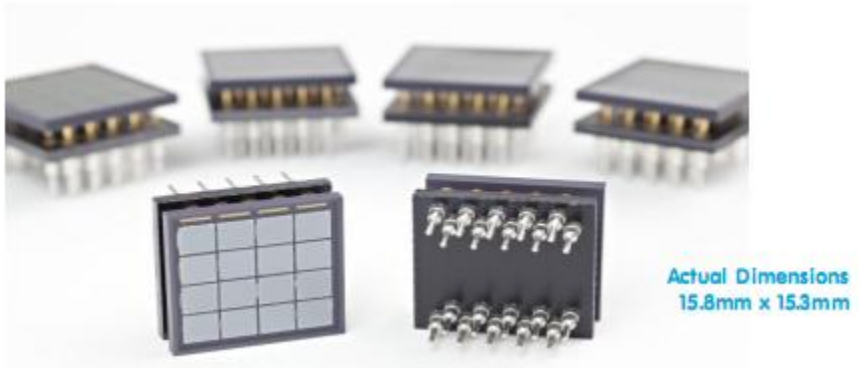

Fig. 23. Sensl's Scalable Silicon Photomultiplier Arrays are constructed using 4x4 individual SiPMs. These devices are conveniently designed for scalability. The Sensl SPMMatrix (not shown) is a prefabricated, fully electronically integrated, commercially available 16x16 SiPM array with 256 analog channels [46**].**

Although SiPM pixels essentially output binary signals, collectively these devices provide a way to measure light proportionally (i.e. the analog signal output from a SiPM is proportional to the number of pixels which fire) over a wide dynamic range while maintaining sensitivity to single photon events. Wangerin, *et al*., developed a passive electrical model of SiPMs with parameters derived from empirical observation of several popular SiPM models. They extended the array models developed by Pavlov and Corsi by empirically extracting physical parameters for single diode quenching resistances, stray and storage capacitances, and breakdown voltages as well as accounting for readout effects [**42**] [**43**] [**47**]. Their model for the Hamamatsu S10362-11-025C, a 40x40 array of 25μm pixels, is shown in Fig. 24.

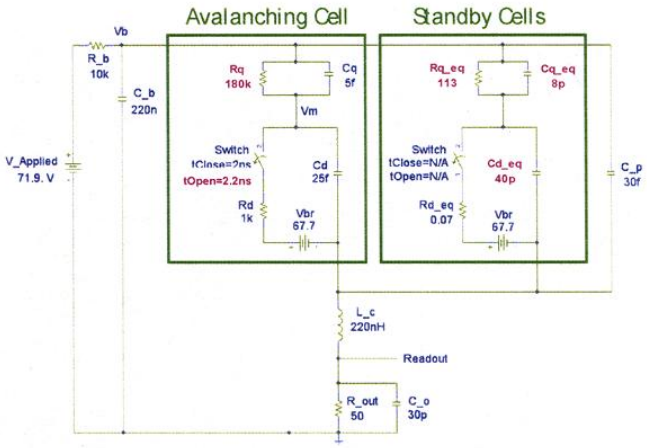

Fig. 24. Passive circuit model for a Hamamatsu S10362-11-02C, adapted from [42**]. For details, the reader is refered to [**42**].**

5. 2. SiPM Photon Detection Efficiency

Since the number of photoelectrons is typically the limiting factor in scintillator resolution, the efficiency of a photosensor is of the utmost importance for the spectroscopist. Unlike, traditional PMTs which have fairly low quantum efficiencies (e.g. 15-20%) due to the relatively large work function of the photocathode (e.g. 3-4 eV), SiPMs have high quantum efficiencies (e.g. ~70% depending on wavelength) [**4**] [**8**]. However, the overall photon detection efficiency (PDE) of a SiPM is dominated primarily on the fill factor, or ratio of active to entire device surface area, and is given by

$$PDE = QE \times \varepsilon_{Geiger}(V) \times \varepsilon_{fill-factor}, \tag{2.24}$$

where QE is the quantum efficiency, ε_{Geiger} is the probability of triggering an avalanche at a particular bias voltage, and $\varepsilon_{fill-factor}$ is the ratio of active APD area to total surface area of the SiPM. Typical PDE values are reported between 15-25% for 1600 pixel devices

and 50-75% for 100 pixel devices depending on operating characteristics and incident wavelength [**45**].

5. 3. SiPM Response Linearity

The finite number of pixels and their finite recharge time contributes to a fundamental limitation of the SiPM, namely device saturation. Although the response of SiPMs is technically a binomial random variable, the expected number of pixels that fire, $\langle N_f \rangle$, can be approximated by

$$\langle N_f \rangle = N_{pixels}\left(1-\left(1-\frac{1}{N_{pixels}}\right)^{N_{photons}\cdot PDE}\right) \approx N_{pixels}\left(1-e^{\frac{N_{photons}\cdot PDE}{N_{pixels}}}\right), \qquad (2.25)$$

for large numbers of pixels. This assumes that the pixels have an infinitesimal recharge time. The mean number of photoelectrons, $PDE \cdot N_{photons}$, per pixel determines the saturation of the device as shown in Fig. 25 for a SiPM of an arbitrary numbers of pixels and incident photons [**4**] [**48**]. As seen, the device becomes saturated when exposed to photon fluxes sufficient to produce an average of five photoelectrons per pixel in any one event (i.e. less than the pixel recharge time, typically on the order of a few tens of ns).

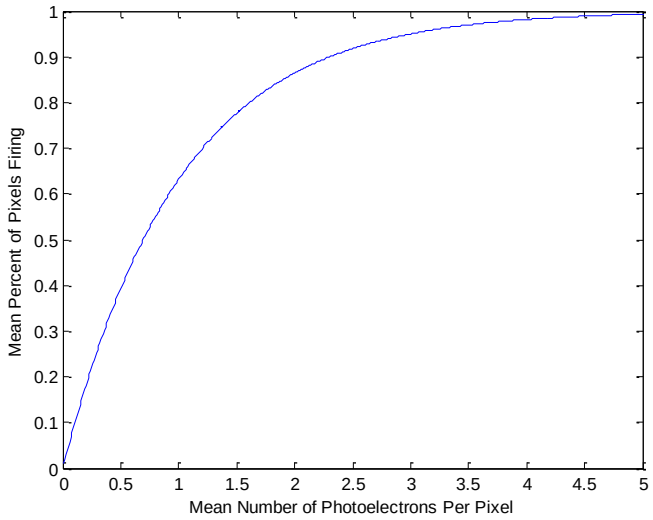

Fig. 25. The number of pixels which fire is a non-linear function of the number of photons incident upon the SiPM. Higher pixel densities offer greater dynamic ranges and less saturation.

5. 4. Dark Counts, After pulses, and Cross-talk

Several sources of noise affect the performance of SiPMs; first and foremost are dark counts. Somewhat analogous to dark current in PMTs, dark counts occur when an electron is thermally released from a shallow trap in the active area of the SiPM, thereby causing an avalanche event. The probability of this phenomenon is proportional to temperature and operating voltage, due to the probability of avalanche breakdown, ε_{Geiger}. Dark count rates of several hundred thousand to a few million hertz per square millimeter can be expected, depending on the device and operating conditions [**49**].

Similar in nature to the mechanisms responsible for afterglow response of scintillating crystals, after pulses are caused when charge carriers produced in avalanches are temporarily and shallowly trapped during their migration before being thermally released after quenching causing another avalanche event. The probability of this

phenomenon is likewise proportional to temperature and, in particular, operating voltage. Since the electron multiplication during avalanche is directly proportional to the difference between the bias and breakdown voltage, increasing the operating voltage releases more electrons and, thus, further increases the probability of trapping and after pulsing.

Cross-talk between SiPM pixels (really CMOS photodiode pixels, in general) occurs when a pixel discharge causes the release of charge in a neighboring pixel. It is generally accepted that hot-carrier luminescence is responsible for pixel cross-talk due to the marked improvement of sensors with the implementation of deep, optically isolating pixel trenches [**4**]. Cross-talk increases proportionally to the inverse square of the pixel pitch (i.e. as the closer the pixels, the worse the cross-talk), and thus is expected to scale with the area of SiPM. Cross-talk also increases with operating voltage. Teshima, *et al*., suggest that the probability of cross-talk experiences "a kind of saturation" depending on the number of pixels firing [**4**].

5. 5. SiPM Amplitude Resolution Limitations

Random fluctuations in photon production, transport, and counting degrade the achievable amplitude resolution of any scintillator based detection system. For the purposes of this discussion, the amplitude resolution of any system is defined as the ratio of the variation in signal amplitude (i.e. the full-width-at-half-maximum, FWHM) to the magnitude of the signal amplitude.

The statistics of photon counting follow Poisson statistics; that is, the dispersion in the number of measured photons is $\sqrt{N_{Photons}}$, in general for linear detectors.

However, as discussed, SiPM are non-linear devices which saturate as the mean number of photoelectrons produced per pixel increases. Therefore, in addition to Poisson fluctuations, signal dispersion in the device results from saturation and further degrades and limits the intrinsic detector resolution.

Stoykov, *et al*., have described this overall intrinsic detector resolution of an ideal SiPM (i.e. a device without cross-talk, after pulses, or dark counts) in [**48**]. They show the resolution (i.e. the FWHM) due to signal saturation as

$$R_0 = 2.35\sqrt{\frac{\exp(\alpha)-1-\alpha}{N_{pixels}\cdot\alpha^2}}, \tag{2.26}$$

which monotonically increases with $\alpha = PDE \cdot N_{photons} / N_{pixels}$, which represents the mean number of photoelectrons per pixel. They also show that the resolution due to Poisson statistics is

$$R_{stat} = \frac{2.35}{\sqrt{PDE \cdot N_{photons}}} = \frac{2.35}{\sqrt{N_{pixels}\cdot\alpha}}. \tag{2.27}$$

Finally, the resulting overall ideal SiPM resolution is the quadrature sum of the two components,

$$R = \sqrt{R_0^2 + R_{stat}^2} = \frac{2.35}{\sqrt{N_{pixels}}}\frac{\sqrt{e^{\alpha}-1}}{\alpha}. \tag{2.28}$$

The overall intrinsic resolution of an ideal SiPM is graphed as a function of the mean number of photoelectrons per pixel, α, in Fig. 26.

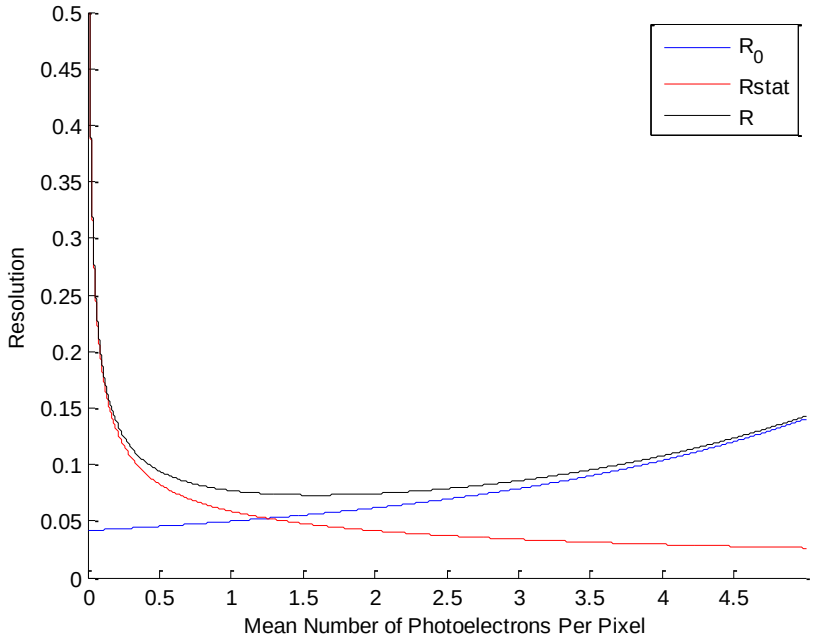

Fig. 26. The overall intrinsic resolution (FWHM) of an ideal SiPM is graphed as a function of the mean number of photoelectrons produced per pixel, shown here for a SiPM with 1600 pixels. Poisson statistics dominate the resolution limit when σ_N / N is large. While relative dispersion due to Poisson statistics improves at higher photon fluxes, eventually the SiPM becomes saturated and the dominating source of signal dispersion and degraded resolution.

From (2.28), it is seen that the overall intrinsic resolution of a SiPM is a function of the mean number of photoelectrons per pixel, α, which conveniently has a minimum at $\alpha = 1.59$ for any SiPM independent of PDE or N_{pixels}. Importantly, however, the overall resolution increases proportionally to the square root of the number of array pixels; thus, the minimum resolution is $2.92/\sqrt{N_{pixels}}$ at $\alpha = 1.59$. This satisfies intuition since the linearity, and thus the saturation, of the device is dependent on the number of pixels available to fire. This is shown for various SiPM arrays in Fig. 27.

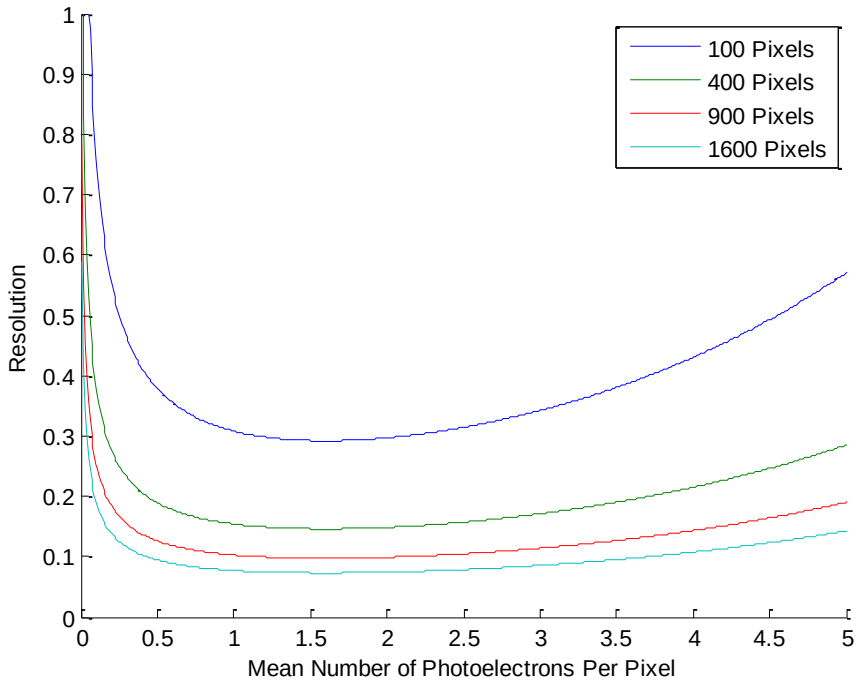

Fig. 27. The overall intrinsic resolutions (FWHM) of SiPMs with various array sizes are shown. Interestingly, the minimum resolution is independent of the mean number of photoelectrons, thus the number of incident photons. However, minimum resolution improves as the square root of the number of pixels.

In addition to the fluctuations of ideal SiPMs, dark counts, after pulses, and cross-talk further degrade the achievable energy resolution of real SiPMs. The decay time of a scintillator therefore becomes critically important in terms of the achievable energy resolution of the system because the longer the required signal integration time, the more noise will be integrated as well. According to Johnson, *et al*., the "excess noise factor" contributes to energy resolution degradation only when the dark counts are on the same order as the number of pixels which fire [**50**]. Recall from (2.5), the brighter and faster the scintillation pulse the higher the Birks' figure of merit and additionally the lower the contribution to energy resolution performance from intrinsic SiPM (and any detector in general) noise sources.

While Stoykov's analytical model provides useful insight into the inherent signal dispersion of an ideal SiPM, it fails to consider the temporal effects of signal integration. There are few scintillators (organics being a notable exception) that have decay times on the order of, or faster than, the recharge time of a SiPM pixel. As a result, most scintillator readout electronics must include some shaping time over which the light pulse is integrated. Consequentially, it is not safe to neglect the effects of noise integration from dark counts, after pulses, or cross-talk.

In response, Johnson, *et al*., propose the *effective* number of available pixels be defined as

$$N_{pixels}^{eff} = N_{pixels} \frac{\tau_{shape}}{\tau_{recharge}}, \tag{2.29}$$

where $\tau_{recharge}$ is the pixel recharge time and τ_{shape} is the shaping time of the readout circuit. According to Johnson, *et al*., the amplitude resolution of the SiPM can be described by two response regions: 1) the linear region in which no more than 30% of the pixels fire and 2) the non-linear region in which more than 30% of the pixels fire. They show in [**50**] that the SiPM component of the overall energy resolution of the detector system as a function of energy in the linear region can be written as

$$\left(\frac{\sigma_E}{E}\right)^2 = F\left(\frac{1}{N_f} + \frac{N_{DC}}{N_f{}^2}\right), \tag{2.30}$$

where F is an empirically measured excess noise term generated from cross-talk and after pulsing during the integration time, N_{DC} is the expected number of dark counts during the integration time, and N_f is the number of pixels which fire as a result of detected photons. Finally, Johnson, *et al*., argue that binomial statistics best describe the

SiPM response in the non-linear region from which the amplitude resolution in terms of triggered pixels has been shown to be

$$\left(\frac{\sigma_{N_f}}{N_f}\right)^2 = F\left(\frac{1-\frac{N_f}{N_{pixels}^{eff}}}{N_f} + \frac{N_{DC}}{{N_f}^2}\right) \tag{2.31}$$

It is important to note that the signal dispersion described by (2.31) is in terms of number of pixels fired and must be appropriately converted into amplitude using (2.25). For full treatment and more complete discussion, the reader is referred to [**50**].

III. Experiments

Fiber shaped inorganic scintillators coupled to SiPMs are promising new radiation detector concept for particle tracking and standoff detector applications. This chapter describes experiments and simulations conducted using YAG:Ce fiber crystals with fiber end SiPM readout. The goal of these experiments is to determine the achievable energy and position resolution of such a detector system.

1. Multi-Pixel Photon Counter Investigation

Paramount to the successful implementation of a compact, ruggedized, and deployable scintillation detector is the SiPM. In contrast to PMTs, the SiPM is a relatively new photosensor with emerging theoretical models to describe its signal response and dispersion. Consequently, much of the focus of this research is centered on the signal response of SiPMs.

The Multi-Pixel Photon Counter (MPPC) is the trademarked SiPM manufactured by the Hamamatsu Photonics company in Japan. The MPPC was chosen for this research due to its relative popularity in industry and literature. The MPPC model S10362-025C SiPM contains a 40x40 array of G-APD pixels on a 1 mm^2 CMOS chip which is housed in a ceramic casing with a layer of optical epoxy protecting the active surface. This particular model was chosen for these experiments because of the dynamic range provided by the large number (1600) of pixels. Similar models are commercially available with 100 and 400 pixels; all three arrays are available in metallic or ceramic packaging as well as surface mountable chips. The S10362-025C, henceforth referred to as the *MPPC*, is shown in Fig. 28.

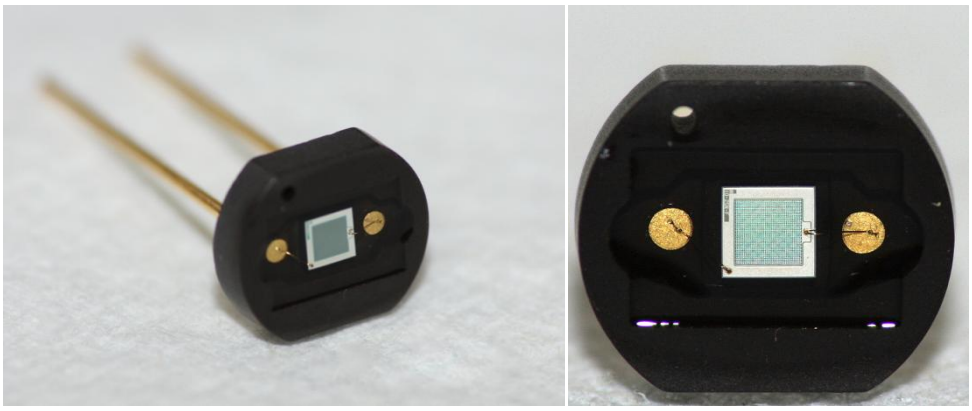

Fig. 28. The Hamamatsu model S10362-025C MPPC is shown. The photosensitive area in the center of the ceramic package is 1x1 mm^2, contains 1600 active G-APD pixels, and lies underneath a layer of protective optical epoxy.

This section describes the calibration process and several experiments and simulations conducted in order to ensure proper understanding of the MPPC response to scintillation.

1. 1. MPPC Readout Circuit

The readout circuit of the MPPC was constructed using conventional electronic components and a prototype printed circuit board (PCB). Coaxial cables (RG-178U) were used to provide the bias voltage to and carry the signal away from the MPPC PCB. The readout was designed for a voltage sensitive configuration using a 50 Ω load resistor. Two MPPCs, each with their own identical readout circuit, were used throughout these experiments. The circuit schematic is shown in Fig. 29.

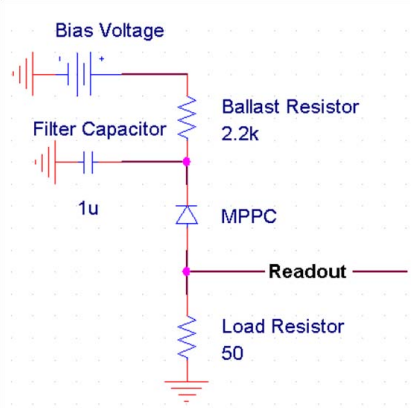

Fig. 29. The MPPC readout circuit used during the experiments is shown. The MPPC is typically biased a few volts above breakdown, nominally 71-72 V.

1. 2. MPPC Readout Circuit Modeling and Simulation

This readout circuit is of the basic form suggested by Hamamatsu and has been widely publicized in the scientific literature [**4**] [**45**] [**49**]. As discussed in Section II. 5. 1. , this circuit has been extended by Wangerin, *et al*., to include an empirically derived passive model for the discharging MPPC, see Fig. 21 [**42**]. Their circuit model was modified using Orcad Capture 16.3 PSPICE software [**51**] to match the values of the readout circuit shown in Fig. 21. In addition, the model was expanded to allow the user to select and sweep through any number of pixels which fire and allows the simulation of repetitive pixel firings (i.e. either after pulsing or retriggering). This expanded model parametrically adapts the values of active and standby components in pixel cells and is only limited by processing time and available memory. The expanded circuit model is shown in Fig. 30.

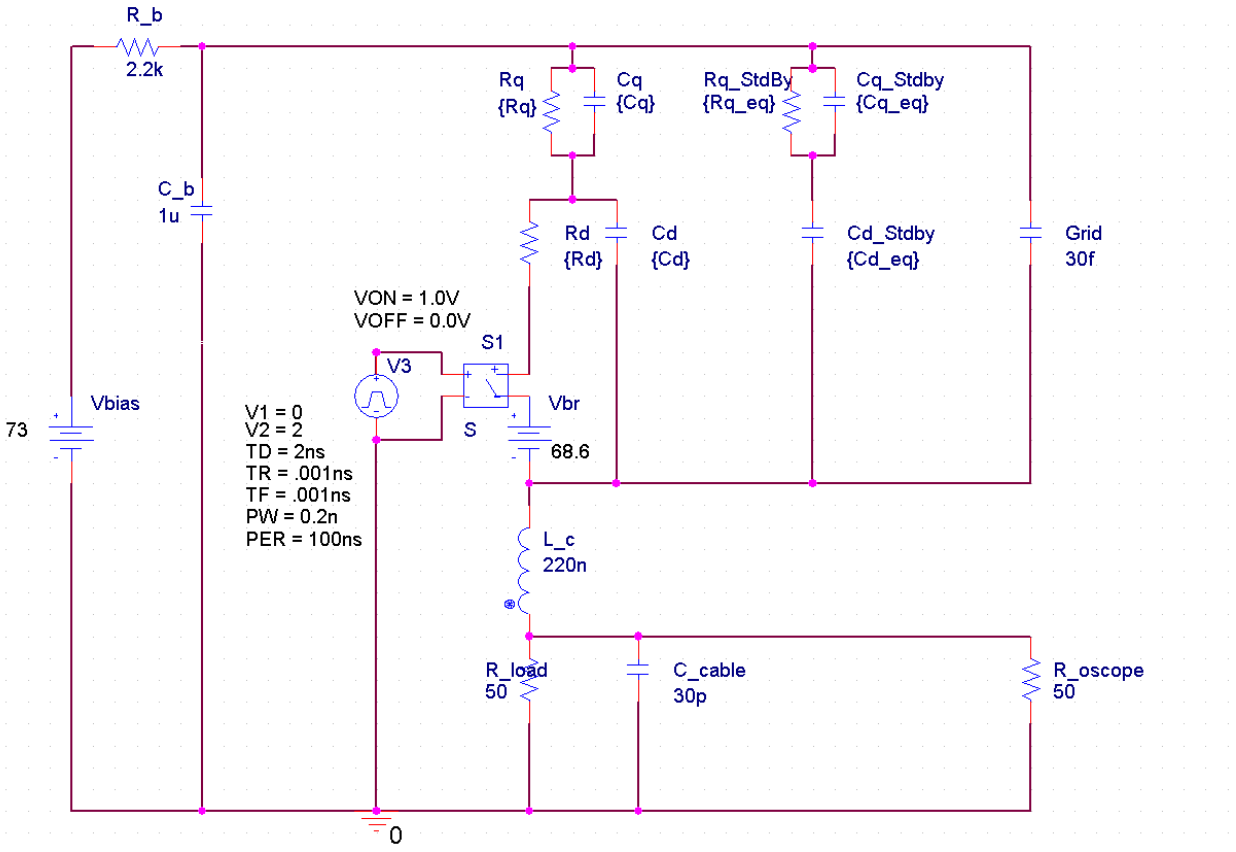

Fig. 30. The passive circuit model of an MPPC first developed by Wangerin, *et al.*, has been expanded as shown. Additional features include scalable and selectable parameterized component values which allow modeling pixel firing across the dynamic range of the device as well as the capability to model repetitive pixel firings or after pulses.

The expanded circuit model used the values reported by Wangerin, *et al.*, for the passive components. Only the bias voltage, breakdown voltages, ballast resistor and filter capacitor values were modified. No attempt to empirically extract MPPC parameters was made, rather the values reported in [**42**] were parameterized. That is, the user specifies the number of pixels which fire, n, which control the component values according to basic electrical circuit theory for series and parallel equivalence. The equivalent resistor and capacitor components values in the expanded circuit model are

$$
\begin{aligned}
R_q &= \left(\frac{1}{n}\right) 180\,\mathrm{k}\Omega \\
R_q^{Stdby} &= \left(\frac{1}{1600-n}\right) 180\,\mathrm{k}\Omega \\
R_d &= \left(\frac{1}{n}\right) 1\,\mathrm{k}\Omega \\
C_d &= (n)\, 25\,\mathrm{fF} \\
C_d^{Stdby} &= (1600-n)\, 25\,\mathrm{fF} \\
C_q &= (n)\, 5\,\mathrm{fF} \\
C_q^{Stdby} &= (1600-n)\, 5\,\mathrm{fF}
\end{aligned}
\quad . \qquad (3.1)
$$

During the bulk of the experiments, signal amplitudes from this readout circuit were sufficiently large enough that they could be digitized directly using a Tektronix DPO7104 digital oscilloscope capable of 10-GSa/s with 1-GHz of bandwidth. The oscilloscope was used primarily as a fast analog-to-digital converter (ADC) and was controlled by a laptop to transfer the digitized waveform data over Transmission Control Protocol (TCP/IP). Under the occasional circumstance, MPPC readout signals could not be directly digitized because of the oscilloscope noise floor (around 0.7-1 mV at 1 GHz of bandwidth). For example, even using a relatively large bias voltage and modest breakdown voltage (e.g. 73 and 68 V, respectively) in the MPPC readout circuit model, one should expect maximum signal amplitudes of less than 500 μV per pixel fired, as shown by the simulated single pixel response in Fig. 31.

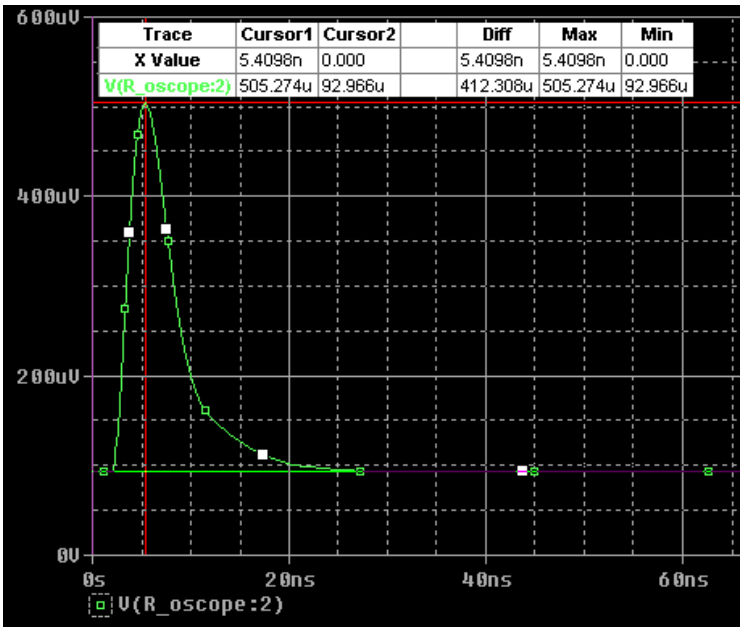

Fig. 31. The simulated response of a single pixel within a MPPC firing is shown. The maximum amplitude is less than the noise floor of the Tektronix DPO7104 oscilloscope.

Therefore, in order to observe single pixel firing events with the oscilloscope, an Ortec 9306 1-GHz fast preamplifier was required.

1. 3. MPPC Calibration

Dark counts provide a convenient way to calibrate each device and, until such time when device manufacturing shows better uniformity, each MPPC must be uniquely calibrated for the best results. Sophisticated systems may require independent bias circuits for each device to ensure uniform operating characteristics, such as pixel gain. This, of course, is complicated by the temperature dependent nature of the MPPC response and, indeed, all SiPMs in general. However, during this research all MPPC experiments were conducted at ambient, uncontrolled room temperature (i.e. ~20-25°C) using only a single bias supply voltage for all MPPCs to limit interfaces with the dark box.

Dark count calibration of MPPCs requires the measurement of a single pixel firing and subsequent cross-talk events caused by thermally excited electrons which initiate avalanches within the active area. As a consequence of the relatively low single pixel signal amplitude, the calibration required the use and calibration of an Ortec 9306 preamplifier. First, the gain of the preamplifier was measured using a calibrated Agilent 33210A arbitrary waveform generator and the oscilloscope (using a 1 GSa/s sampling rate). Next, the MPPCs were placed in a light tight box made from a polycarbonate case which was modified with RG-59 bulkhead connectors to supply the bias voltage and readout channels. The average dark count rate was measured with the MPPC inside the polycarbonate dark box. A dark count rate of 200-300 kHz (increasing with bias) was measured and is within the manufacturer's specification, indicating a reasonable light tight seal. The maximum amplitudes of 24,000 dark counts at four different bias voltages were recorded and the results from one MPPC have been corrected for preamplifier gain and are shown in a histogram in Fig. 32. The results of this calibration is discussed in Section IV. 1. 1.

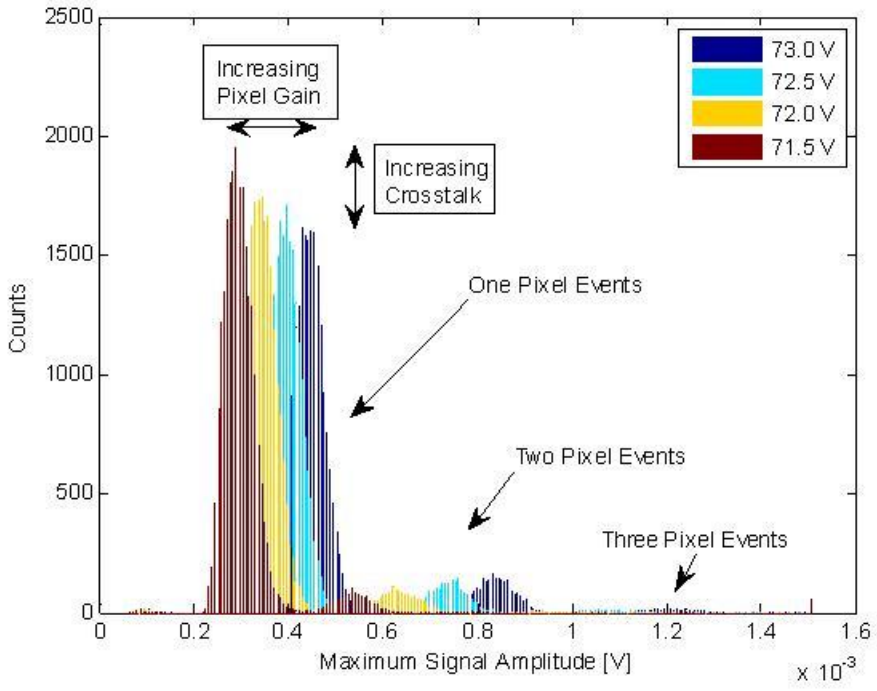

Fig. 32. The dark count pulse height spectrum from MPPC#1 is shown at four different bias voltages. There are three distinct sets of peaks which correspond to the single, two, and three pixel events which result from dark counts and pixel cross-talk. The cross-talk probability and pixel gain clearly increases with bias voltage.

1. 4. MPPC Scintillator Response Experiment and Simulation

Prior to conducting any experiments with long, unconventional YAG:Ce fibers, the response of the MPPC was independently tested by measuring the time domain fluorescence decay profile and pulse height spectrum from another common scintillator material. A 1x1x12 mm^3 cerium activated lutetium-yttrium oxyorthosilicate (LYSO:Ce) crystal was coupled on its end to the MPPC using BC-630 (n=1.46) optical grease. LYSO:Ce is a bright (~28,000 ph/MeV) and fast scintillator which, unlike YAG:Ce, has only one fast component around 42 ns [**52**]. Additionally, LYSO:Ce has the same refractive index as YAG:Ce (n=1.82). The LYSO:Ce sample used in this experiment was grown via the μ-PD method by Fibercryst. The end was cut and polished and the crystal

was wrapped in several layers of Teflon tape by the author. Consequently, the optical quality of the surface treatments may be somewhat questionable.

The scintillation response of the LYSO:Ce to gamma radiation from a ^{22}Na point source was measured directly via the MPPC readout circuit (72.0 V bias) using the oscilloscope. Using a rising edge trigger, 100,000 digitized waveforms were collected, each 250 ns in duration. The time domain fluorescence decay measurements of LYSO:Ce were used to confirm proper MPPC response to a scintillation pulse. A typical pulse is shown below in Fig. 33. The measured data and experimental results are presented in Section IV. 1. 3. in Fig. 42 and Fig. 43.

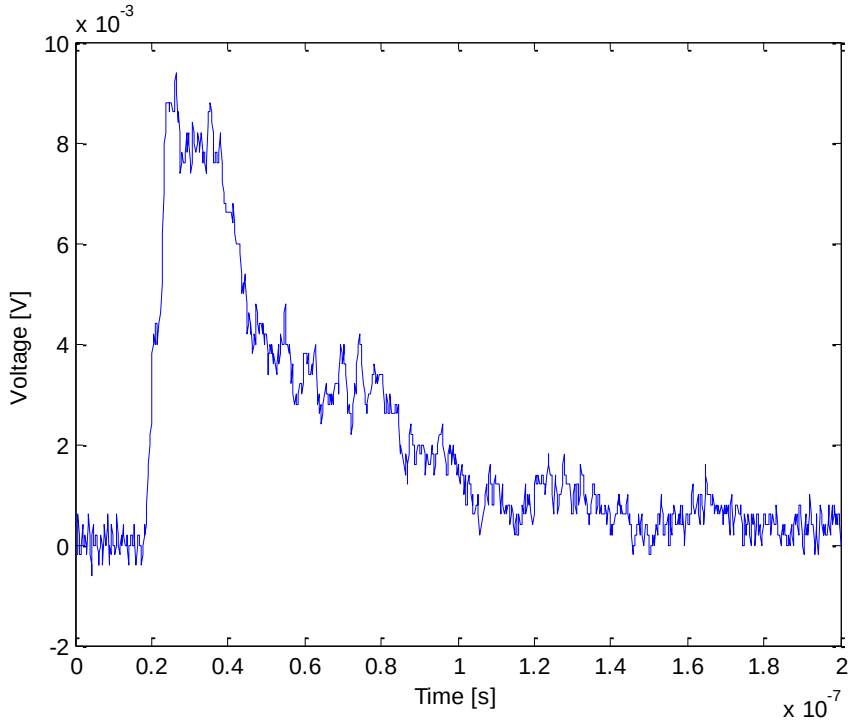

Fig. 33. A typical digitized LYSO:Ce gamma scintillation pulse as measured directly using the MPPC readout circuit and 1 GSa/s oscilloscope is shown.

To complement the LYSO:Ce MPPC measurements, the experiment was simulated using DETECT2000 [**53**], a Monte Carlo based software program designed to model the optical properties of scintillators. DETECT2000 uses optical ray tracing to track user defined quantities of randomly polarized scintillation photons throughout the scintillator medium and any optical coupling medium such as wavelength shifters or light pipes until the photons are either lost due to escape, absorption, or detection. The photons are born in accordance with the user defined decay time profile which is written as a series of weighted exponential sums. The user specifies the refractive indices and geometries of all materials and detectors; the user must also specify the surface models which correspond to different optical processes at optical interfaces. For example, a surface can be defined as painted or metallic (requiring reflectivity coefficients) which correspond to diffuse or specularly reflective surfaces, respectively. Surfaces that are specified as ground or polished are modeled using refraction and Fresnel reflections associated with the changes in refractive index; the difference in the two models is the degree of surface roughness modeled using micro-facets. More complicated model parameters such as the amount of surface roughness, the reflectivity coefficients, and backscatter intensities can also be adjusted to match empirical data. Other helpful features include the calculation of time of arrival, path length traveled, and a spatial distribution tally of each scintillation photon at the detector surface [**54**].

The simulated LYSO:Ce crystal was assumed to produce 14,000 photons for each 511 keV gamma ray associated with positron annihilation from the ^{22}Na source. The simulated decay time was modeled as a single exponential with a 42 ns decay time. Five of the six LYSO:Ce crystal surfaces were modeled using the paint surface treatment with

a reflection coefficient of 0.95 which treats each surface as a 95% efficient Lambertian reflector to represent the Teflon tape. The sixth and final crystal surface was modeled to include refractions and reflections strictly due to changes in refractive index (i.e. optical refractions and Fresnel reflections). The detector surface was assumed to be 100% efficient with a thin coating of n=1.46 coupling compound. The DETECT2000 code is available in Appendix A1.

The results of the DETECT2000 simulation were processed to form a time series of unit delta functions which represent the arrival of photons on the MPPC surface as a function time. A separate Monte Carlo routine determined which of the photons would produce avalanche pixel discharge in accordance with the PDE specified in the Hamamatsu product sheet at the peak wavelength of YAG:Ce emission (PDE=15% at 550 nm) [**45**]. This final time dependent series of unit deltas represented individual pixels firing assuming independence (i.e. no pixel could fire before being reset) and was convolved with the simulated response of a single pixel firing at bias voltage of 72 V using the expanded MPPC readout circuit PSPICE model. The result is a fully simulated LYSO:Ce 511 keV gamma ray scintillation pulse as would be observed via the readout electronics, the results of which can be found in Fig. 45 and Fig. 46 of Section IV. 1. 3.

2. YAG:Ce Fiber Crystal Investigation

The other key component in this research, the YAG:Ce fibers, were grown by the Fibercryst company in cooperation with the University of Lyon in Lyon, France. The YAG:Ce cylindrical fibers were grown in an iridium crucible and extruded via the µ-PD method with an outer diameter of 400 µm in an inert, argon atmosphere. The fibers were cut to a length of 100 mm and the ends were polished by Fibercryst. A total of 36

YAG:Ce crystal fibers have been procured for this research, four of which are prepackaged by Fibercryst in a 2x2 bundle with a clear polyethylene cladding. However, only six individual fibers are subject to the bulk of these experiments.

The vast majority of the YAG:Ce experiments were conducted using dual fiber end MPPC readout. In order to repeatedly couple various fibers to the same set of MPPCs, an aluminum vice mount was designed and custom manufactured at the AFIT Model Shop. The vice mount, fiber, and MPPCs were housed in a black polycarbonate dark box with three RG-59 bulkhead connectors. An illustration of the custom vice mount is shown in Fig. 34.

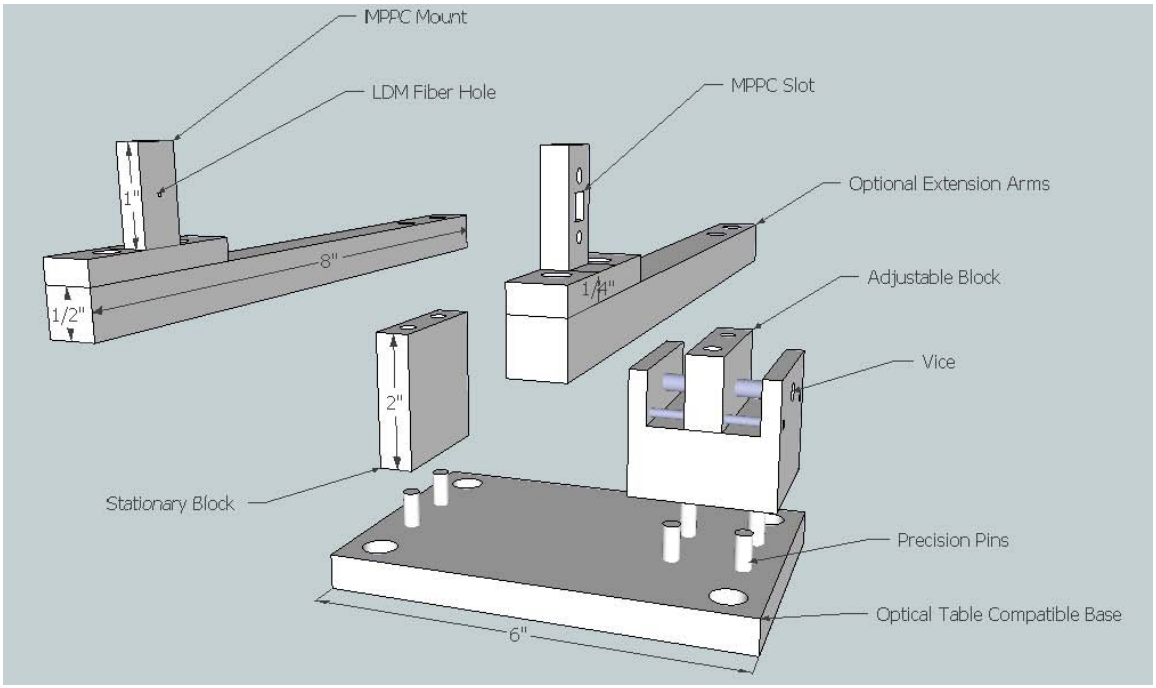

Fig. 34. The custom manufactured MPPC and YAG:Ce fiber vice mount is illustrated.

The six YAG:Ce fibers under study were chosen randomly from the original shipment of 12. The six fibers were assigned a unique number and for the sake of

compact notation will henceforth be referred to as F1, F2, etc., through F6. The first set of experiments intended to show proper MPPC response to the YAG:Ce scintillator. However, upon irradiating the detector system with gamma rays, it became immediately apparent that the low density, low effective Z, and small volume of the individual YAG:Ce fibers made for a very inefficient gamma detector material. Low count rates from a bare source indicated that measurements made via narrow collimation would be impractical with the available laboratory sources. As a result, the position resolution measurements originally planned for a collimated gamma source were modified for a collimated alpha source. Evidence for these claims and further quantitative discussion is provided in Section IV. 2. 2.

An ^{241}Am alpha source was selected because the mean range of the 5.4 MeV alpha associated with its decay has a range in excess of 4 cm in dry, sea level air [**8**] [**55**]. However, the mean range of that alpha in YAG:Ce is less than 20 μm, calculated using The Stopping and Range of Ions in Matter computer code (SRIM 2008.04 [**56**]). According to the SRIM tables, the linear stopping power of a 5.5 MeV alpha in dry, sea level air is 892 keV per cm. The full results of the SRIM table calculations are shown in Appendix A3.

The alpha source was placed 5.8 mm directly below the YAG:Ce fiber on a wooden block to minimize alpha straggling in air. Only alphas produced on or near the surface of the ^{241}Am source can escape the material with enough energy to interact within the YAG:Ce fibers. Those alphas which do interact lose very little energy in transit and are sure to deposit the entirety of their energy within the scintillator in a range of 20 μm and are expected to produce a bright scintillation light pulse.

2. 1. YAG:Ce Scintillation Properties Investigation

The initial YAG:Ce experiment was intended to characterize the time domain fluorescence decay profile and amplitude of scintillation pulses from each of the six fibers measured directly from the MPPC readout. For this initial experiment, no collimation was used; rather, a bare ^{241}Am source was placed 5.8 mm directly underneath the fiber under test, well below the mean range of 4 cm. Due to the long decay times of YAG:Ce combined with its overall lower light yield when compared to LYSO:Ce (Birks' figure of merit values $M_{YAG} \approx 68$ and $M_{LYSO} \approx 650$ ph ns^{-1} MeV^{-1}), the MPPC bias was increased to 73V at the risk of increased quantities of dark counts, after pulses, and cross-talk in order to increase the signal-to-noise ratio on the oscilloscope.

For each of the six fibers under study, 1600 alpha particle scintillation pulses were readout via MPPCs, directly digitized by the oscilloscope, and stored on the laptop controller. Additionally, digitized scintillation waveforms for one fiber, F6, were collected during gamma irradiation from a bare ^{22}Na source. This fiber was tested both bare and wrapped with several layers of Teflon tape. These waveforms were digitally processed to compare the fluorescence decay profiles to the values published in literature. The results can be found in Section IV. 2. 1.

As with the LYSO:Ce experiment, the YAG:Ce fiber experiment was modeled in DETECT2000. Scintillation parameters from Ludziejewski, *et al.*, were chosen for this model [**32**]. Specifically, a light yield of 17,000 ph/MeV was selected and an α/γ ratio of 21% was applied; therefore, the 5.4 MeV α-particle was assumed to produce 17,000 scintillation photons (approximately accounting for energy lost due to particle straggling). Two decay constants, 88.9 ns and 458.5 ns, were chosen with two

independent intensities, 14.9% and 85.1% respectively (refer to Table 1). The refractive index of the 400 μm diameter by 100 mm long cylindrical YAG:Ce fiber was set to 1.82 and the emission wavelength was set to 550 nm, the emission peak of YAG:Ce. Air was used as the fiber cladding (n=1.00). Importantly, the surface treatments were modeled as polished; this surface model applies only refraction and reflection due to changes in the refractive index between the air and the fiber. The two fiber ends both had 100% efficient detectors with a thin coating of index matching fluid (n=1.46). Again, the data from DETECT2000 was processed and convolved with the MPPC single pixel response to produce a fully simulated YAG:Ce 5.4 MeV alpha particle scintillation pulse as measured via the readout electronics. The DETECT2000 code is available in Appendix A2. These results are presented in Fig. 49 and Fig. 50 of Section IV. 2. 1.

2. 2. YAG:Ce Energy Spectrum and Resolution Measurements

Energy calibration measurements were taken using the YAG:Ce fibers coupled to a single fiber end MPPC readout and compared to a single fiber end PMT readout. Unlike conventional scintillation detectors, energy calibration using dual fiber end readout requires careful collimation of the particles rather than direct irradiation from a bare source. A bare source would result in a much wider spread in the spatial position of interaction along the fiber which would reduce the overall energy resolution because of varying amounts of scintillation photon absorption. This light attenuation property will later be exploited to estimate the position-of-interaction.

For the MPPC readout experiments, an ^{241}Am alpha source was collimated using a 4.7 mm (3/16”) thick circular aluminum plate with a 1 mm diameter hole drilled out. The alpha source was placed 5.8 mm directly underneath the center of the mounted

YAG:Ce fiber. In this configuration, the spread of alpha particles along the length of the fiber is limited to 2.4 mm (see Appendix A4). This experiment was setup to minimize variation in the amount of scintillation light produced and detected in the YAG:Ce fiber.

In addition to alpha radiation, several gamma sources were also collimated and used to irradiate the YAG:Ce fibers during MPPC readout. Again, because of the low count rates from gamma irradiation of YAG:Ce, the energy resolution measurements from a ^{22}Na source were taken using only one fiber, F6. These sources were placed behind a one inch thick lead brick with a 1 mm diameter hole removed for collimation. The resulting spread of the gamma beam at distance of three inches is 6 mm.

The YAG:Ce energy resolution measurements were made using the photodetector (i.e. either MPPC or PMT) connected in series to a Cremat CR111 charge integrating preamplifier, an Ortec 672 shaping amplifier with a 1 μs shaping time, and an ADCAM multi-channel analyzer. These results can be found in Section IV. 2. 2.

2. 3. YAG:Ce Position Resolution Measurements and Simulations

Position resolution experiments were conducted on YAG:Ce fibers using dual fiber end MPPC readouts by two sources of excitation, laser induced photoluminescence and alpha scintillation. The premise behind these experiments was that position-of-interaction information could be inferred from differences in scintillation light intensity measured at opposite ends of YAG:Ce fibers by MPPCs in accordance with (2.13). Only five fibers were used in these experiments, F1-F5; F6 remained wrapped with Teflon tape which would significantly reduce or eliminate the probability of alpha interaction within the fiber.

The photoluminescence experiments were conducted using a 405 nm solid state laser to excite the Ce^{3+} activator at various positions along the length of the fibers (refer to Fig. 11). The laser beam width of 2.65 mm (FWHM) was determined by measuring the light intensity while scanning the beam across the surface of an MPPC (see Appendix A4; the beam was assumed to be Gaussian in shape. Throughout the experiment, the MPPC bias was reduce to 71.5 V because of the high intensity of laser light. A graduated neutral density filter was adjusted to reduce the laser intensity until the YAG:Ce steady state fluorescence signal amplitude measured directly using the MPPCs was near 10 mV, well below device saturation. Saturation was determined by empirical observations. That is, the fluorescence intensity was increased by reducing laser stimulation via the graduated neutral density filter until the measured oscilloscope voltage no longer increased. This saturation occurred at approximately 50 mV, thus 10 mV was selected as a satisfactory steady state operating point between saturation and the minimum discernable level of the oscilloscope (~1 mV). These relatively low signal voltages may indicate that MPPC pixels are unable to fully recharge before being retriggered; this type of pile up may call into question this methodology and will be discussed in more detail in Section IV. 2. 3.

A mechanical chopper wheel was used to modulate the laser signal at 400 Hz and trigger the oscilloscope. It is noteworthy that these modulation frequencies were selected primarily to trigger the oscilloscope and were much too slow to capture the MPPC transient response. The MPPC signals were directly measured using the oscilloscope; 1000 sets of two channels of digitized waveform data were recorded at each position during the peak of the laser modulation for 250 ns at 1 GSa/s. Using a mirror on a

motorized calibrated rail, the laser beam was positioned at 8 randomly selected positions along the length of the fiber. The setup can be seen in Fig. 35.

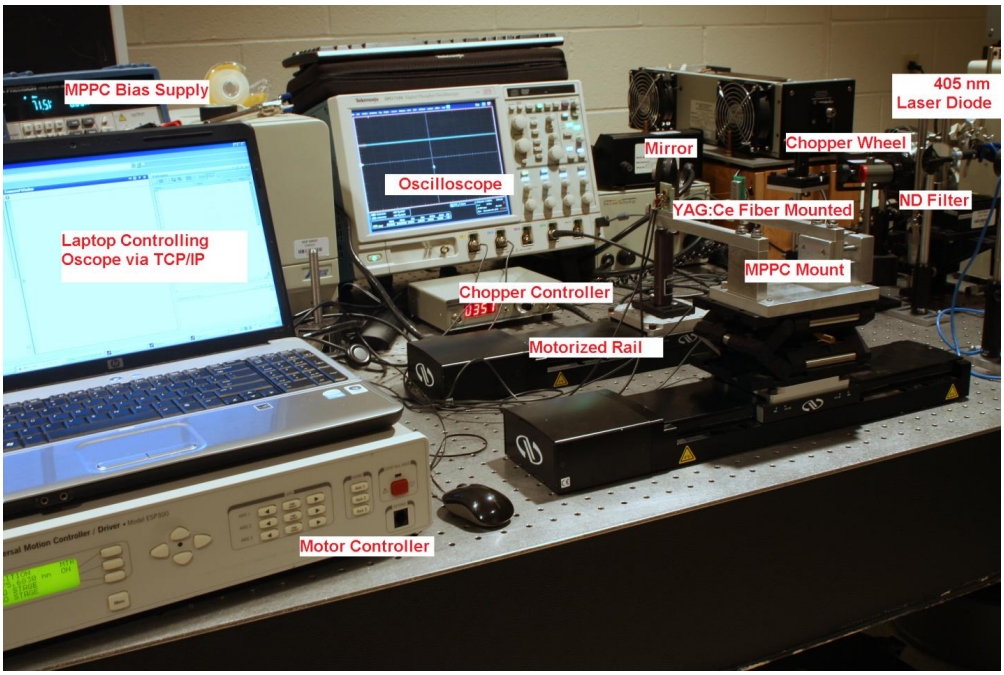

Fig. 35. Photograph of the photoluminescence experimental setup.

During the photoluminescence measurements, each of the five fibers was mounted using fresh BC-630 optical grease and measured five separate times in an attempt to quantify the repeatability of optical coupling. Due to the presence of optical imperfections (e.g. micro-bubble clusters, surface roughness, etc.) new locations of laser excitation were selected during each measurement to prevent unintentional measurement bias. That is, if an area of high concentration of optical imperfections was repeatedly excited, the increased probability of optical scattering could reduce the fluorescence light intensity measured at one or both MPPCs. A 973x scanning electron microscope (SEM)

image of a YAG:Ce fiber, shown in Fig. 36, shows potential optical flaws on the surface of the YAG:Ce fibers.

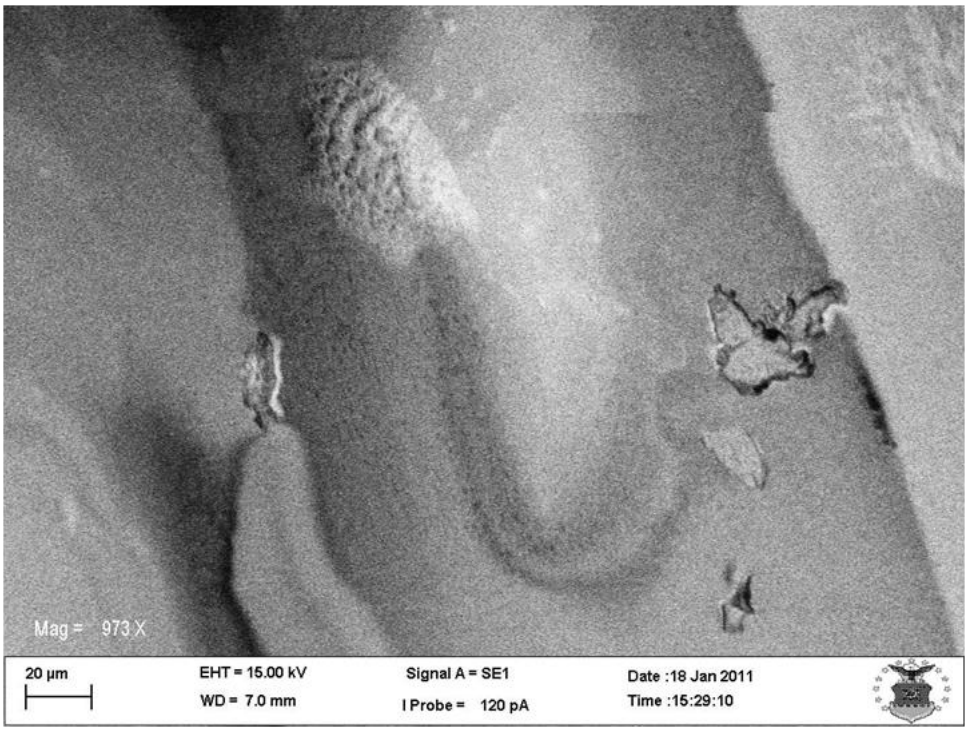

Fig. 36. A 973x SEM image of a YAG:Ce fiber shows surface imperfections such as micro bubbles, protrusions, and pits.

Position resolution in the five YAG:Ce fibers (F1-F5) was also measured in a similar manner using scintillation from alpha irradiation. During the scintillation measurements, the MPPC bias was again set to 73 V to increase the signal-to-noise as measured on the oscilloscope. The collimated ^{241}Am source described in Section III. 2. 2. was positioned by hand 5.8 mm below the YAG:Ce mounted fiber at centimeter increments along the fiber length. As described in Section III. 2. 2. , the beam of alphas irradiated a 2.4 mm section of fiber at each position. Scintillation pulse intensity measurements were made by digitizing and recording the waveform data from the two

channels of dual fiber end MPPC readout. Each waveform was collected for 1 μs at 1 GSa/s using a two channel coincidence logic trigger set just above the three pixel dark count threshold to increase the probability of detection but reduce the probability of triggering on dark count chance coincidences. That is, dark count coincidence is any event which is caused by dark counts occurring nearly simultaneously in both MPPCs (i.e. within the 10 ns coincidence gate) and above rising edge threshold of the oscilloscope trigger. Although rare, these events are not negligible due to the long count times (i.e. on the order of tens of minutes) required. Due to relatively low count rates (e.g. ~20 counts per minute, depending on beam alignment) from the collimated alpha source, only 200 waveforms were measured at each position and each fiber was freshly mounted and the measurement repeated only three times. An illustration of this setup can be seen in Fig. 37.

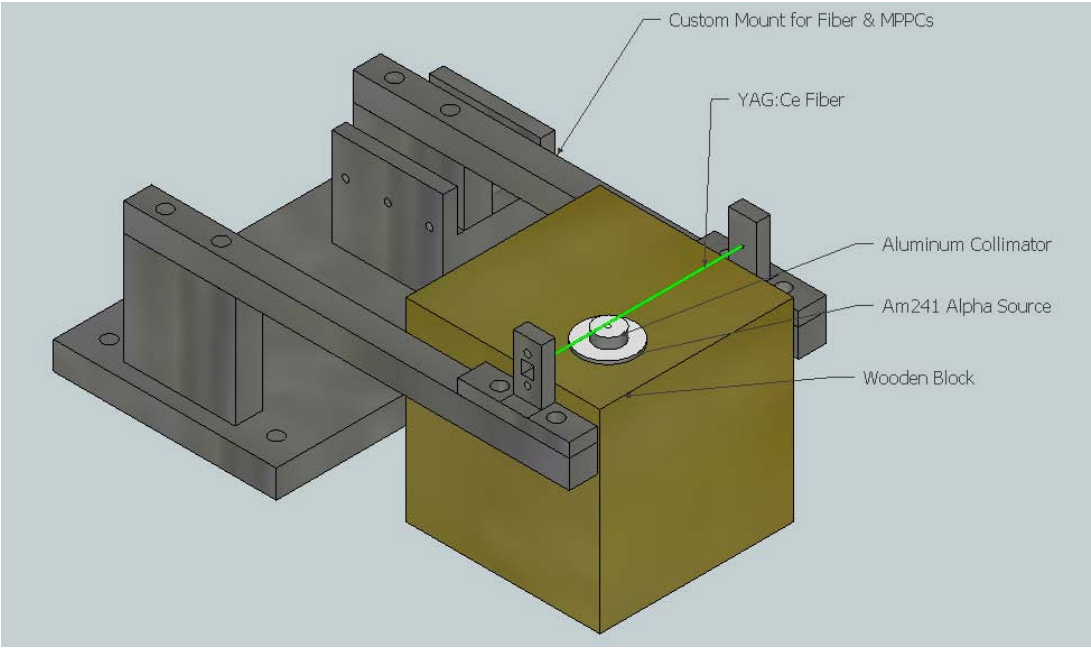

Fig. 37. An illustration of the YAG:Ce position resolution experimental setup using a collimated alpha source is shown.

This experiment was also modeled using DETECT2000 using the same 100 mm fiber modeled in Section IV. 2. 1. (see Appendix A2 for code). Three separate fibers were simulated using three different attenuation lengths, 10, 20, and 30 cm. Thirty scintillation events (17,000 photons per event) were simulated at nine positions spaced equally by 10 mm along each fiber between 10-90 mm. The number of photons measured by a single end, 100% efficient detector was recorded for each of the thirty events during the simulation of each of the three fibers.

The scintillation photon flux results of the DETECT2000 simulations were used in a separate Monte Carlo routine which modeled the random nature of the incident scintillation photon flux (i.e. the true number of photons is a Poisson distributed random variable) and the random process involved in SiPM photon counting (i.e. a binomial random variable) to determine the overall number of pixels which fire given a deterministic scintillation photon flux. The code used the mean number of scintillation photons as a function of position of interaction (i.e. as determined via DETECT2000 simulations) to select a Poisson distributed random variable representing the number of incident photons from a full energy scintillation event, N_{ph}. Using that random parameter, the code drew a binomial random variable from N_{ph} with probability PDE (e.g. 15% for the MPPC) representing the resulting number of pixels which fired. This experiment was repeated 50,000 times to estimate the best-case expected value and variance in the number of pixels which fire given a known scintillation pulse (i.e. given the expected value of the scintillation light yield) without the effects of excess noise (e.g. electronic noise, after pulses, crosstalk).

Ultimately, the results from these simulations were processed in the same manner as the measured data. First, the number of pixels fired was determined and assumed to be directly proportional to the number of incident photons. This assumption is valid for small numbers of incident photons with respect to the number of *effective* pixels, see (2.29). Next, the attenuation length was estimated by inverting (2.13) and using a linear-least-squares fit to determine the slope of the plot of $\log[\overline{N}_2(x)/\overline{N}_1(x)]$ as a function of interaction positions, *x*. Note that the attenuation length is determined by taking the logarithm of the ratio of the mean number of photons at each fiber end; $\overline{N}_i$ is the average number of fired pixels from the i^{th} MPPC due to a scintillation pulse occurring at position *x* along the fiber axis. Finally, using the empirically measured (i.e. estimated) attenuation length, the position of interaction was estimated on an event-by-event basis. The standard deviation of the data is said to be the position resolution. The results are found in Section IV. 2. 3.

IV. Results and Analysis

The results of the experiments and simulations using YAG:Ce fibers and MPPCs are presented, analyzed, and discussed in this chapter. This chapter begins with the results of the MPPC calibrations and sanity checks; measured signals are compared to simulations and LYSO:Ce scintillation decay time measurements are compared to published values. YAG:Ce fiber scintillation properties and the results of energy and position-of-interaction resolution measurements and simulations are presented and discussed. Finally, the chapter concludes with a discussion of practical and quantifiable means of improving the fiber scintillator system for future research.

1. MPPC Findings

This section describes the significant results of the MPPC calibration measurements, simulations, and scintillation response measurements.

1. 1. MPPC Breakdown Voltages and Cross-talk

By using the dark counts and subsequent cross-talk, key parameters (e.g. breakdown voltage, pixel gain, and pixel capacitance) of the MPPC can be determined as described in Section III. 1. 3. These values are critical for proper simulation of the MPPC signal response using the PSPICE model. As such, the results are presented first.

Two MPPCs were the primary readout devices throughout these experiments. A dark count pulse height calibration histogram of MPPC#1 can be found in Fig. 32. In Fig. 38, the dark count pulse height calibration histogram of MPPC#2 is shown.

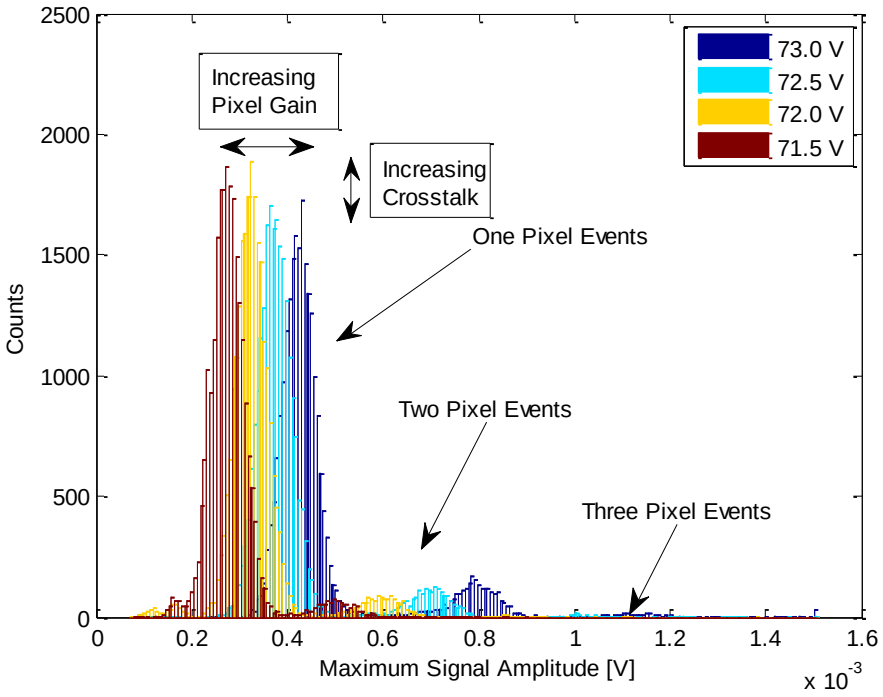

Fig. 38. MPPC#2 dark count pulse height spectrum is shown for four bias voltages. The amplitude of the pulses is linearly dependent on excess bias. As shown, cross-talk probability increases with bias voltage.

Using the peak amplitudes of the dark count pulse height spectra, one can determine the single pixel response as a function of bias voltage. The breakdown voltage can be determined by the x-intercept of a plot of the single pixel response as a function of bias voltage, see Fig. 39.

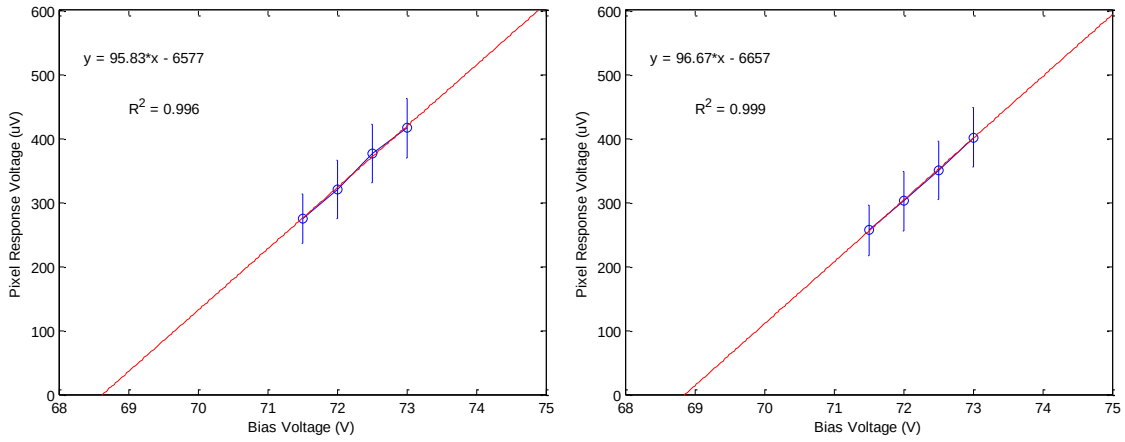

Fig. 39. The single pixel response amplitude of MPPC#1(left) and MPPC#2 (right) as a function bias voltage. The breakdown voltage determined by the x-intercept is 68.6 V and 68.9V, respectively. The error bars are the standard deviation of the measured single pixel response data.

The differences in breakdown voltage and very slight differences in pixel gains (i.e. slope of the line, which is related to the pixel capacitance) indicate that the response of these MPPCs can only be matched at a single operating bias voltage (i.e. the intersection of the two lines, if it exists). That operating bias voltage is an unreasonable 95.2 V for these two MPPC; consequently, the response can only be matched by using unique bias supplies. However, if the difference is within the tolerance of the application or can be corrected, then the MPPCs may be paired to a single bias supply without loss of functionality. For these experiments, the MPPCs were biased with a single supply for simplicity and to minimize interfaces with the dark box. Differences in the MPPC gains are accounted for in post processing corrections.

Additionally, by analyzing the area under the pulse height spectra, one can determine the probability of cross-talk as a function of bias voltage. The ratio of the area under the double pixel events to single-plus-double pixel dark count events gives the

probability of single pixel cross-talk, see [**4**]. The single pixel cross-talk data as a function of bias voltage is plotted in Fig. 40.

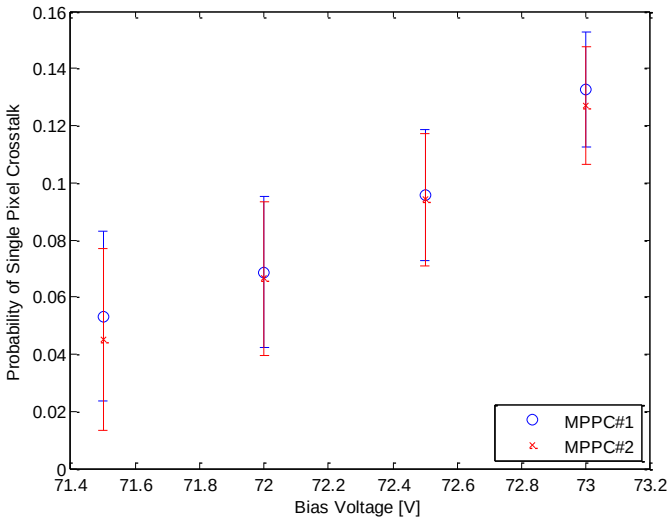

Fig. 40. Single pixel cross-talk probabilities are plotted versus bias voltage for both MPPCs. The error bars give the uncertainty due to counting statistics.

If precise crosstalk probabilities are essential for the application at hand, the error bars in Fig. 40 could be substantially reduced by increasing the number of counts (i.e. more measurement time since dark count rates are fixed at stable temperatures) shown in Fig. 32 and Fig. 38.

1. 2. MPPC Pixel Gains

By analyzing digitized dark count waveform data, several key operating parameters of each MPPC can be extracted. First, the pixel electron gain values can be extracted. By integrating the waveform over a short shaping time, the total charge released per pixel can be estimated by

$$Q = e \cdot M = \int_0^{\tau} I \, dt = \int_0^{\tau} \frac{V(t)}{R} dt \approx \frac{\tau}{N} \sum_{n=1}^{N} \frac{V[n]}{R}, \tag{4.1}$$

where Q is the estimate of the charge released during each pixel firing and is equal to the charge of an electron times the pixel gain, *M*. In (4.1), R is the load resistor over which the charge current, *I*, becomes the time dependent voltage waveform, $V(t)$, that is digitized over N samples throughout the integration time, τ, to become $V[n]$. Therefore, by averaging or simply summing the digitized waveform over a brief shaping time, a quantity directly proportional to the pixel gain is achieved, opening the possibility for regular self-calibration routines to be programmed into software controlling deployed SiPM devices. Similar calibration routines could be used to pair devices with similar pixel gains.

Using the measured breakdown voltages and nominal circuit parameter values from Wangerin, *et al*., a single pixel event was simulated using the expanded PSPICE model. The simulated single pixel waveform was compared to the measured single pixel waveform, the results can be found for MPPC#1 in Fig. 41.

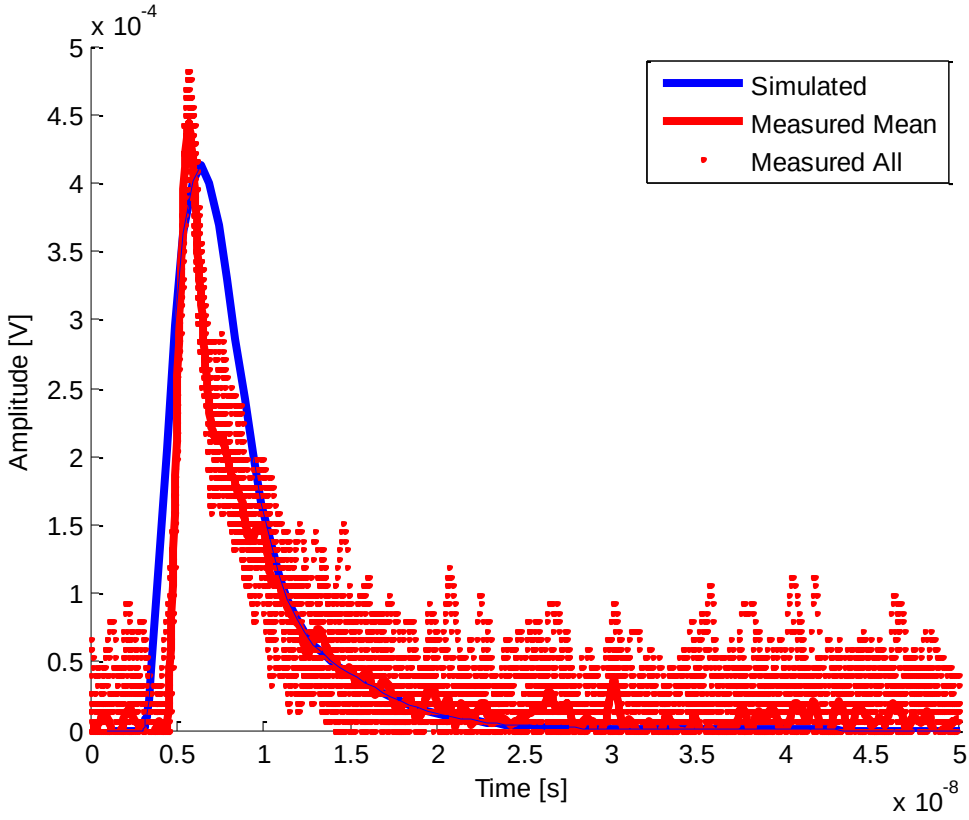

Fig. 41. The simulated waveform of a single pixel firing event is shown compared to the measured response of 25 of single pixel waveforms (and their mean) from MPPC#1 at 73 V bias.

Agreement between the simulated and measured data is quite good considering there is a degree of freedom in the components of the pixel capacitance (i.e. $C_{Pixel} = C_D + C_q$), which define the pixel discharge and recharge time constants. It is important to note that the pixel decay constant is measured to be approximately 5 ns (measured by the slope of the logarithm of the waveform); therefore, the pixels are generally fully recharged within about 20-25 ns. The resistor and capacitor values of each MPPC could be measured empirically (e.g. I-V curve measurements) then adjusted in the expanded circuit model to provide a better fit, but such effort would retract from the objective of this research.

Instead, this data is presented strictly to illustrate a reasonable understanding of the MPPC response.

According to (4.1), the average of the voltage waveform divided by the readout load resistance (i.e. 50 Ω) and multiplied by the integration time gives the charge. Doing so gives 39.5 fC for the simulated waveform and 40.5 fC and 34.2 fC for the mean measured waveforms for MPPC#1 and #2, respectively. The agreement is impressive considering the Wangerin model parameters (e.g. R_q and R_D) were not empirically measured. The pixel gains are computed to be $2.53\pm 0.50\times10^5$ and $2.15\pm 0.41\times10^5$, respectively, in good agreement with the advertised gain of 2.75×10^5 [**45**]. Finally, the pixel capacitance of the MPPC can be known by

$$C_{pixel} = \frac{Q}{\Delta V} = \frac{q \cdot M}{\left(V_{bias} - V_{breakdown}\right)}. \tag{4.2}$$

Applying (4.2) and using the measured charge values above and a bias voltage of 73 V give pixel capacitances of approximately 10 fF for both MPPCs. This pixel capacitance value is somewhat smaller than the 20-30 fF reported in [**42**] and [**44**].

A caveat is worth mentioning here. The pixel gain specified by Hamamatsu does not include a bias voltage but is assumed to be the operating voltage specified on each MPPC which is nominally 71.5 V per published specifications [**45**]. This bias is significantly less than the 73 V used in these measurements; therefore the pixel gain may be considered lower than expected. This lower than expected pixel gain corresponds to the lower than expected pixel capacitance and may suggest measurement bias. Since the load resistor was chosen to match the impedance of the coaxial cable and oscilloscope termination, the equivalent load resistance may have been less than 50 Ω resulting in a

lower measured current which would explain the lower measured values of pixel gain and capacitance.

1. 3. MPPC Response to Scintillation

Once the MPPCs were calibrated and their pixel response accurately simulated, the focus shifts to their application in scintillation detection. A widely studied scintillator, LYSO:Ce, was chosen because of its relatively high light yield and fast decay time. Consequently, LYSO:Ce has a high Birks' figure of merit value, $M_{LYSO} \approx 650$ ph ns^{-1} MeV^{-1}. The response of the LYSO:Ce crystal to gamma radiation from a ^{22}Na source was measured and simulated. Twenty five thousand scintillation pulse waveforms were digitized and collected using the oscilloscope with a rising edge trigger. One thousand of the largest amplitude waveforms were chosen to measure the decay time of the scintillator; jitter due to amplitude walk was thereby minimized. The largest measured scintillation pulses are shown individually in Fig. 42 and shown summed and normalized in Fig. 43.

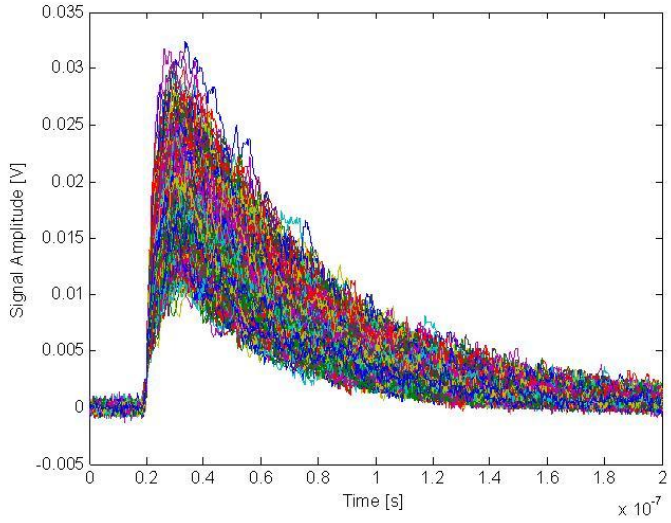

Fig. 42. MPPC response of LYSO:Ce scintillation pulses due ^{22}Na gamma irradiation is shown. The waveforms are measured directly from the MPPC readout without any amplification. Only the largest pulses were used to analyze the time decay of the scintillator to minimize jitter from amplitude walk.

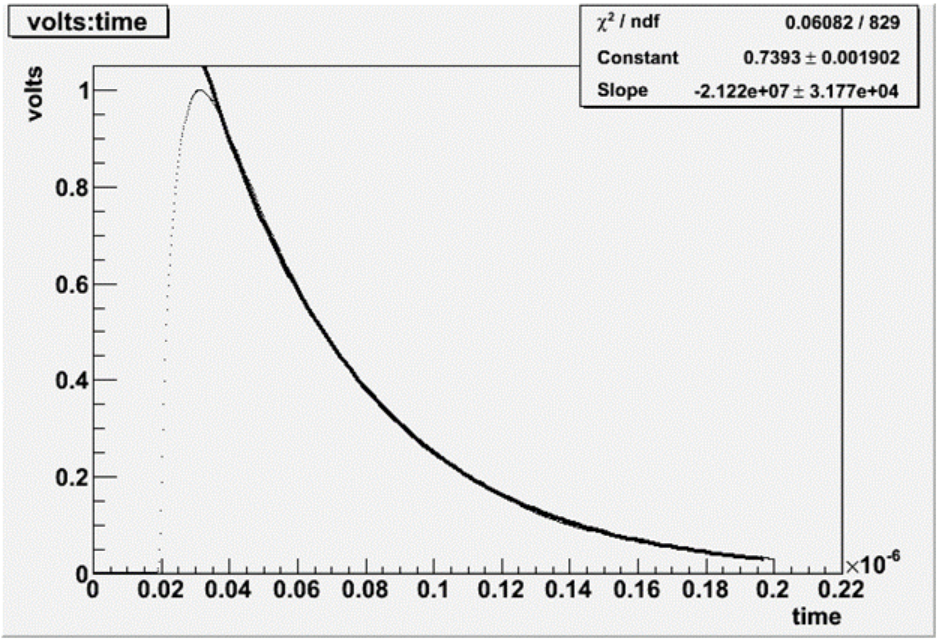

Fig. 43. LYSO:Ce scintillation decay curve as measured by the MPPC is shown normalized. The decay time constant is determined by the negative inverse of the slope of the exponential fit reported by ROOT [57], an open source C++ data analysis toolkit. A single exponential decay with a 47.1 ns time constant (black line) provides an excellent fit to the measured data (black dots).

The time domain response of the MPPC to LYSO:Ce scintillation light is in good agreement with values published in literature. ROOT, an open source and object-oriented data analysis toolkit [**57**], was used to provide the exponential fitting parameters; the decay time constant is the negative inverse of the "slope" reported by ROOT, 47.1±0.1 ns. Although 42 ns is generally accepted as the decay time for the LYSO:Ce, published values ranging between 40-50 ns are found in literature and industry [**58**] [**59**] [**60**]. Thus, the proper time domain response of the MPPC to LYSO:Ce scintillation is confirmed.

The signal amplitude is more challenging to confirm. The LYSO:Ce crystal is not calibrated and therefore has an unknown scintillation light yield. The repeatability of optical coupling of the small crystal to a calibrated PMT window is also a serious concern. Additionally, the optical quality of the author's attempt at surface polishing is somewhat suspect. As such, the signal amplitude was compared to simulated results from DETECT2000 for the correct order of magnitude response.

The LYSO:Ce scintillation waveforms were processed to generate a pulse height spectrum in terms of number of pixels firing, shown in Fig. 44.

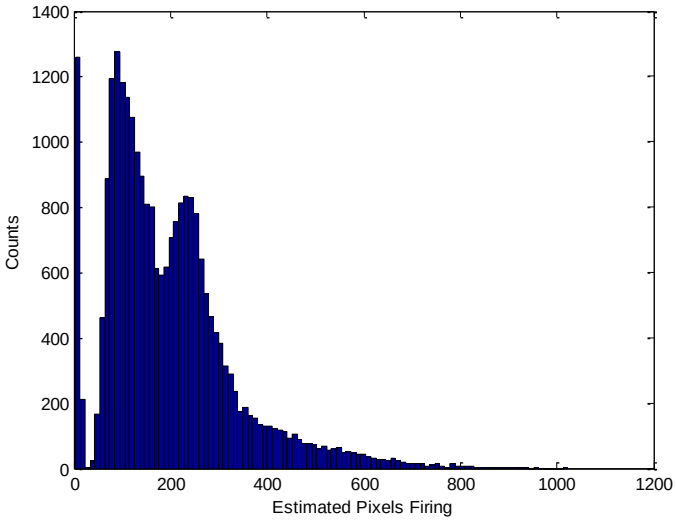

Fig. 44. MPPC pulse height spectrum of LYSO:Ce in response to ^{22}Na γ radiation in terms of approximate number of pixels firing. The 511 keV photopeak is centered near 240 pixels. The gap in the Compton continuum is due to the high threshold value set to discriminate dark counts. The events at the very left are due to dark counts or spurious trigger events.

Recall that the effective number of pixels using (2.29) yields approximately 10 times the number of physical pixels (i.e. 250 ns integrating time vs. 20-25 ns pixel recharge time). Therefore, the small number of pixels firing indicates that the device is operating in the linear region and correction of the spectrum for device saturation is not necessary. A rising edge trigger was used to discriminate dark counts and is responsible for the gap in the Compton continuum. However, occasional dark counts with cross-talk or spurious noise did breach the voltage threshold. Normally, such a threshold is set after integrating the signal, but this was not practical using the oscilloscope. Consequently, the gap in the continuum is larger than is typically seen in spectroscopy measurements and dark counts can be seen at the left of the spectrum. More sophisticated triggering systems will be required if directly digitized waveform data is to be used for MPPC signal readout and processing.

From Fig. 44, it can be seen that the energy resolution is quite poor (greater than 40%). This might be explained by the poor optical finish of the LYSO:Ce crystal or bad optical coupling to the MPPC. More likely, however, this energy resolution spread is due to electronic noise which could also explain the 30 channel spread from darkcounts at the left of the spectrum. Nevertheless, it is shown that the 511 keV photopeak from ^{22}Na positron annihilation corresponds to approximately 240 MPPC pixels firing. By simulating the experiment using DETECT2000, a mean value of 977 photons was detected using a 100% efficient detector. Assuming a photon detection efficiency of 25% (which corresponds to the MPPC PDE at 450 nm, the peak of LYSO:Ce emission), one should expect 244 MPPC pixels to fire from 977 scintillation photons.

While this appears to be reasonable agreement between measurement and simulation, it is important to bear in mind that the simulation results are drastically altered by user specified parameters, primarily the reflectivity coefficient of the simulated Teflon tape. For this simulation, a reflectivity coefficient of 0.95 was selected since it is the mean of the generally accepted values (0.92-0.98) found in published literature [**61**] [**62**] [**63**][**64**]. Changing this simulation parameter from 0.92 to 0.98 drastically alters the expected number of collected photons from 524 to 2559, respectively. Although other simulation parameters have drastic impact on collection efficiency, none are as significant as the surface treatment (assuming reasonability of the physical parameters; e.g. light yield, attenuation length, etc.). Of course, if this simulated phenomenon occurs in reality, this would be a substantial source of energy resolution smearing as well.

This caveat is mentioned not to discredit the agreement between the results of the measurements and simulations, rather to remind the reader that the purpose of these

measurements and simulations is to confirm the proper amplitude response of the MPPC to scintillation light. Using results from simulations throughout a range of reasonable parameters gives agreement to measured results to within, roughly, a factor of 2, thereby confirming the proper overall amplitude response (i.e. to well within an order of magnitude) of the MPPC to LYSO:Ce scintillation light.

As a final check, a simulated MPPC waveform was generated by convolving a time series of unit impulses (representing the arrival of scintillation photons) with the simulated single pixel response of the MPPC as described in Section III. 1. 4. The simulated 511 keV waveform is shown compared to a measured 511 keV waveform in Fig. 45. The simulated pulse is compared to the mean of 25,000 waveforms that fall under the photopeak in Fig. 46.

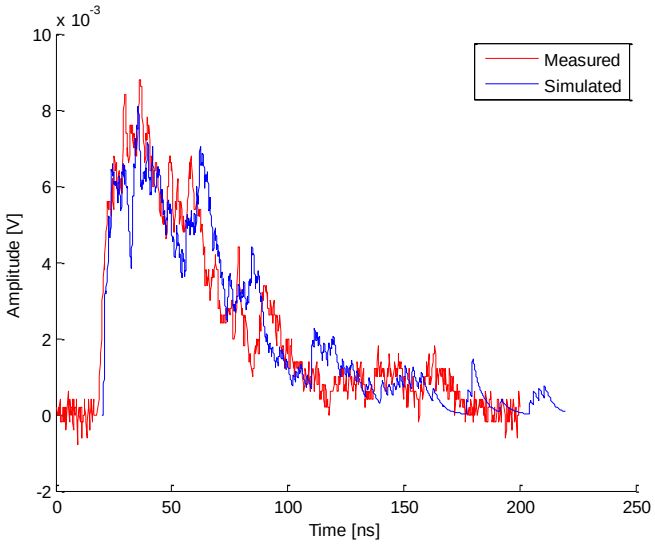

Fig. 45. A fully simulated 511 keV LYSO:Ce scintillation waveform is shown compared to a 511 keV LYSO:Ce scintillation waveform measured by an MPPC.

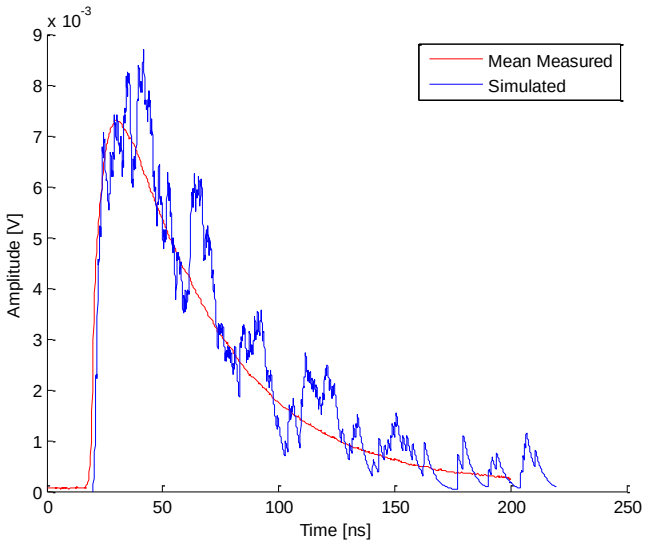

Fig. 46. A fully simulated 511 keV LYSO:Ce scintillation MPPC waveform is compared to the mean of 25,000 measured 511 keV scintillation MPPC waveforms.

2. YAG:Ce Fiber Findings

Once the MPPCs were calibrated and their response understood, they were used to measure the properties of the YAG:Ce fibers, namely the fluorescence decay time, attenuation length, and the energy and position resolution.

2. 1. YAG:Ce Scintillation Properties

An ^{241}Am alpha source was used to excite the YAG:Ce fibers, F1-F6 as described in Section III. 2. 1. The scintillation pulse shapes of 1600 events were recorded, summed together (i.e. filtering the MPPC signal), and normalized for each fiber, the results are shown in Fig. 47. The decay profile for each fiber was fit using a sum two exponentials for each fiber and the fit parameters are given in Table 3. The fit began at the peak of the scintillation pulse (nominally 10 ns) and concluded at 750 ns. The individual fiber decay profiles with fit curves can be found in Appendix A6. For comparison, recall from Table 1 that the fast component of YAG:Ce scintillation increased from ~105-115 ns

under gamma scintillation to around 68-89 ns under alpha scintillation, increasing with cerium activator concentration.

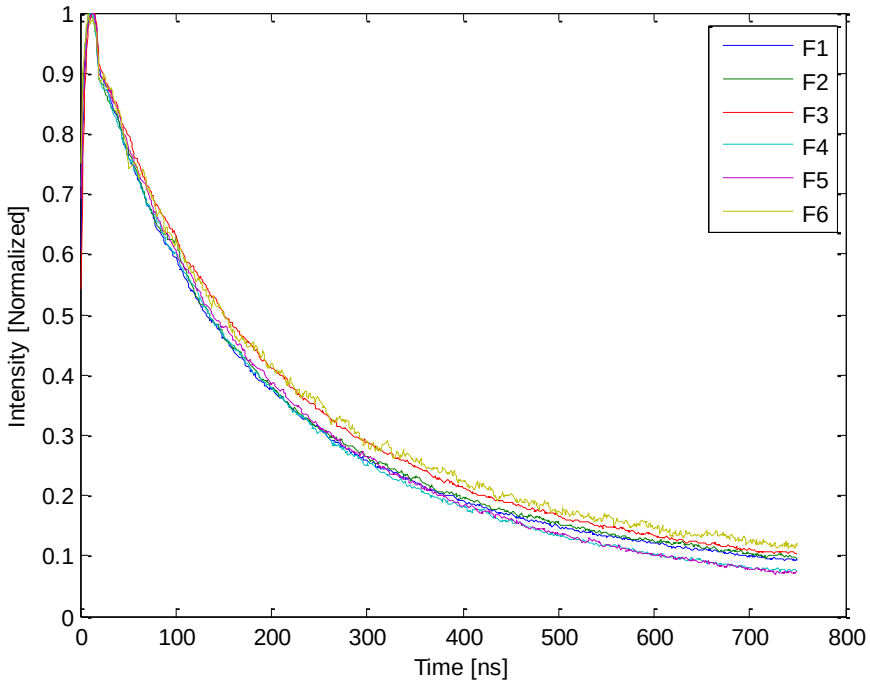

Fig. 47. The fluorescence decay profile measurements for six YAG:Ce fibers are shown after summing and normalizing over hundreds of scintillation pulses. The tails show slightly differing decay times.

Table 3. Alpha Particle Scintillation Decay Properties of YAG:Ce Fibers

Fiber	Fast Component		Total Intensity - Fast		Slow Component		Total Intensity - Slow	
[#]	[ns]	[± ns]	[%]	[± %]	[ns]	[± ns]	[%]	[± %]
1	115.27	1.13	28.39%	0.28%	519.75	7.12	71.61%	1.00%
2	125.08	1.43	30.77%	0.36%	588.93	12.28	69.23%	1.48%
3	139.61	1.63	31.77%	0.37%	587.20	12.45	68.23%	1.48%
4	126.33	1.71	31.85%	0.44%	436.68	7.53	68.15%	1.21%
5	113.69	1.89	24.65%	0.42%	373.27	4.77	75.35%	0.98%
6	122.52	2.41	24.45%	0.49%	562.75	14.66	75.55%	2.03%

As seen in Table 3, the fast components of YAG:Ce scintillation decay are in agreement with each other in terms of decay times and relative intensities. However, the

fast components are significantly longer than 68-89 ns scintillation decay of bulk YAG:Ce reported by Ludziejewski *et al.* in response to alpha radiation [**32**]. In fact, the fast decay component of the alpha scintillation more closely matches 105-115 ns decay associated with gamma scintillation as reported by Ludziejewski *et al.*, see Table 2. The slow decay components of the alpha scintillation reasonably compare to the slow components measured by Ludziejewski *et al.*. The trends of the relative intensities are also in agreement with the results reported by Moszynski *et al.*[**32**]. Of course, the materials studied by these groups can reasonably be assumed to be homogeneously doped with cerium activator. This is unlikely the case for the single crystal fibers grown via μ-PD, as shown in [**21**], [**28**], and [**40**].

In addition to alpha excitation, F6 was irradiated with gamma rays from a ^{22}Na source. The fluorescence decay time profile of gamma scintillation is shown compared to alpha scintillation in Fig. 48.

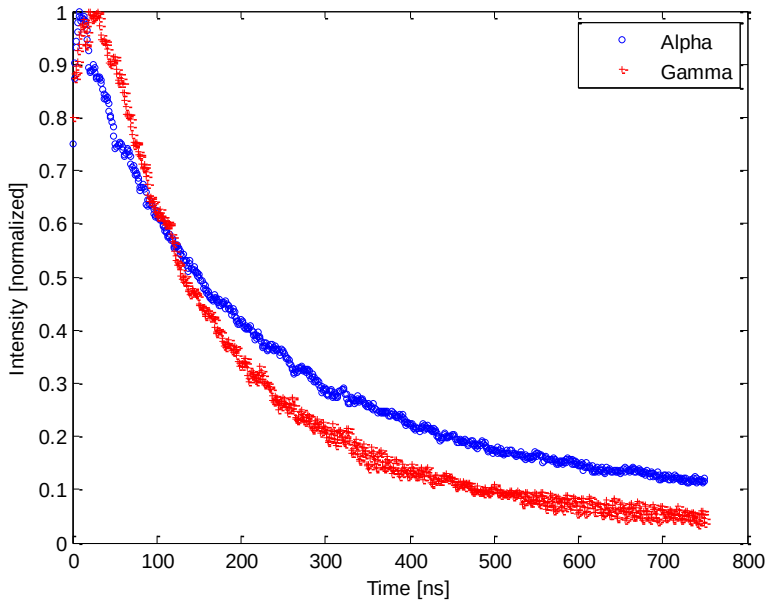

Fig. 48. The fluorescence time decay profile of YAG:Ce fiber F6 under gamma excitation is shown compared to alpha excitation. Interestingly, the fast and slow decay constants are nearly identical for both gamma and alpha excitation, but the intensities flip.

The fast and slow decay components of F6 in response to gamma scintillation are 128.1 ±2.4 ns and 561.8 ±56.8 ns with respective intensities of 56.6 ±1.1% and 43.4 ±4.8%. Interestingly, the decay time constants are nearly identical to the fiber's alpha scintillation response. Thus, the decay time constant change between alpha and gamma scintillation in bulk YAG:Ce observed by Moszynski *et al.* is not apparent in this fiber shaped sample. However, Moszynski *et al.* report that a slow transfer of energy from lattice-to-activator under gamma excitation results in a slow rise time which can be seen in the data from F6. Zych, *et al.*, attribute this to the presence of Y_{Al} anti-site defects and the subsequent intrinsic luminescence which is strongly absorbed by activator sites [**20**]. Additionally, the change in decay intensities between YAG:Ce alpha and

gamma scintillation has been reported by Moszynski *et al.*, however the relative change is dependent on Ce concentration, see Table 2 [**30**].

The change in scintillation decay times between gamma and alpha reported by Moszynski *et al.* is attributed to the presence of shallow traps, as shown by Zych *et al*, and is also dependent on the amount of Ce activator [**20**]. Under alpha excitation, Ce activator sites quickly saturate resulting in the population of thermal traps which release charge slowly (e.g. tens to hundreds of ns) and can de-excite non-radiatively. This mechanism is responsible for the low α/γ ratio, the short fast component, and long slow component which causes the long tail on the alpha scintillation pulse. The fast primary and secondary electrons associated with gamma interaction in the YAG:Ce, transfer their energy (via ionization) to the lattice over a greater range and over a longer time period than alphas. In the presence of anti-site defects, de-excitation readily occurs via extrinsic luminescence which is absorbed by Ce activator sites, according to Zych, *et al.* [**20**]. The result is a slower rise time, but more efficient transfer of energy to the Ce activator sites. The longer than expected fast decay component for alpha scintillation suggests saturation of Ce activator sites. Perhaps, higher concentration of Y_{Al} anti-site defects, which could be a result of the rapid growth rates via μ-PD or of the after heater annealing process, cause the slower-than-expected fast decay component. Without further experimentation, such explanations remain mere conjectures. To test this hypothesis, one could identify the Y_{Al} anti-site defect photoluminescence peak in bulk YAG:Ce and compare its relative intensity to that measured in YAG:Ce fibers. Additionally, positron annihilation lifetime spectroscopy comparisons between sintered ceramic YAG:Ce films, bulk single crystal YAG:Ce, and fiber single crystal YAG:Ce might test this hypothesis. Since YAG:Ce

ceramics have been shown to be free of Y_{Al} anti-site defects in [**65**], the lifetime of a positron in the YAG:Ce might be used to compare the relative abundance of Y_{Al} anti-site defects in YAG:Ce fibers to those found in bulk YAG:Ce (see [**33**]).

A very fast initial decay component (~6 ns decay constant) can be observed immediately after reaching the peak (~10-15 ns) in Fig. 47 which may indicate the presence of the similarly fast (16 ns) Ce luminescence decay observed in fine grain ceramic YAG:Ce scintillators as reported by Zych, et al [**66**]. However, its intensity was too low relative to the entire pulse to accurately measure using the fitting functions. The Ce concentration, according to Fibercryst, is between 0.05-0.10% mol. [**38**]. Compared to the crystals used in the experiments by Ludziejewski *et al.,* these activator concentrations are relatively low (0.1 at. %. compared to 1.08 at. % reported in [**32**]) and saturation might explain the slower decay times. Refer to Table 1 for the decay time data reported for various cerium concentrations of YAG:Ce.

As with the earlier LYSO:Ce scintillation experiment, the readout of alpha scintillation waveforms from the YAG:Ce fibers using MPPCs was simulated in DETECT2000, using parameters from Moszynski *et al.*. The fully simulated 5.4 MeV alpha scintillation MPPC waveform is shown compared to a measured alpha scintillation waveform in Fig. 49. The same simulated pulse is shown compared to the mean of 8,000 digitized 5.4 MeV alpha scintillation waveforms in Fig. 50.

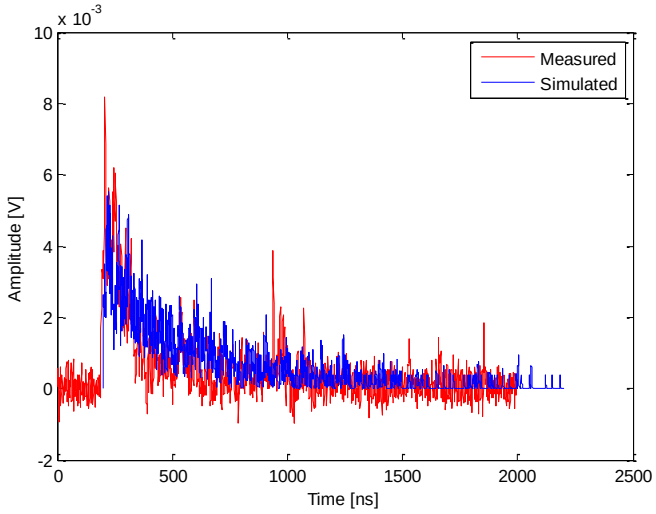

Fig. 49. A fully simulated 5.4 MeV alpha scintillation waveform in a YAG:Ce fiber as readout using an MPPC is compared to a measured event waveform.

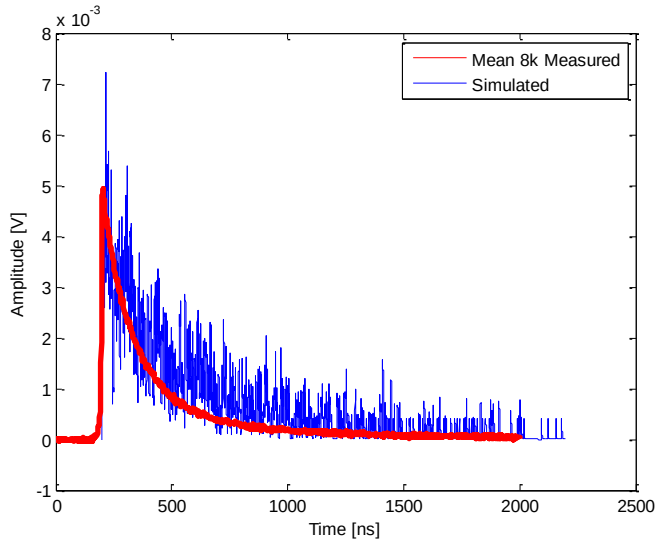

Fig. 50. A fully simulated 5.4 MeV alpha scintillation waveform in a YAG:Ce fiber as readout using an MPPC is compared to the mean of 8,000 measured waveforms.

The overall signal amplitude of the measured alpha scintillation waveforms are in good agreement with the results of the simulation. In general, fewer pixels fired in measurement than in simulation which may indicate a lower than expected scintillation

yield. This could be explained by particle straggling, or perhaps by a lower concentration of Ce activators which is supported by the longer than expected scintillation decay times.

2. 2. YAG:Ce Energy Spectrum and Resolution Results

Attempts to measure the achievable energy resolution using YAG:Ce fibers with fiber end MPPC readout, as described in Section III. 2. 2. were unsuccessful due to the lack of a measureable photopeak using gamma sources. Spectra were collected using traditional NIM spectroscopy electronics (e.g. charge integrating preamplifier, shaping amplifier, and multi-channel analyzer). A typical measured spectrum is shown in Fig. 51, taken under gamma irradiation from a ^{22}Na source.

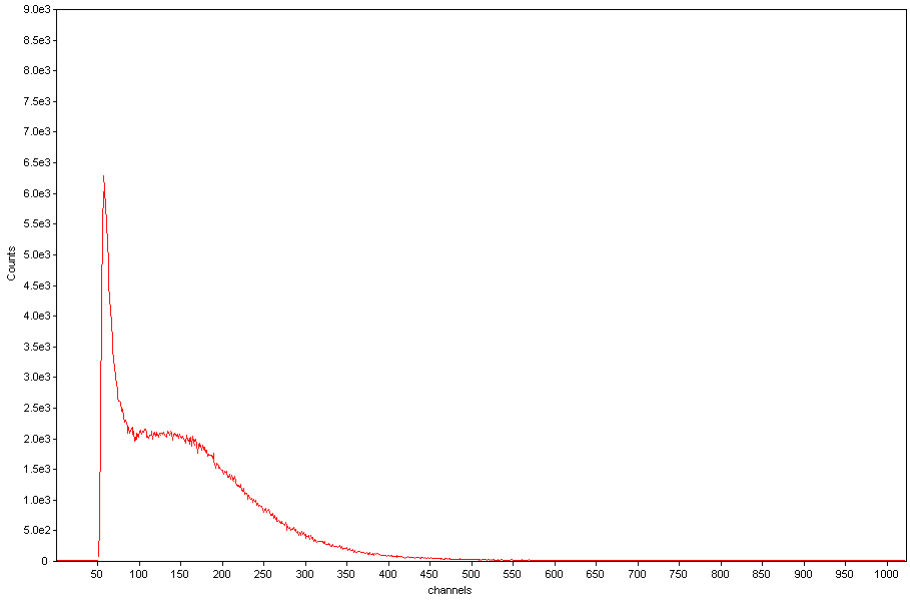

Fig. 51. ^{22}Na gamma energy spectrum using MPPC readout, NIM spectroscopy electronics, and a YAG:Ce scintillating fiber. Noise integration can be seen near Channel 75 indicating very noisy electronics. A feature resembling a Compton edge appears around Channel 200.

Extremely low gamma efficiencies should be expected from such thin scintillating crystals, especially those with low stopping power such as YAG:Ce. Consequently,

alpha spectroscopy is better suited. An alpha spectrum from a ^{241}Am source taken using the same fiber and electronic settings is shown in Fig. 52.

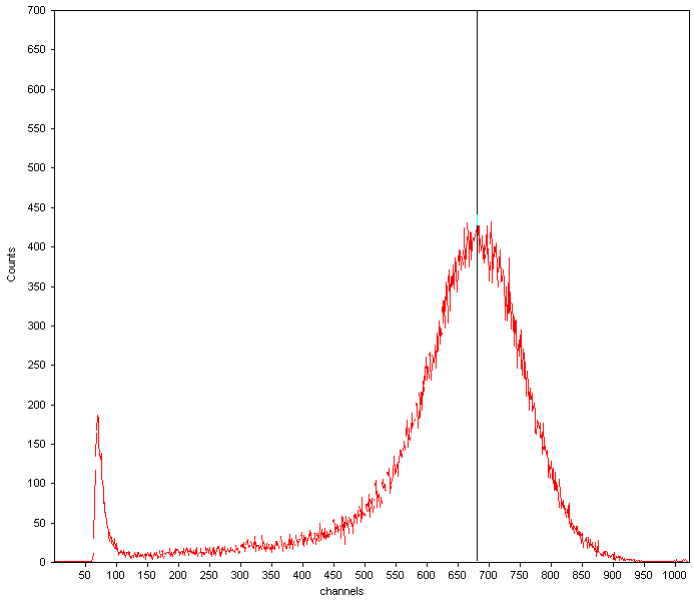

Fig. 52. ^{241}Am alpha spectrum shown using the same readout and settings as the ^{22}Na spectrum in Fig. 51. Noise integration can be seen around Channel 75 indicating very noisy electronics. The alpha peak appears around Channel #667.

As a side discussion, the electronic noise from this system is a serious concern. Noise that was integrated via the preamplifier, shaped, and then digitized can be seen as high as Channel 100 from the ADC pulse height spectrum. A better engineering MPPC front end readout to include better shielding and grounding will be essential to improve the noise performance of this detector system.

The Compton edge of a 511 keV gamma ray lies at 340 keV. If one accepts that the Compton edge lies near Channel #200 of Fig. 51 and assumes an α/γ ratio of 21% in YAG:Ce, then the peak of the 5.4 MeV alpha associated with ^{241}Am should be expected at Channel #667, which agrees with the data in Fig. 52. These results are no substitute

for a proper energy calibration, to say the least; rather, they merely serve as sanity check to the system response.

The results of the alpha spectroscopy experiment are somewhat reasonable. The spectrum shown in Fig. 52 appears to be a typical alpha spectrum; there is a well defined (albeit broad due to electronic noise) peak with a low energy tail which represents the counts of particles which lost energy (i.e. straggling) along their tracks to the detector. However, the gamma energy spectrum is lacking distinguishing features making it difficult to calibrate and impossible to determine energy resolution. To explain the lack of features, the experiment was simulated using a popular particle tracking code called Monte Carlo N-Particle transport code, version 5 (MCNP5) [**67**]. The simulated energy spectra of a pure YAG fiber from several monoenergetic gamma ray beams at two angles of incidence are shown in Fig. 53.

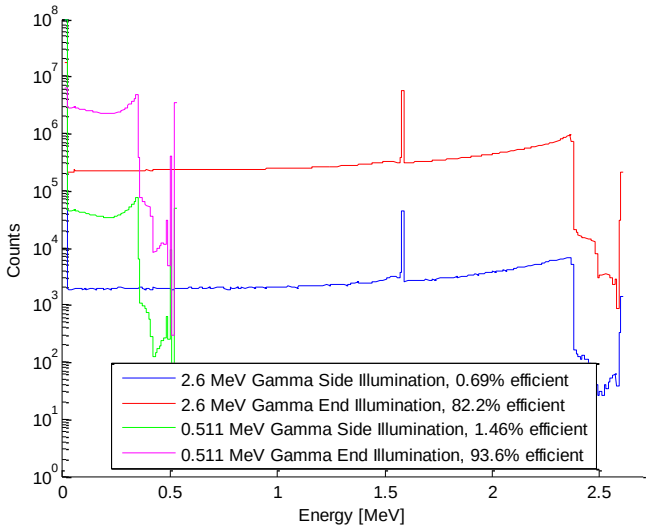

Fig. 53. The gamma energy spectra of a YAG fiber simulated using MCNP5 are shown for beams of monoenergetic 511 keV and 2.6 MeV gamma rays at two angles of incidence. Side illumination means the beam was incident orthogonal to the fiber axis. End illumination means the beam incidence was along the fiber axis. The reported efficiencies are the total number of interactions out of the 100 million incident gamma particles.

It is clear from Fig. 53 that the YAG:Ce fibers are inherently inefficient by themselves and have extremely low photofractions (i.e. the ratio of the area under the photopeak to the entire response function). The 511 keV photofraction is about 3.5% while the 2.6 MeV photofraction is a dismal 0.2%. The spectrum measured in the lab had much fewer overall counts and it is therefore unreasonable to expect a distinct photopeak. Also, the position resolution measurements required side illumination (i.e. orthogonal to the axis) of the fiber. The results from MCNP5 simulations clearly indicate that the fibers are more efficient when illuminated from the end (i.e. along the fiber axis). This increase in efficiency may provide directionality or background reduction for future imaging applications. In addition to inefficiency, another explanation for the lack of well defined features in the measured gamma spectrum is offered here.

Recall that the Ce concentration of YAG:Ce grown via μ-PD has a strong radial dispersion. In fact, the fiber may be more closely modeled as a shell of highly doped YAG:Ce with a lightly doped core rather than a homogeneous material. As a result, when the Compton recoil electrons or photoelectrons deposit their energy along relatively long tracks, they excite charge carriers in both regions of high and low Ce concentration within the fiber crystal. Since the scintillation efficiency of the fiber crystal is dependent on the activator concentration, the total amount of light produced during scintillation is dependent on the location of interaction and the subsequent localized densities of charge carriers within the fiber. In other words, the already poorly defined high energy features (due to the inefficiency of the small detector volume) may be smeared due to the fluctuations in scintillation light yield which result from varying concentrations of activator sites.

Although the absolute quantities of cerium activator could not be measured in the fibers via X-ray fluorescence microscopy or SEM due to low atomic concentrations (i.e. 0.1 at.% [**38**]), clear radial dispersion of the cerium can be observed via UV fluorescence microscopy. A 100 μm thick cross-sectional slice of YAG:Ce fiber was cut by technicians at the Air Force Research Laboratory Materials and Manufacturing Directorate. The slice was then photographed under a UV microscope. As shown in Fig. 54, there is clearly a radial dispersion of the activator as indicated by the increase in luminous intensity near the fiber rim.

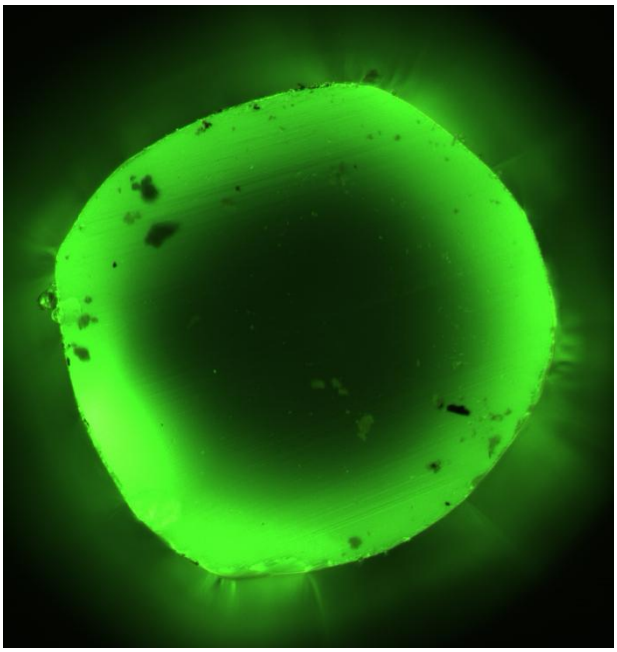

Fig. 54. An image of a 100 µm thick cross-sectional slice of YAG:Ce fiber taken using a UV microscope is shown. The radial dispersion of the cerium activator is evident by the increase in luminous intensity at the rim of the fiber. The dark spots are most likely carbon deposits from the diamond saw blade used to cut the fiber.

The intensity of the green channel was plotted for three vectors across the fiber, as shown in Fig. 55. However, the camera's 8-bit ADC was saturated by the intense luminescence at even the lowest UV illumination setting; this can be seen by the plateau at values of 255 in Fig. 55.

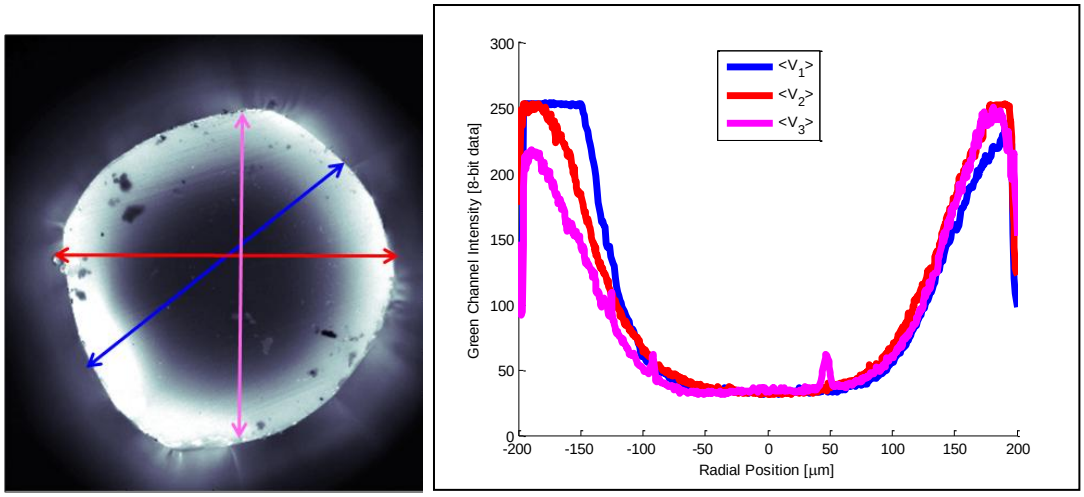

Fig. 55. The green channel from an image of a YAG:Ce fiber cross-section under UV fluorescence is shown on the left. On the right, the channel intensity is shown as a function of radial position for the three different diameter vectors shown in blue, red, and magenta. Notice that the CCD's 8-bit ADC is saturated even at the lowest UV illumination setting.

Although this data does not indicate the cerium concentration directly, one might assume a linear relationship between the concentration and light yield, as shown for LuAG:Ce by Dujardin, *et al.*, in [**40**]. If the average radial intensity is normalized to the nominal cerium concentration value of 0.1 at.%, Fig. 55 can be transformed, albeit crudely, from intensity to cerium concentration. The cross-sectional fiber slice is obviously not thin enough to neglect the transport of fluorescence photons within the material; thus, this approach is a rudimentary oversimplification at best. Nevertheless the shape of the transformation is insightful and, as shown in Fig. 56, agrees rather nicely with the calibrated data presented by Dujardin, *et al.*, for a 2 mm diameter LuAG:Ce fiber. Compare, specifically, the shape of the profile in the outer 100 μm of the fiber diameter.

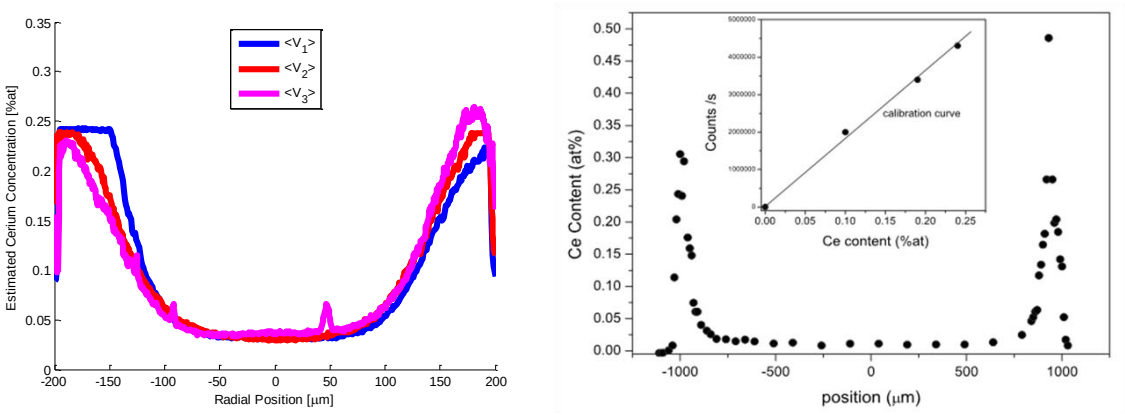

Fig. 56. Intensity data from YAG:Ce fluorescence has been linearly transformed and normalized (to 0.1 at.%) to indicate relative cerium activator concentration (left). The spike at 50 μm in magenta is from a deposit of material, see Fig. 55. The data is comparable to that shown by Dujardin, *et al.*, in [40] for 0.1 at.% cerium doped LuAG:Ce (right).

The cerium concentration results presented and discussed above invite a variety of additional experiments for cerium activated and fiber shaped crystals grown via μ-PD of various diameters. Many questions come to mind. Is the activator dispersion a function of the ratio between fiber volume and surface area? Is there a limit to this dispersion if fibers are grown thin enough? Can fibers be more heavily doped, then chemically etched to remove the highly doped outer shell while also removing optical defects on the fiber surface?

Of course, the present situation leaves open the possibility of energy resolution degradation due to light yield smearing as secondary electrons deposit energy along their tracks within the scintillator. The following discussion presents evidence showing that the track lengths of fast Compton recoil electrons in YAG:Ce are sufficiently long that this possibility of scintillation light yield smearing cannot be overruled.

To determine the track length of electrons in YAG:Ce, one can use the stopping power and range equations, (2.22) and (2.23). Additionally, the stochastic nature of light particle interactions is well suited for Monte Carlo simulations. CASINO (v2.42) [**68**], a Monte Carlo software program designed to track electron interaction in user defined materials, was used to simulate the trajectories of Compton recoil electrons in YAG:Ce. Specifically, beams of 340 keV and 2.36 MeV electrons (corresponding to the Compton edges of a 511 keV and 2.6 MeV gamma ray, respectively) were simulated using CASINO to track trajectories in a bulk YAG:Ce using the Joy and Luo models for low energy electron scattering with cross-section values determined by the Mott and Massey interpolation [**69**]. The CASINO electron trajectories as well as the penetration distance and energy distributions are shown in Fig. 57 through Fig. 60 for both 340 keV and 2.36 MeV electrons. The results are compared to the electron range in YAG:Ce calculated using the Bethe-Bloch formula, see Fig. 15.

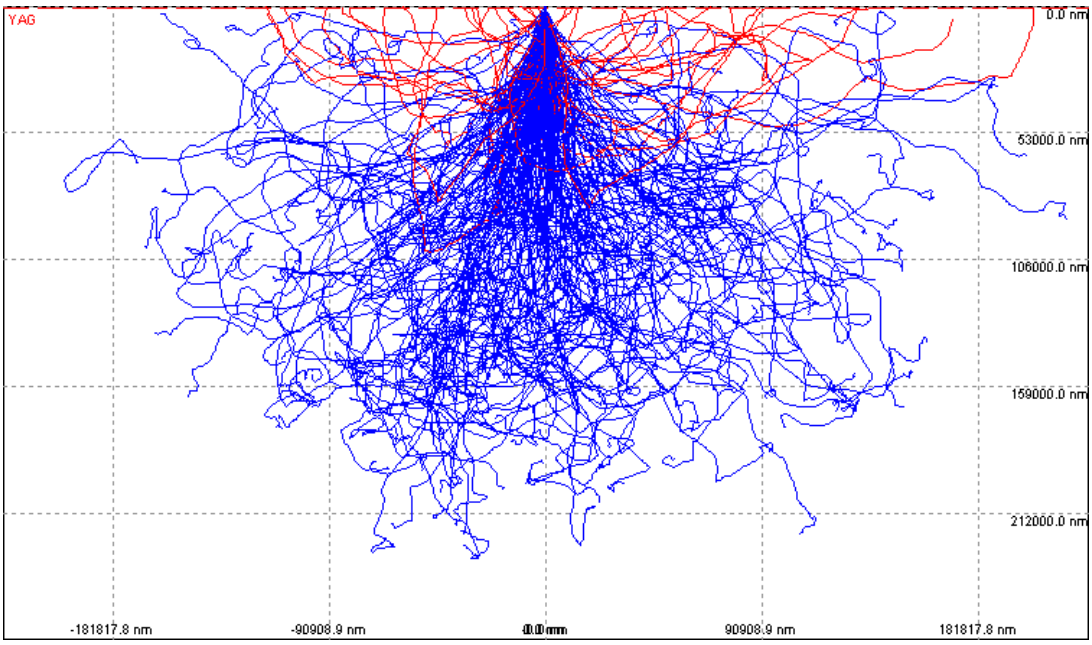

Fig. 57. Electron trajectory results from CASINO v2.42 simulations of 1000, 340 keV electrons in bulk YAG:Ce are shown. Red tracks are events which backscatter and eventually escape the sample, while blue tracks show full energy deposition events. The results agree nicely with 100-200 µm range for 340 keV electrons in YAG:Ce calculated using the Bethe-Bloch formula and presented in Fig. 15.

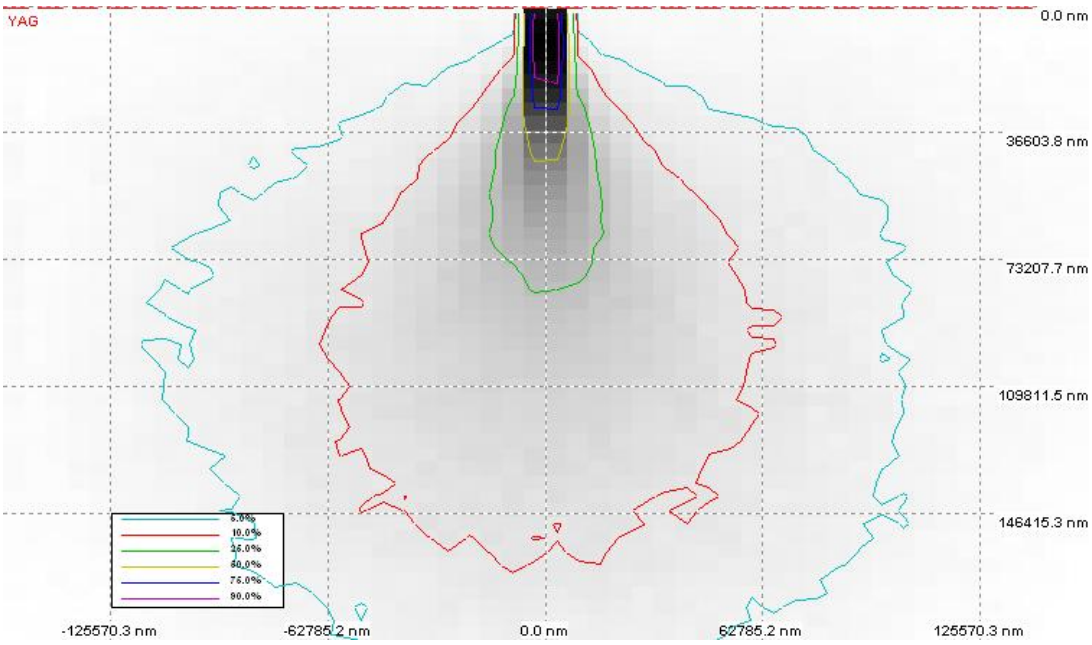

Fig. 58. Energy deposition distribution from CASINO v2.42 simulations of 340 keV electrons in bulk YAG:Ce is shown.

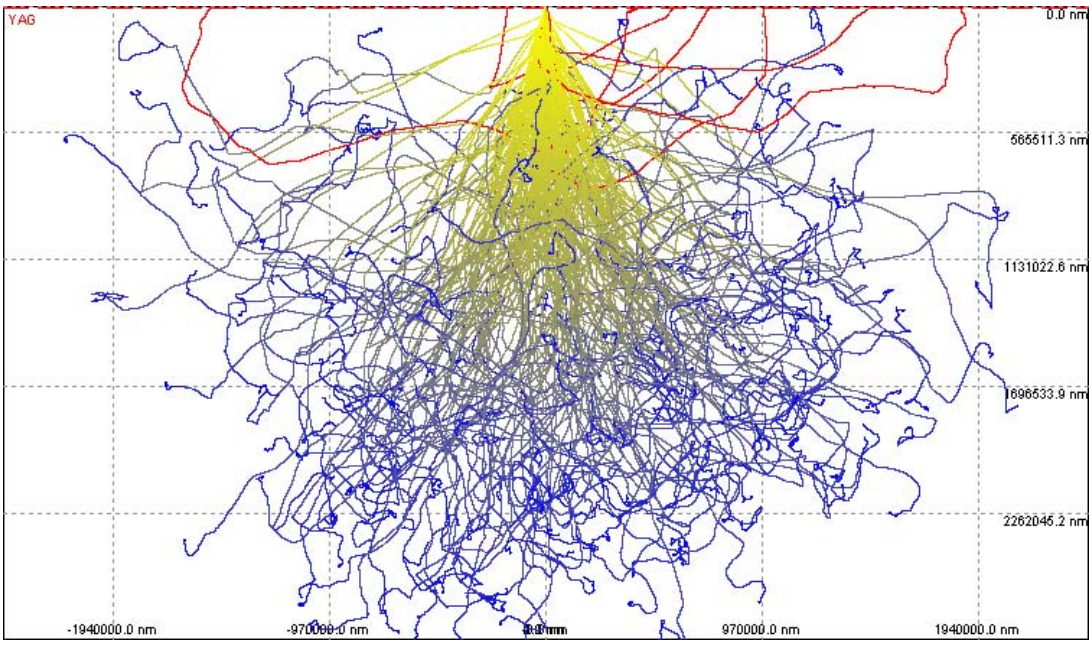

Fig. 59. Electron trajectory results from CASINO v2.42 simulations of 1000, 2360 keV electrons in bulk YAG:Ce are shown. Red tracks are events which backscatter and eventually escape the sample, while yellow (high energy electron) and blue (down scattered, low energy electron) tracks show full energy deposition events. The results agree nicely with the ~1-2 mm range for 2360 keV electrons in YAG:Ce calculated using the Bethe-Bloch formula and presented in Fig. 15.

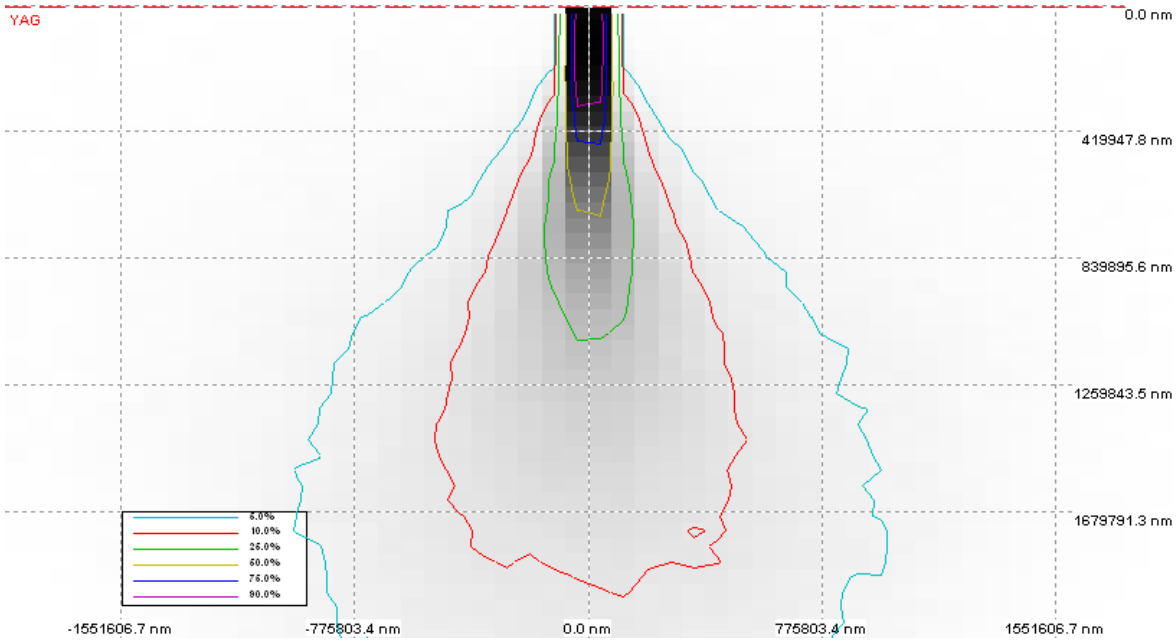

Fig. 60. Energy deposition distribution from CASINO v2.42 simulations of 2360 keV electrons in bulk YAG:Ce is shown.

According to the Bethe-Bloch calculations in Fig. 15, the range of a 340 keV electron in YAG:Ce is between 100-200 μm which agrees with the CASINO simulations shown in Fig. 57 through Fig. 58. According to Fig. 58, CASINO simulations indicate that a 340 keV Compton recoil electron which penetrates further than 100 μm can retain more than 10% of its energy. Even more interesting, however, are the results in Fig. 59 and Fig. 60 which simulate a 2360 keV Compton recoil electron from a 2.6 MeV gamma interaction. CASINO simulations indicate that the 2360 keV electron ranges are in exceess of 1 mm in YAG:Ce, which is also in good agreement with the Bethe-Bloch calculations. According to Fig. 60, the 2360 keV Compton recoil electrons retain as much as 75% of their energy after 400 μm and 50% of their energy after 1 mm. Since Compton scattering dominates the gamma ray interactions in this energy regime (200 keV -3 MeV), these simulated and computed electron ranges in excess of 100 μm can be reasonably expected from gamma ray interactions in YAG:Ce.

The takeaway from this discussion is that the penetration range of even low energy Compton recoil electrons is a sizeable portion of the 400 μm YAG:Ce fiber diameter. Higher energy recoil electrons may altogether escape the YAG:Ce fibers, depositing only a fraction of their energy in the scintillator. Although these results do not indisputably confirm the presence of scintillation light yield smearing as the charge carriers interact in regions of differing Ce concentrations, it certainly does not rule out the possibility either. Likewise, these simulations indicate that tracking Compton recoil electrons in neighboring inorganic scintillating fibers is not only possible, but may be necessary in order to ensure accurate calorimetry using YAG:Ce scintillating fiber of diameters even as large as 1 mm.

2. 3. YAG:Ce Fiber Photoluminescence Position Resolution Results

The achievable position resolution in a YAG:Ce fiber was measured using both photoluminescence from a 405 nm laser and alpha scintillation from an ^{241}Am source. This section is reserved for the results of the photoluminescence experiments described in Section III. 2. 3. Although the charge carrier kinetics associated with non-ionizing photoluminescence are different than those associated with ionizing radiation, the emission spectrum is the same due to the 5d-4f transitions of the Ce activator. Therefore, the photoluminescence experiments provide controlled conditions to measure the attenuation length of the YAG:Ce fibers to compare to scintillation based measurements.

By integrating the charge released by dual fiber end MPPC readouts and controlling the position-of-interaction, the attenuation length of the fiber can be estimated by inverting (2.13). The attenuation length, λ, can be estimated from the slope of a linear-least-squares fit of the plot of $\log\left(\overline{N}_2 / \overline{N}_1\right)$ as a function of the interaction position. That is, the attenuation length is by definition

$$\begin{aligned} \log\left(\frac{\overline{N}_2(x)}{\overline{N}_1(x)}\right) &\equiv -\frac{l-x}{\lambda} - \frac{-x}{\lambda} \\ \log\left(\frac{\overline{N}_2(x)}{\overline{N}_1(x)}\right) &= \frac{2}{\lambda}x - \frac{l}{\lambda} \quad , \\ y(x) &= mx + b \\ \lambda &= \frac{2}{10 \cdot m}[\text{cm}] \end{aligned} \tag{4.3}$$

where m is the slope from a linear-least-squares fit of $\log\left(\overline{N}_2 / \overline{N}_1\right)$ as a function of x, the position-of-interaction, and the factor of 10 simply converts between units of millimeters (i.e. x is measured in mm) and centimeters which are conventionally used to

describe attenuation length. By repeatedly mounting the fiber and making independent measurements of λ, one can gain confidence in the accuracy of the measurement as well as assess the repeatability of the optical coupling. The slope of the linear-least-squares fit is reported as the fiber's attenuation length for all five fibers for each repitition. To quantitatively assess the quality of the linear-least-squares fit, the coefficient of determination, R^2, is computed and indicates the linearity (i.e. the quality) of the fit. If the R^2 is less than or equal to 0.95 for any trial, that λ measurement is rejected.

In order to estimate the uncertainty in the $\log\left(\overline{N}_2 / \overline{N}_1\right)$ using the error propagation formula, (2.15), one must first show normality of $\log\langle N_i \rangle$ with mean $\log\left(\overline{N}_i\right)$ and sample variance $\sigma^2_{\log\langle N_i \rangle}$ where $\langle N_i \rangle$ is the set of photon counts at the i^{th} MPPC. It is important to note that there is no theoretical justification for true normality in the distribution of these logarithmic ratios (i.e. one might expect log-normality if N_i is large). It is convenient, however, to apply such an assumption of normality when calculating an *estimate* of the uncertainty, if such an assumption can be justified.

To justify the assumption of normality, a Kolmogorov-Smirnov goodness-of-fit test (KS-Test) was applied to the logarithmic data sets, $\log\langle N_i \rangle$, at each illumination position to test for normality. Without exception, the null hypothesis of the KS-Test (i.e. that the data are normally distributed) was accepted with a 95% confidence interval for every photoluminescence data set. As a result, the error bars on the plots of $\log\left(\overline{N}_2 / \overline{N}_1\right)$ are reported as

$$\sigma_{\log\frac{\overline{N}_2}{\overline{N}_1}} = \sqrt{\sigma^2_{\log\langle N_1\rangle} + \sigma^2_{\log\langle N_2\rangle}} \tag{4.4}$$

where $\sigma^2_{\log\langle N_i\rangle}$ is the sample variance of the set $\log\langle N_i\rangle$ at each position, for every fiber and repitition.

Before presenting the results, one final point must be discussed. First, notice the outlying data set on the attenuation length plot for F1 shown in Fig. 61.

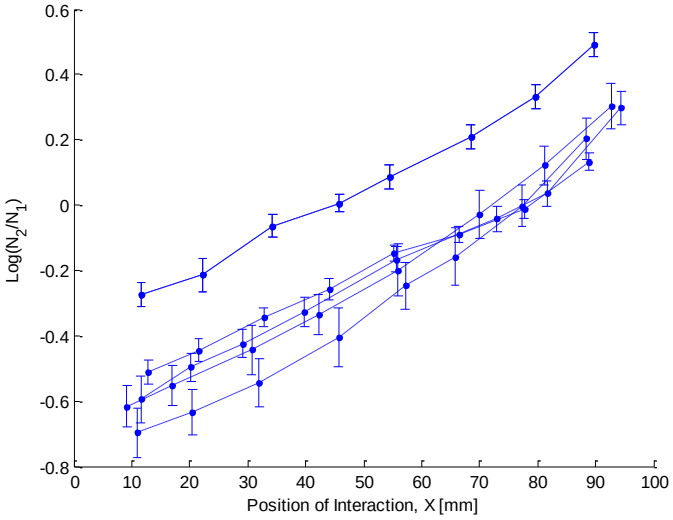

Fig. 61. The attenuation length of F1 can be determined by the slope of the line of $\log\left(\overline{N}_2 / \overline{N}_1\right)$ vs. interaction position. The measurements were repeated five times for each fiber. The slope of the lines should be the same for a given attenuation length. Repeatability of optical coupling is measured by the y-intercept. The error bars are computed by (4.4).

By symmetry, one should expect that the ratio of light intensity be equal to unity at the mid-point in the fiber (log[1]=0). This corresponds to the y-axis intercept on the plot. Notice that in Fig. 61 only one line intercepts the y=0 at the 50 mm fiber mid-point. The reason for this is because during the second attempt at mounting the fiber crystal, the acrylic window of MPPC#2 was accidently damaged by over-tightening the vice mount.

Rather than rebuild another MPPC readout circuit and test and calibrate it, the experiments were continued with the damaged MPPC#2 under the assumption that valid conclusions can still be drawn from relative measurements. As such, the damaged MPPC#2 can be thought of as a less efficient detector or a signal path with more loss. No further damage was done to the device by continuing to use it. The damage done to MPPC#2 can be seen in Fig. 62.

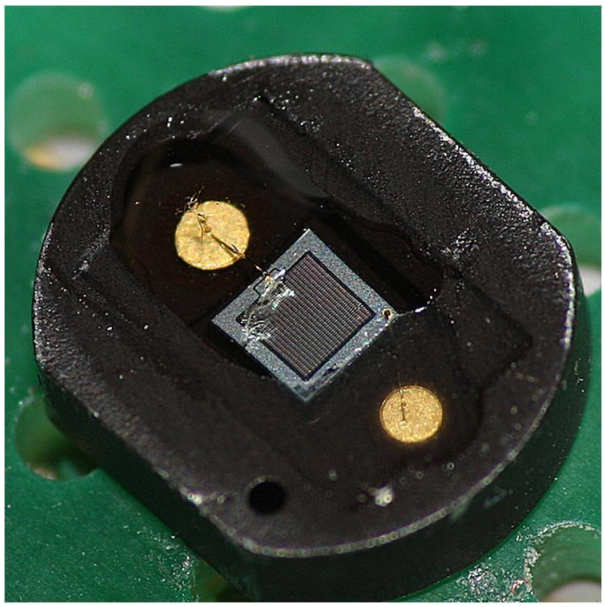

Fig. 62. Damage done to the acrylic window of MPPC#2 by over-tightening in the vice mount is shown. Extreme caution should be applied when handling the photosensitive surfaces of the MPPCs. The acrylic is soft and easily cracks and scratches; it is not intended for pressure coupling with extremely hard surfaces such as thin garnet crystals.

Despite this incident, the results of the attenuation length measurements for F1 are reasonable. The slopes are repeatable; however, the repeatability of the optical coupling is somewhat questionable. Ignoring the outlier prior to MPPC#2 damage, the data shown in Fig. 61 indicates a spread in y-offset by as much as 0.2, which corresponds to a factor of $\exp(0.2) = 1.22$ in optical coupling repeatability. The quality of the optical coupling

is paramount to successful spectroscopy measurements; therefore, the optical coupling of these thin fibers to MPPCs is an area with room for improvement.

The discussion now returns to the experimental results. Once estimated, the attenuation length is then applied to the inverse problem to determine the achievable position resolution of the YAG:Ce fiber under laser excitation. The achievable position resolution is defined by the sample standard deviation of the position estimate distribution. The position resolution is, equivalently, the error bars of the position-of-interaction plots shown in Fig. 63 through Fig. 68.

The position-of-interaction plots also report a goodness-of-fit descriptive statistic, χ^2, defined as

$$\chi^2 = \sum \frac{\left(x - x\right)^2}{\sigma_x^2}, \tag{4.5}$$

where x is the position estimate given by (2.13), x is the true position-of-interaction, and σ_x^2 is the sample variance of the distribution of x or, equivalently, the position resolution squared. The χ^2 is averaged across all repititions to give an overall fit to the multiple data sets. Said another way, the average χ^2 describes the quality of position-of-interaction reconstruction for each fiber. Lower χ^2 values indicate better fits to the truth data. Individual position resolution estimates from curves with values of χ^2 greater than 20 are rejected due to excess residual error. A summary of the attenuation length and position resolution measurements of F1-F5 are shown in Table 4. Results in red strike-through cells have been rejected either because of low R^2 or low χ^2 values (rejection source is highlighted in yellow).

Table 4. Attenuation lengths and position resolution of five YAG:Ce fibers measured using 405 nm laser induced photoluminescence

Fiber	Repitition	Attenuation Length, λ		Mean Spatial Resolution		
		[cm]	R^2	[mm]	χ^2	χ^2 Average
1	1	18.6	0.99	6.4	2.05	3.7
	2	17.5	0.98	6.5	2.59	
	3	24.5	0.99	3.6	3.13	
	4	20.3	0.98	4.7	6.36	
	5	21.1	0.99	3.9	4.57	
~~2~~	~~1~~	~~9.5~~	~~0.91~~	~~2.3~~	~~153.94~~	~~152.8~~
	~~2~~	~~10.9~~	~~0.86~~	~~2.6~~	~~213.27~~	
	~~3~~	~~9.5~~	~~0.89~~	~~2.2~~	~~185.77~~	
	~~4~~	~~9.8~~	~~0.87~~	~~2.7~~	~~113.78~~	
	~~5~~	~~10.7~~	~~0.86~~	~~2.9~~	~~97.09~~	
3	1	24.6	0.99	7.2	1.08	2.2
	2	31.0	0.98	5.5	4.00	
	3	29.3	0.98	7.5	1.45	
~~4~~	~~1~~	~~17.3~~	~~0.94~~	~~2.2~~	~~100.17~~	~~44.6~~
	~~2~~	~~14.0~~	~~0.95~~	~~5.0~~	~~17.91~~	
	~~3~~	~~14.5~~	~~0.96~~	~~3.4~~	~~27.60~~	
	~~4~~	~~13.1~~	~~0.95~~	~~2.9~~	~~50.00~~	
	~~5~~	~~14.2~~	~~0.95~~	~~3.5~~	~~27.55~~	
5	1	18.4	0.99	3.8	3.59	18.5
	2	14.5	0.97	3.7	12.78	
	3	14.6	0.96	3.4	18.62	
	4	15.1	0.96	~~2.9~~	~~32.05~~	
	5	16.8	0.96	~~3.1~~	~~25.69~~	

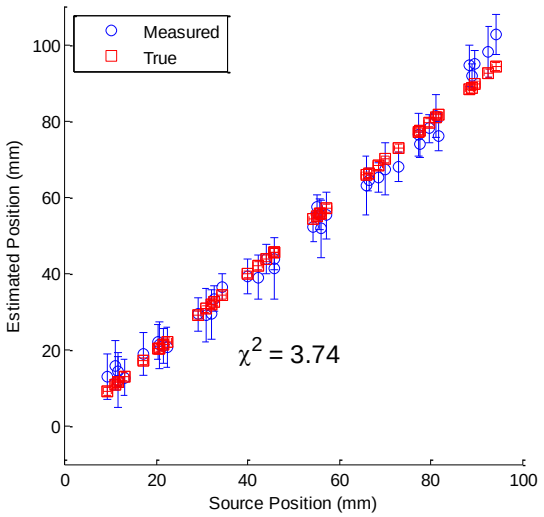

Fig. 63. Using measured attenuation length data, the photoluminescence position-of-interaction in F1 can be estimated. The error bars on the blue dots represent the position resolution (i.e. sample standard deviation) at that point. The red squares represent the true position-of-interaction. The size of the red squares is equal to the FWHM of the laser beam, 2.6 mm.

Of course, the assumption that the light attenuation follows (2.12) is essential to estimating position of interaction using a simple function. In other words, if the plot of $\log\left(\overline{N}_2 / \overline{N}_1\right)$ is not a straight line, the process described to estimate position fails. Such is the case for F2, as shown in Fig. 64 and Fig. 65. For example, the attenuation length measurements for fibers F2 and F4 are rejected essentially due their poor linear correlation. That is, the $\log\left(\overline{N}_2 / \overline{N}_1\right)$ is too non-linear to accurately model the optical attenuation properties using Beer's law.

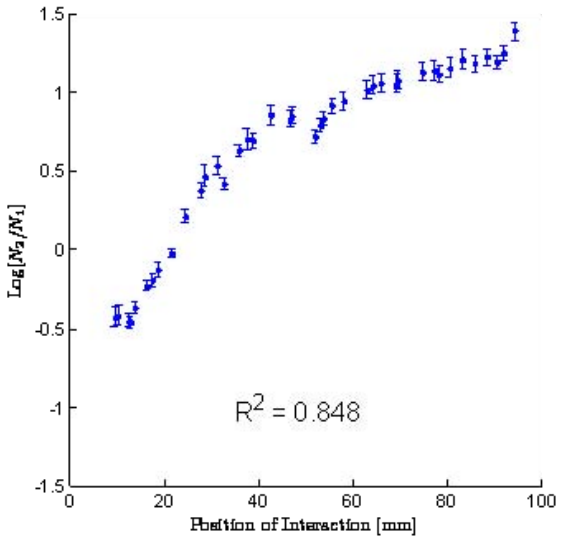

Fig. 64. The plot of $\log\left(N_2 / N_1\right)$ is not a straight line for F2. Shown are five independent and repeatable measurements. The exponential attenuation model does not provide an accurate description of the light propagation in F2. The error bars are computed by (4.4). R^2 is the coefficient of determination calculated by the square of the correlation coefficient. R^2 = 0.848 indicates a poor linear fit.

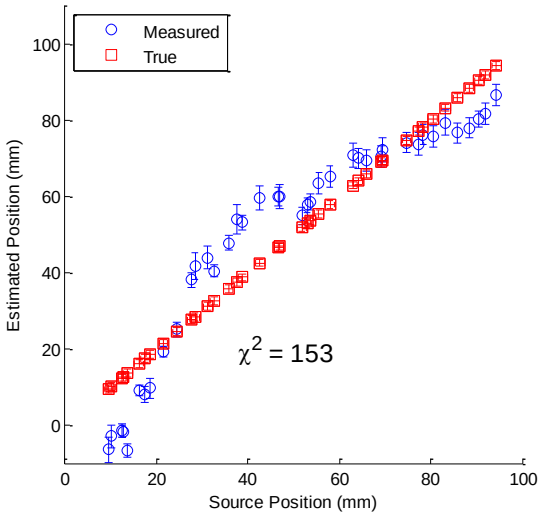

Fig. 65. Using an exponential attenuation model provides a poor reconstruction of the position-of-interaction in F2. The response is suspected to be due to a local imperfection near x=30 mm which causes disproportionate distribution of light intensity at the fiber end readouts due to reflection or absorption. The average χ^2 goodness-of-fit statistic is over 40 times higher than in F1 as shown in Fig. 63, indicating very poor position estimates.

The most reasonable explanation for the light propagation behavior observed in F2 is the presence of a localized region of absorption or reflection. A small imperfection in the crystal at approximately 30 mm from the end (i.e. the point of slope disjoint) is likely acting as an absorber or reflector of incident light. The light intensity measured on the side of the interaction is therefore disproportionately higher than the opposite side. As a result and according to the goodness-of-fit parameter χ^2, F1 position estimates are 40 times better than those from F2. Although F2 was inspected under a microscope, the presence of such an imperfection was not obvious. Ultimately the fiber was damaged during microscopy and the presence of the imperfection remains only conjecture.

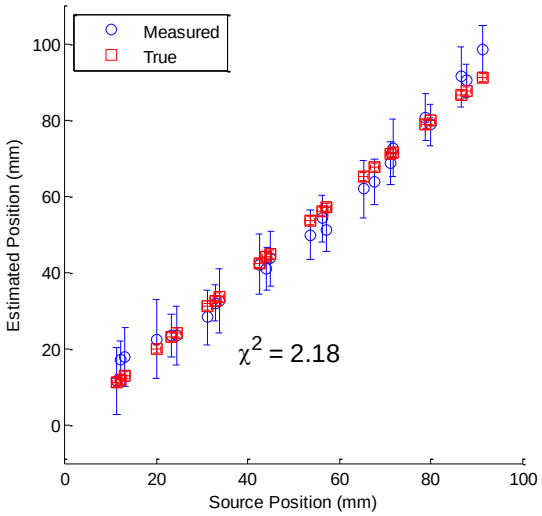

Fig. 66. Fiber F3 shows a position-of-interaction reconstruction slightly better than that of F1 as evidenced by the average χ^2=2.18. The size of the red squares is equal to the FWHM of the laser beam, 2.6 mm.

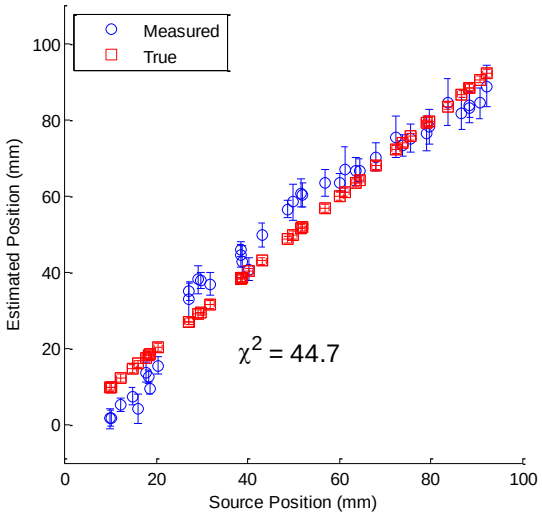

Fig. 67. The position-of-interaction reconstruction of F4, while better than F2, suffers from bias due to the faulty assumption that light propagation within the fiber follows an exponential attenuation model. The red squares represent the true position-of-interaction. The size of the red squares is equal to the FWHM of the laser beam, 2.6 mm.

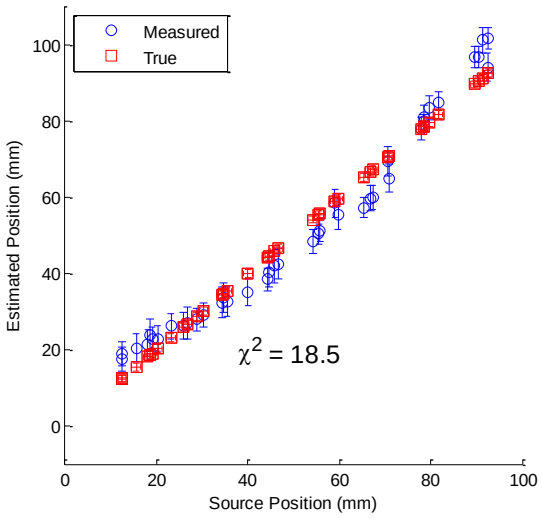

Fig. 68. Fiber F5 generally follows the exponential attenuation model for reconstructing position-of-interaction. The goodness-of-fit is better than F2 and F4, but not as good as either F1 or F3. The error bars on blue dots represent the position resolution at that point. The red squares represent the true position-of-interaction. The size of the red squares is equal to the FWHM of the laser beam, 2.6 mm.

Some attenuation length variation between fiber samples should be expected. No qualitative assessment of these fibers is offered. The measured attenuation lengths are somewhat repeatable. Discrepancies between repetitions of the same fiber are attributed to power fluctuations in the laser; power observably decreased by as much as 50% over the course of several minutes.

Care was taken to avoid MPPC saturation, but outliers are attributed to inadvertent saturation. For example, changes to the setting of the graduated neutral density filter account for the absent F3 data (i.e. repetitions four and five). The laser output power which was monitored throughout the experiment began to decline just prior to repetition four of F3; therefore the neutral density filter was reduced to allow more

laser light to pass through. During the measurements the laser power increased to its nominal level and mild MPPC saturation occurred. As the MPPC saturates due to photon pile up, $\log\left(\overline{N}_2 / \overline{N}_1\right)$ decreases and the data falsely indicates a more transparent crystal. Therefore, repetitions four and five for F3 are not presented.

Pile up saturation and laser power fluctuation may also explain the rather large range of attenuation length values measured for F1. As mentioned in Section III. 2. 3. , this saturation due to pile up may raise some concern over flaws in the methodology since the MPPCs (and SiPMs in general) are not designed to accurately count photons under continuous illumination from bright light sources. This methodology could be improved by using a pulsed laser with pulse widths on the order of pixel recharge times, around 20 ns or less.

2. 4. YAG:Ce Fiber Scintillation Position Resolution Results

To complement the photoluminescence experiment, the position resolution of the dual fiber end MPPC readout of YAG:Ce fibers was measured using scintillation. Unlike the large, stable MPPC signals (e.g. on the order of several thousands of pixels firing during the 250 ns integrating time) found in the laser photoluminescence experiment, the MPPC pixels which fire due to YAG:Ce alpha scintillation number in the hundreds. Consequently, the MPPC signals are not subject to the pile up saturation problems discussed above, but are subject to the inherent uncertainties associated with photon counting statistics. Therefore, the scintillation experiment to measure position resolution was simulated in DETECT2000 using three crystals of different attenuation lengths (e.g. 10 cm, 20 cm, and 30 cm) to predict the achievable position resolution; these simulations

are discussed at the end of Section III. 2. 3. In order to better understand the results of the experiments, the simulation results are first discussed.

A 1 MeV gamma equivalent event producing 17,000 photons was simulated at 1 cm increments between 1 cm and 9 cm along the YAG:Ce fiber axis. Using a polished surface treatment, DETECT2000 was used to simulate the trajectories of the photons until detection at the fiber ends. The experiment was repeated 30 times at each simulated position-of-interaction in order to estimate the mean number of photons in the scintillation flux (for the given number of total scintillation photons). The scintillation photon flux was then modeled as Poisson distributed random variables from which a random number of MPPC pixels fired in accordance with binomial statistics and the PDE of the MPPC (e.g. 15% at 550 nm). The mean number of MPPC pixels which fire is plotted as a function of interaction position in Fig. 69 through Fig. 71.

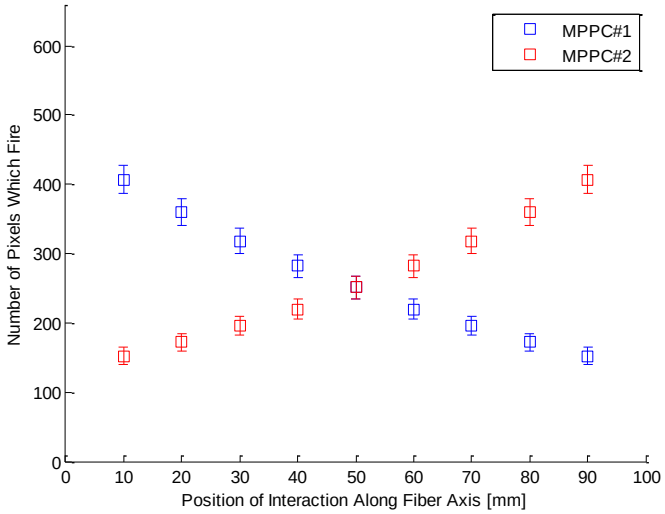

Fig. 69. The mean number of simulated MPPC pixels firing is shown as a function of interaction location along a YAG:Ce fiber with an attenuation length of 10 cm. The error bars indicate the standard deviation of the number of pixels based on counting statistics.

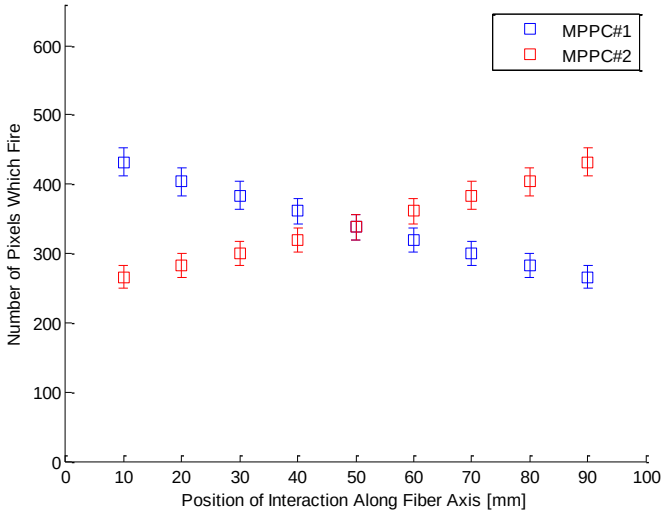

Fig. 70. The mean number of simulated MPPC pixels firing is shown as a function of interaction location along a YAG:Ce fiber with an attenuation length of 20 cm. The error bars indicate the standard deviation of the number of pixels based on counting statistics.

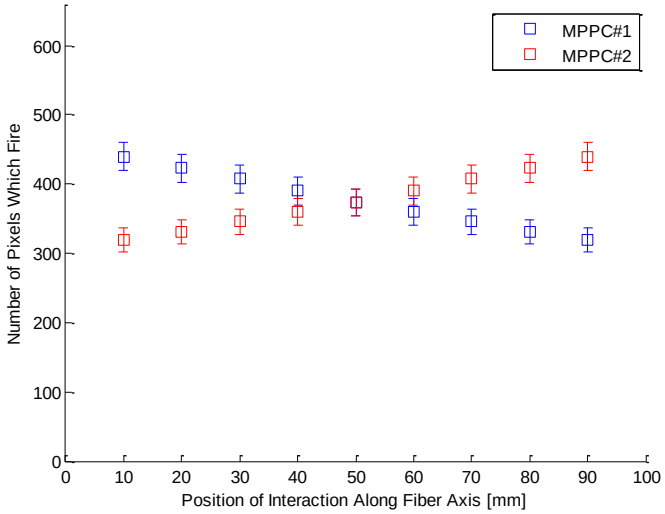

Fig. 71. The mean number of simulated MPPC pixels firing is shown as a function of interaction location along a YAG:Ce fiber with an attenuation length of 30 cm. The error bars indicate the standard deviation of the number of pixels based on counting statistics.

Since the number of pixels which fire is a random variable, there is inherent position uncertainty which is conditioned on the number of total scintillation photons, see

(2.21). Of course, in reality the number of initial scintillation photons is a random variable as is the energy deposited by ionizing radiation which is a stochastic process, further complicating calculation of the position resolution predicted by (2.21). Supposing that full energy events (i.e. events under the alpha peak) can be discriminated electronically or by digital processing, then the number of initial scintillation photons can be treated deterministically based on the expected light yield of the material, thereby simplifying the position resolution calculations. Full energy peak discrimination is the underlying premise of the following analysis of the simulated results which is intended only to provide insight about the lower bound of the achievable position resolution.

Using the mean number of firing pixels, 50,000 MPPC measurements were simulated in accordance with the stochastic process model for MPPC pixel firing. The simulated data were used to reconstruct an estimate of the position-of-interaction on an event-by-event basis. The simulated results of the position-of-interaction reconstruction are shown in Fig. 72 and Fig. 73.

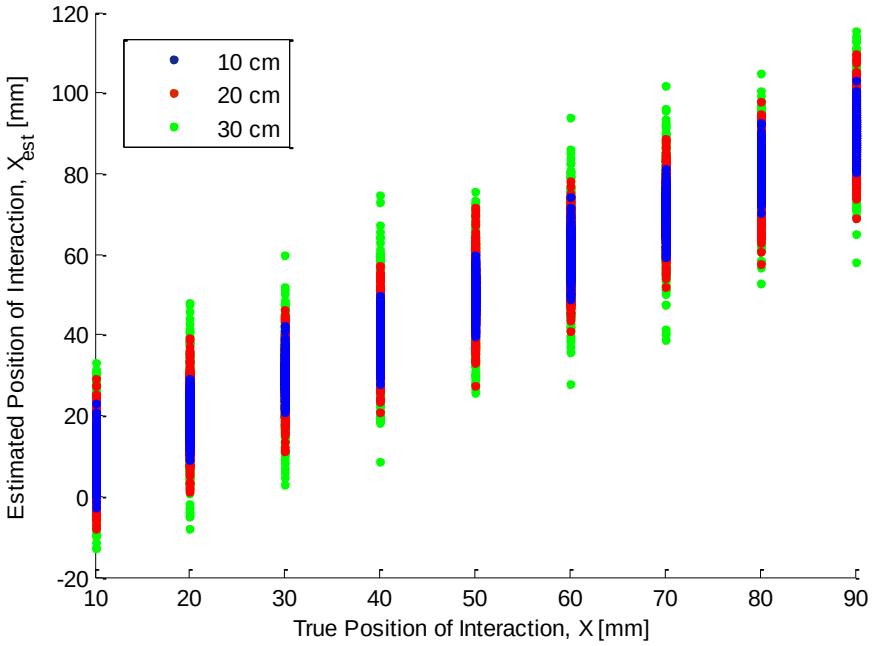

Fig. 72. Simulated results of the position-of-interaction reconstruction using a Monte Carlo method to model the stochastic process of MPPC pixels firing are shown for three crystals of different attenuation lengths. In aggregate, the simulated results accurately reconstruct the position-of-interaction. The spread in data is due solely to the random nature of the MPPC response, in accordance with binomial statistics. The different colors are associated with the different attenuation lengths of the crystals: blue is 10 cm, red 20cm, and green 30 cm.

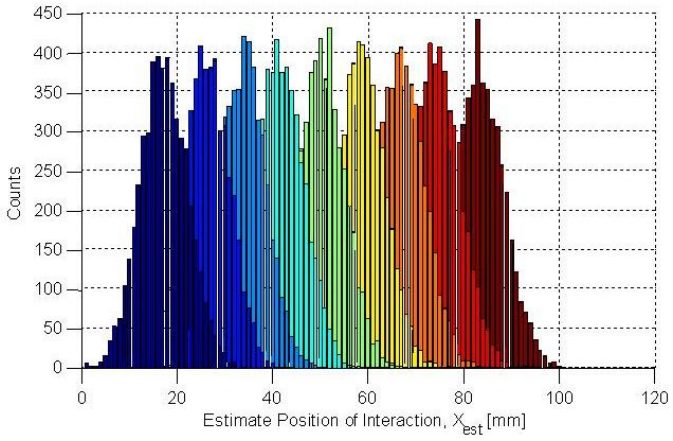

Fig. 73. The simulated position-of-interaction reconstruction data from the 30 cm attenuation is shown as a histogram. The different colors indicate different true positions-of-interaction. The spread in the data (i.e. the standard deviation) is the ideal position resolution.

Using the mean number of firing MPPC pixels shown in Fig. 69 – Fig. 71 for each of the three simulated fiber crystals, the ideal position resolution is calculated by (2.21). The analytical results are compared to the results of a Monte Carlo simulation of MPPC signal dispersion due to random fluctuations shown in Fig. 72; the comparatrive results are shown in Fig. 74.

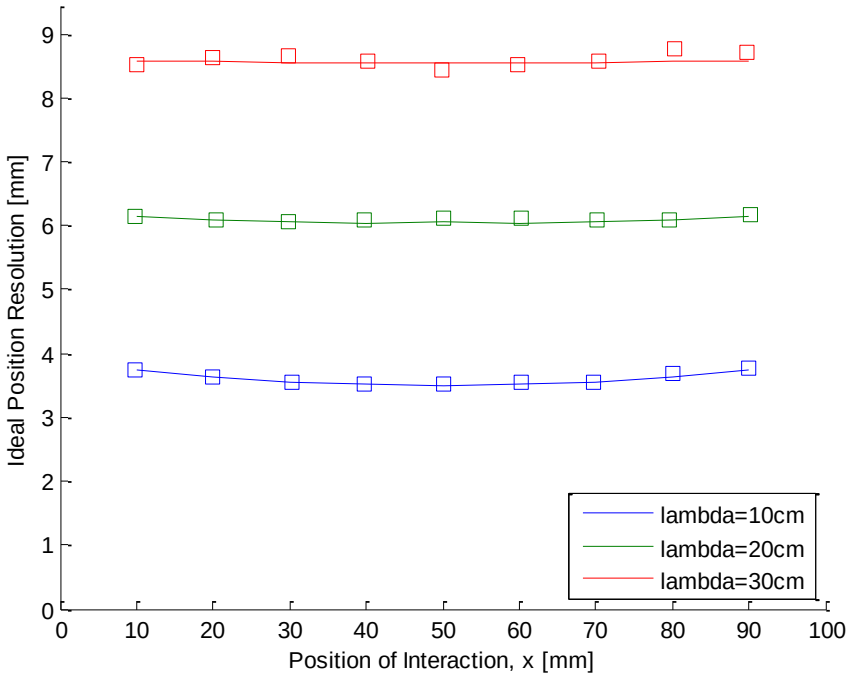

Fig. 74. Ideal position resolution of a 1 MeV (gamma equivalent) scintillation pulse in three YAG:Ce fibers of different attenuation lengths using dual fiber end MPPC readout is shown. The lines represent the analytical position resolution which is described by (2.21). The squares represent the results of Monte Carlo simulations of the MPPC pixel firing process given a simulated scintillation photon flux modeled in DETECT2000.

Intuitively, more transparent crystals (i.e. those with longer attenuation lengths) have less relative difference between the two fiber end readouts; this is seen by the relative slopes in Fig. 69 – Fig. 71. Recall from the discussion surrounding (2.21) that

the ideal achievable position resolution degrades as the crystal becomes clearer despite improving the ideal achievable energy resolution. Using (2.19), the ideal energy resolutions given a 17,000 photon scintillation event are shown in Fig. 75.

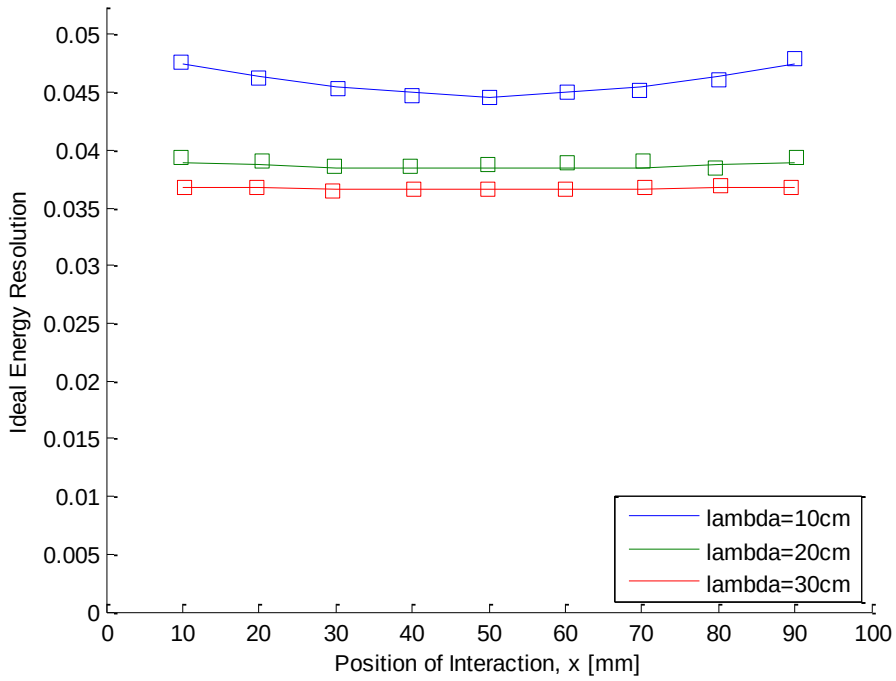

Fig. 75. Ideal energy resolution of a 1 MeV (gamma equivalent) scintillation pulse in three YAG:Ce fibers of different attenuation lengths using dual fiber end MPPC readout is shown. The lines represent the analytical energy resolution which is described by (2.19). The squares represent the results of Monte Carlo simulations of the MPPC pixel firing process given a simulated scintillation photon flux modeled in DETECT2000.

Recall that the data shown in Fig. 69- Fig. 71 is shown using full energy event discrimination for simplicity. In a Compton imaging application, even low energy Compton scattering events are necessary to form an image. Therefore, uncertainties in energy and position resolution must be calculated in real-time on an event-by-event basis.

The results of the Monte Carlo simulation verify the application of (2.19) and (2.21) for such imaging applications.

In addition to simplifying both the discussion and computation of the ideal energy and position resolutions achievable in a YAG:Ce fiber with dual end MPPC readouts, the deterministic number of scintillation photons (e.g. 17,000 per 1 MeV gamma equivalent event) was chosen for the simulations as a reasonable approximation to the expected light yield from full energy 5.4 MeV alpha scintillation events. The data presented therefore represent a reasonable, albeit idealized, lower bound of energy and position resolution which can be achieved from the scintillation experiments. At best, a position resolution of 4-9 mm can be achieved in a readout system without excess noise, depending upon the fiber attenuation length. Worse performance must be expected for any event of less than full energy deposition.

Before presenting the experimental results, it is appropriate to discuss some interesting findings from the simulations. As in the experimental results, the attenuation length of the crystal is required to produce an estimate of the position-of-interaction. Interestingly, the estimated attenuation length is less than the parameter specified in the DETECT2000 simulations. The "measured" (i.e. from simulated data) attenuation lengths of the three crystals were 7.9, 16.0, and 23.7 cm rather than the specified 10, 20, and 30 cm respectively. This result directly corresponds to the mean path length of the photons in the crystal fiber before being detected. On average, the photons travel nearly 1.25 times further than their axial position in the fiber before being detected. Therefore, the *effective* attenuation length of the crystals is approximately $0.8\,\lambda_{bulk}$, which agrees with results published by Vilardi, *et al*., in [**22**]. The true value of the bulk attenuation

length is inconsequential since one is constrained to using the effective attenuation length in this application. However, it is important to be mindful of this fact when selecting crystals based on reported bulk attenuation lengths for dual fiber readout applications.

Now, the results from the position-of-interaction experiment conducted using the collimated ^{241}Am alpha source are presented. First, the mean number of MPPC pixels which fire is estimated by integrating the charge released in each recorded digital waveform. Pixel firing results from F1 are shown in Fig. 76.

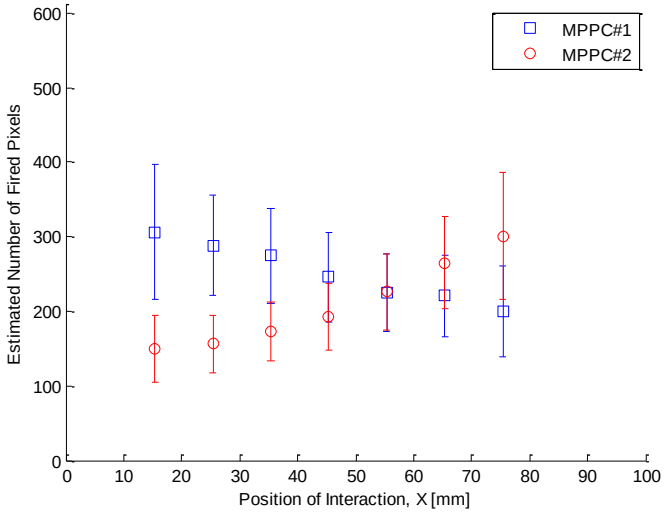

Fig. 76. The mean number of MPPC pixels firing in response to alpha scintillation in F1. The error bars represent the standard deviation of the measured pixel response data. It is important to recall that low energy events are not discriminated in the collection or processing of these data. The lack of symmetry is due to the damaged, less efficient MPPC#2.

From the MPPC response data presented in Fig. 76, the mean number of pixels firing in response to alpha scintillation is significantly lower than predicted by the simulation, see Fig. 69-Fig. 71. This is attributed to the presence of low energy events (i.e. other than full energy peak) and poor optical coupling. The result is the inclusion of

events with necessarily poorer energy and position resolution. That said, the majority of events should fall under the broad alpha peak seen in Fig. 52.

Additionally, one can observe asymmetry in the pixel response due to the damaged, less efficient MPPC#2. If both MPPCs had the same gain response and efficiency, one would expect the lines to cross at the center of the fiber, 50 mm. This asymmetry has implications on the achievable energy and position resolution, as will be shown.

The discussion now returns to the experimental results. As in the photoluminescence experiments, the attenuation lengths were computed using the slopes of linear-least-squares-fit of $\log\left(\overline{N}_2 / \overline{N}_1\right)$. The positions-of-interaction are then reconstructed using the measured attenuation length and the position resolution is defined as the sample standard deviation of the resulting distribution. The reconstruction of the position-of-interaction is shown for F1-F5 in Fig. 77-Fig. 82. The R^2 values of the $\log\left(\overline{N}_2 / \overline{N}_1\right)$ plots and χ^2 values of the x plots are computed identically as well. For attenuation length measurements, as with the photoluminescence experiment, values of R^2 less than or equal to 0.95 are rejected. However, because the inherent position uncertainties are much higher (due to counting statistics), the χ^2 values as defined by (4.5) are necessarily smaller in value than those computed during photoluminescence experiments. The mean χ^2 values are approximately an order of magnitude less for the scintillation results. As such, the χ^2 values between experiments are not comparable and values greater than 2.0 result in the rejection of the position resolution measurement. A summary of the experimental attenuation length and position resolution results can be

found in Table 5. Rejected values are shown in red strike-through font; the yellow highlighted cell indicates the source of rejection.

Table 5. Attenuation lengths and position resolutions measured in five YAG:Ce fibers using scintillation from a 5.4 MeV alpha source

Fiber	Repitition	Attenuation Length, λ		Mean Spatial Resolution		
		[cm]	R^2	[mm]	χ^2	χ^2 Combined
1	1	15.2	0.99	16.8	0.28	0.37
	2	11.4	0.99	12.6	0.31	
	3	11.7	0.99	11.4	0.52	
~~2~~	~~1~~	~~18.0~~	~~0.92~~	~~19.2~~	~~0.64~~	~~4.10~~
	~~2~~	~~13.2~~	~~0.80~~	~~12.5~~	~~6.65~~	
	~~3~~	~~13.5~~	~~0.81~~	~~12.5~~	~~4.97~~	
3	1	23.4	0.98	21.1	0.17	0.14
	2	24.6	0.99	23.2	0.11	
	3	24.8	0.98	22.2	0.12	
4	1	17.9	0.99	18.6	0.24	0.32
	2	18.2	0.99	18.8	0.21	
	3	16.0	0.96	17.4	0.51	
5	1	16.4	0.99	17.3	0.21	0.33
	2	15.9	0.98	16.7	0.34	
	3	15.1	0.98	15.2	0.44	

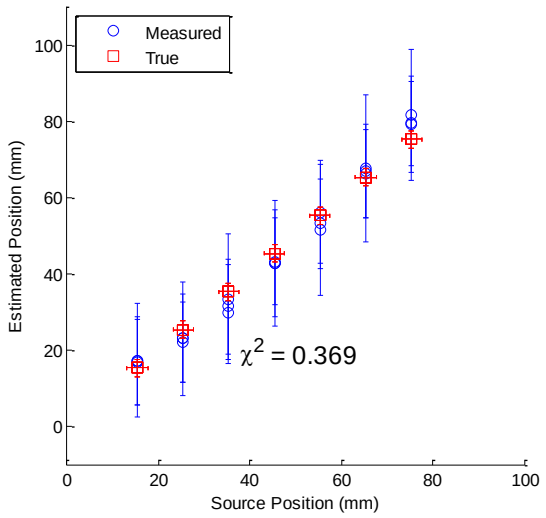

Fig. 77. The reconstruction of alpha particle position-of-interaction within F1 is shown. The blue circles are the mean of the position-of-interaction estimates using (2.13) with position resolution as error bars. The red squares represent true source positions; the size of the squares is equal to the 2.4 mm beam width of the collimated alpha source.

Recall that light propagation within F2 did not resemble the exponential attenuation during the photoluminescence experiments. The same phenomenon was observed in the scintillation experiments, but with much more drastic impact. The fiber orientation was unintentionally flipped during mounting for these experiments. That is, the defect observed at 30 mm during the photoluminescence experiments is now at 70 mm. The overall number of pixels which fire is drastically reduced at the opposite fiber end. This problem is exacerbated by placing the defective side on MPPC#2, the damaged and less efficient MPPC. The estimated number of fired pixels as a function of source position is plotted in Fig. 78 for F2. As a consequence of the extremely low number of pixels firing, the position resolution achieved by F2 in the scintillation experiments is terrible, seen in Fig. 79.

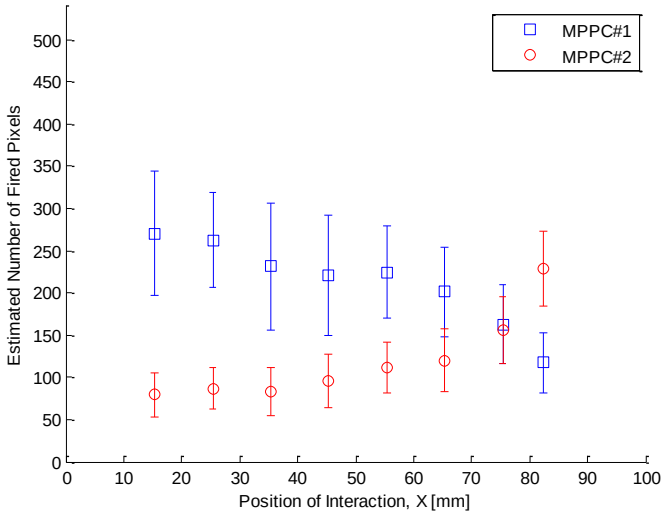

Fig. 78. The discrepancy between the light propagation in F2 and the expected exponential attenuation which was observed in the photoluminescence experiments is repeatable in the scintillation experiment. Here, the fiber has been flipped so the disjoint due to suspected optical defects is observed by the change in slope near 70 mm rather than 30 mm. The defective fiber is on the side closest to the damaged MPPC#2 resulting in low numbers of fired pixels and consequently terrible position resolution.

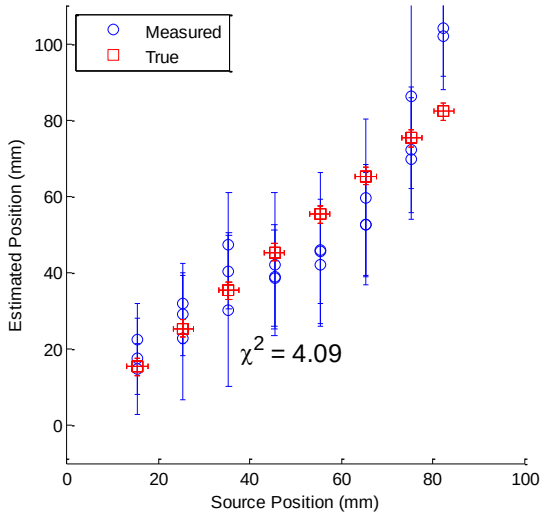

Fig. 79. The accuracy and resolution of the alpha position-of-interaction reconstruction in F2 is very poor due to the low number of fired MPPC pixels. Additionally, the light propagation discrepancy observed for F2 during the photoluminescence experiments is again observed in scintillation experiments and is responsible for the over 10 times worse χ^2 compared to F1.

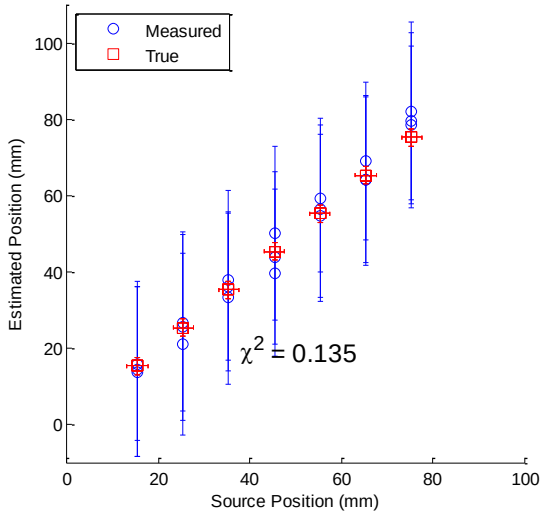

Fig. 80. The reconstruction of the alpha particle position-of-interaction within F3 is shown. The blue circles are the mean of the position-of-interaction estimates using (2.13) with position resolution as error bars. The red squares represent true source positions; the size of the squares is equal to the 2.4 mm beam width of the collimated alpha source.

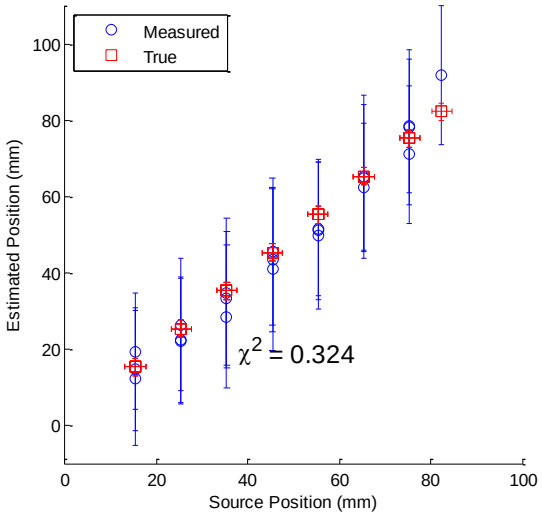

Fig. 81. The reconstruction of the alpha particle position-of-interaction within F4 is shown. The blue circles are the mean of the position-of-interaction estimates using (2.13) with position resolution as error bars. The red squares represent true source positions; the size of the squares is equal to the 2.4 mm beam width of the collimated alpha source.

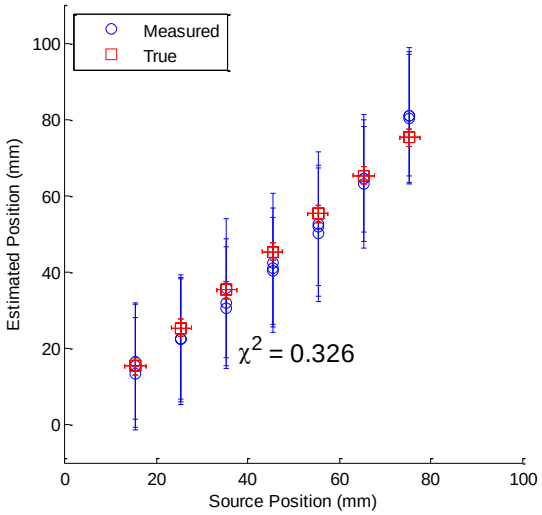

Fig. 82. The reconstruction of alpha particle position-of-interaction within F5 is shown. The blue circles are the mean of the position-of-interaction estimates using (2.13) with position resolution as error bars. The red squares represent true source positions; the size of the squares is equal to the 2.4 mm beam width of the collimated alpha source.

With exception of the terrible performance of F2 which has already been discussed and rejected, the position-of-interaction reconstruction showed good aggregate performance (i.e. no rejections due to large χ^2), indicating that the exponential attenuation is a reasonable model for the light propagation within YAG:Ce fibers including F4 which was rejected from photoluminescence measurements due to poor R^2 values.

With some exceptions, the attenuation lengths measured in the scintillation measurements agree with the photoluminescence results found in Table 4. The general trend in fiber performance is in agreement. Fiber F3 is the most transparent according to both data sets with an attenuation length of ~25 cm. Fibers F1, F4, and F5 all have attenuation lengths between ~13-20 cm. Overall, the scintillation measurements provided much more repeatable attenuation length measurements. As discussed, this may be attributable to flaws in the photoluminescence methodology caused by photon pile up saturation.

The large error bars in Fig. 77 - Fig. 82 indicate relatively poor position resolution, which may be a result of a lower than expected number of pixels firing as a result of lack of full energy discrimination or poor optical coupling. The best overall measured position resolution was 11 mm using F1. The worst overall position resolution (ignoring the defective F2) was 23 mm using F3. As expected from (2.21), the most transparent crystal (i.e. F3 has the longest attenuation length) has the worst position resolution while the most opaque (i.e. F1 has the shortest attenuation length) has the best position resolution. However, assuming the measured attenuation lengths are reasonably accurate, the measured position resolution is a factor of two worse than the ideal position resolutions of the simulated crystals, see Fig. 74.

Additional noise factors such as the fluctuations in pixel gain and discharge, as well as the integration of cross-talk, after pulses, and dark counts, as well as electronic noise from the oscilloscope are also likely contributors to the poor position resolution. These noise sources are exacerbated by the very slow decay component and low overall light yields of the YAG:Ce fibers which necessitate the use of long integration times and excessive bias voltages (in order to directly digitize MPPC readouts). Johnson *et al.* include these noise sources in the excess noise factor term in (2.30) [**50**]. While cross-talk and dark count rates can be directly measured, after pulsing is more difficult to quantify. Prompt after pulsing occurs when the pixel is retriggered before recharging fully and the charge released is less than that of a full pixel discharge. Delayed after pulsing (i.e. after the pixel is recharged) is difficult to distinguish from dark counts. For these reasons, the excess noise from after pulses is neglected in the following analysis.

The variation in the pixel gain is difficult to distinguish from the oscilloscope noise in the measurements shown in Fig. 32 and Fig. 38 and is termed electronic noise. From the measurement of the FWHM of the single fired pixel distributions, the relative electronic noise is ~7%. From Fig. 40, one can see that the probability of MPPC pixel cross-talk is 12-13% at 73 V, the bias voltage used in these experiments. Thus, the number of pixels firing as a result of true photon detection is less than the measured value. Since, the dark count rate was measured between 200-300 kHz , the excess noise effects from dark counts are negligible during a 1 μs integration time. Of course, to accurately estimate the overall excess noise factor, one must measure the MPPC signal dispersion using a calibrated light source as in [**50**]. In [**50**], Johnson *et al.* report similar

values of cross-talk and excess noise factors between 1.08 and 4.19 depending on operating bias.

To explain the worse than predicted measured position resolution, the experiment was again simulated, but under modified conditions in order to model the asymmetric MPPC readout efficiencies and match the mean number of fired pixels (shown in Fig. 76). This was accomplished by reducing the PDE of MPPC#1 from 15% to 11% and by reducing the PDE the damaged MPPC#2 from 15% to 9%. Additionally, the DETECT2000 simulation was adjusted to simulate λ_{eff} equal to 13 cm, in accordance with the measured F1 attenuation length (see Table 5). Additionally, an arbitrarily chosen excess noise factor term of 1.7 is applied to the theoretical calculations and Monte Carlo simulations. The excess noise value is selected empirically to fit the data and, while arbitrary, is reasonable according to results published in [**50**]. The results are compared to the F1 measurements in Fig. 83 and Fig. 84.

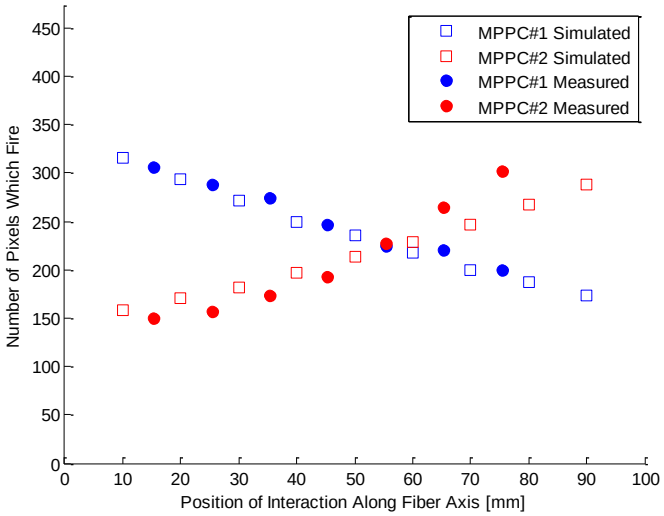

Fig. 83. The poor optical coupling of the scintillator and MPPC and the damage to MPPC#2 was simulated and compared to the measured MPPC response. The photon detection efficiencies of MPPC#1 and MPPC#2 were reduced from 15% to 11% and 9%, respectively. Only the means of the measured data are shown; the data are presented without error bars for clarity. The error bars can be found in Fig. 76.

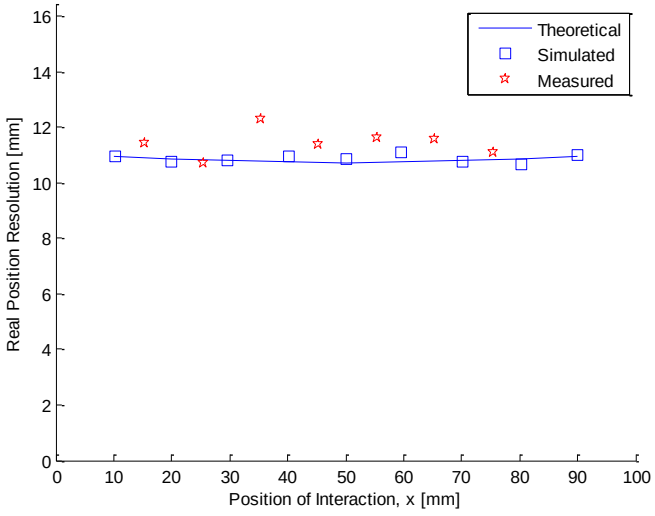

Fig. 84. The position resolution of the asymmetric simulation is shown with an excess noise factor of 1.7, chosen to match the measured position resolution of F1.

The best position resolution (measured using F1) seems to reasonably match the theoretical and simulated values with an excess noise factor of 1.7, suggesting very poor

noise performance of the system. The excess electronics noise could be avoided in the future with proper instrumentation (e.g. incorporating a customized charge integrating pre-amplifier into the MPPC readout circuit front end). The excess noise due to cross-talk and after pulses could then be minimized by reducing the required operating bias. Better optical coupling between the MPPC and the scintillator could also improve the overall performance of the system. However, the low Birks' figure of merit value (e.g. $M \approx 68$ ph ns^{-1} MeV^{-1}) of YAG:Ce is a fundamental limitation of the signal-to-noise performance of the system.

2. 5. Improving System Resolution

Despite their slow decay component and subsequent low Birks' figure of merit value, the YAG:Ce fibers are not the limiting factor in the achievable position resolution of the dual end MPPC readout system. Instead, the real culprit is the MPPC which has a PDE of 15% at the peak of YAG:Ce emission. According to the DETECT2000 simulations, between 1000 and 3000 scintillation photons arrive at each MPPC detector surface, depending on the fiber attenuation length. By essentially throwing away 85% of them, the MPPC devastates the achievable energy and position resolution of the system. This efficiency limitation is due to the low geometric fill factor of the 1600 pixel MPPC (30.8% [**45**]), required to reduce cross-talk. Although a greater number of pixels allows for greater dynamic range and less saturation, a device with far fewer pixels and a much higher fill factor is better suited for scintillators with low Birks' figure of merit values because the *effective* number of pixels (due to pixel recharge during the long scintillation pulse) will allow proportional response, but the device will be much more efficient. For example, the S10362-11-100C and -50C are the 100 and 400 (78.5% and 61.5% fill

factors, respectively [**45**]) pixel versions of the MPPC used in this research and they have respective PDEs of 55% and 35% at 550 nm [**45**]. To illustrate the improvement to the detector system by simply replacing the MPPC with a more efficient model, the Monte Carlo simulations and analytical calculations of ideal energy and position resolution were repeated using the S10362-11-100C 100 pixel device. The results are shown in Fig. 85 - Fig. 87.

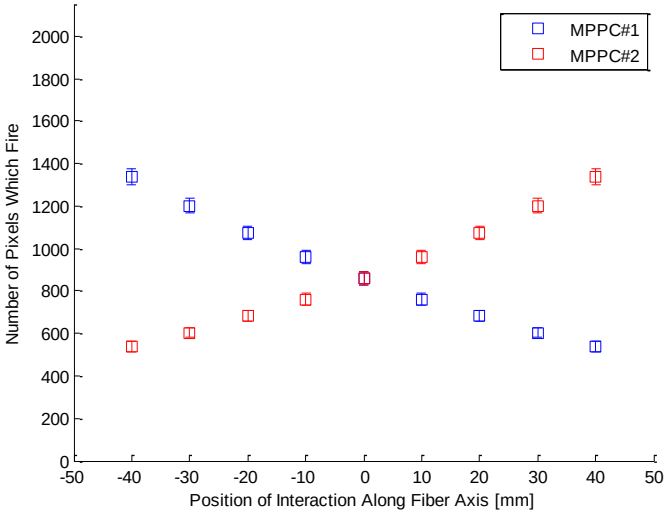

Fig. 85. The number of simulated pixels which fire using the more efficient S10362-11-100C 100 pixel Hamamatsu MPPC is drastically increased over the 1600 pixel MPPC used in this research when coupled to a YAG:Ce fiber with a simulated attenuation length of 10 cm.

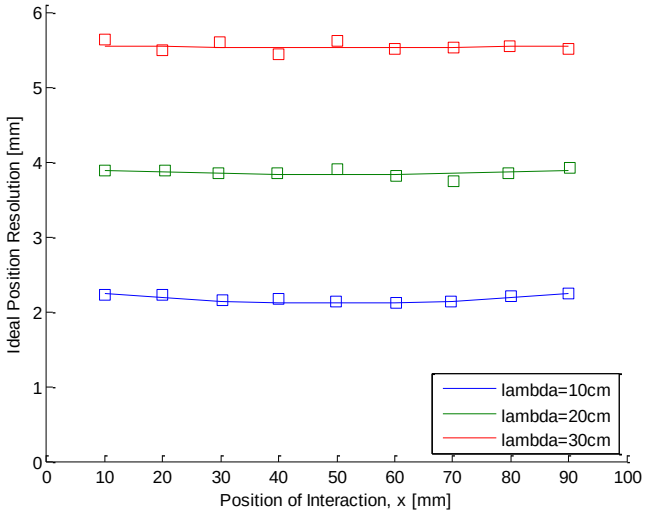

Fig. 86. The achievable position resolution of a 1-MeV (gamma equivalent) scintillation event in a YAG:Ce fiber is significantly improved when readout using a more efficient 100 pixel MPPC as opposed to the inefficient 1600 pixel MPPC used in this research. Any effects of saturation are ignored. Lines indicate the analytical solution and squares indicate the results of Monte Carlo simulations.

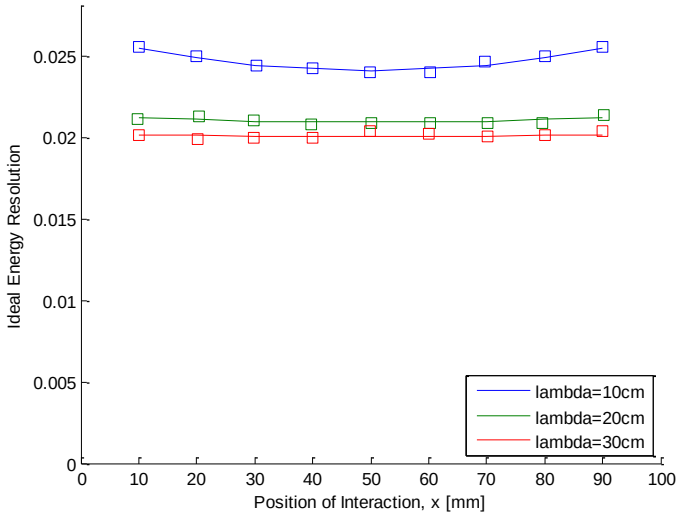

Fig. 87. The achievable energy resolution of a 1-MeV (gamma equivalent) scintillation event in a YAG:Ce fiber is significantly improved when readout using a more efficient 100 pixel MPPC as opposed to the 1600 pixel MPPC used in this research. Any effects of saturation are ignored. Lines indicate the analytical solution and squares indicate the results of Monte Carlo simulations.

It is clear from the simulated results shown in Fig. 85-Fig. 87, that the MPPC chosen for these experiments was suboptimal. Both the ideal achievable energy and position resolutions were improved by as much as a factor of two simply by substituting 100 pixel MPPCs for the 1600 pixel MPPCs. However, these results ignored the effects of MPPC saturation which increases as N_{pixels} decreases and PDE increases.

The risk of saturation from using a 100 pixel MPPC is especially high since the 400 μm diameter YAG:Ce fiber only covers 12.5% of the 1 mm^2 active area. To determine the best MPPC model for this application, one must substitute

$$N_{pixels}^{eff} = \frac{Area_{YAG}}{Area_{MPPC}} \cdot N_{pixels} \frac{\tau_{shape}}{\tau_{recharge}} = 0.125 \cdot \frac{1000\,ns}{20\,ns} \cdot N_{pixels} = 6.25 \cdot N_{pixels} \qquad (4.6)$$

for N_{pixels} in (2.26) and compute (2.28) using the expected number of scintillation photons from the DETECT2000 simulations (e.g. 1000-3000 for YAG:Ce depending on λ). The ratio $Area_{YAG} / Area_{MPPC}$ is simply the percentage of the MPPC active area covered by the scintillating fiber footprint. The shaping and recharge times, τ_{shape} and $\tau_{recharge}$, are 1000 and 20 ns, respectively. The results of these computations are shown in Fig. 88 for 100, 400, and 1600 pixel MPPCs with their respective PDEs. Note that the MPPC intrinsic amplitude resolution results presented in Fig. 88 are from single fiber end MPPC readout simulations which cannot be compared to previously reported energy resolution results which were computed using (2.19) for double end readouts.

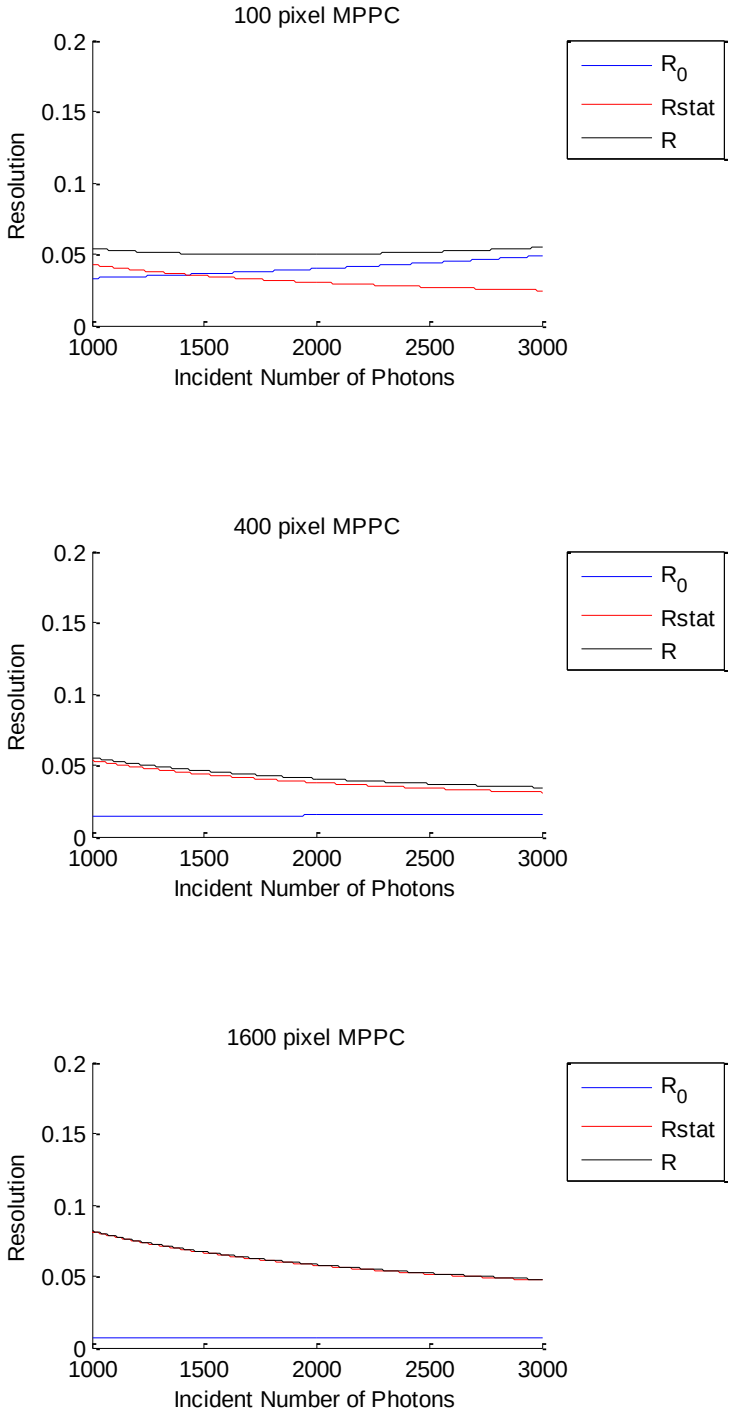

Fig. 88. The intrinsic amplitude resolutions of the 100, 400, and 1600 pixel MPPCs in response to a 1 MeV (gamma equivalent) scintillation event in a 400 μm diameter YAG:Ce fiber were computed using (2.28) and are shown from top to bottom. The contribution from saturation is R_0 while the contribution from counting statistics is Rstat. Note that the resolution values are reported as $\left(\sigma_E / E\right) = R_{FWHM} / 2.35$, not the FWHM.

Again, as shown in Fig. 88, the 1600 pixel MPPC was clearly a poor choice for this application. The best choice for this application is the 400 pixel MPPC. As expected, the contribution from saturation effects is essentially negligible for both the 400 and 1600 pixel MPPC. However, saturation is the limiting factor for the intrinsic resolution of the 100 pixel MPPC. This is primarily due to the size of the fiber relative to the MPPC. If the areas of the scintillator and MPPC are matched, the effect from saturation, and consequently the intrinsic resolution, is reduced. Evidence for this claim is provided in Fig. 89.

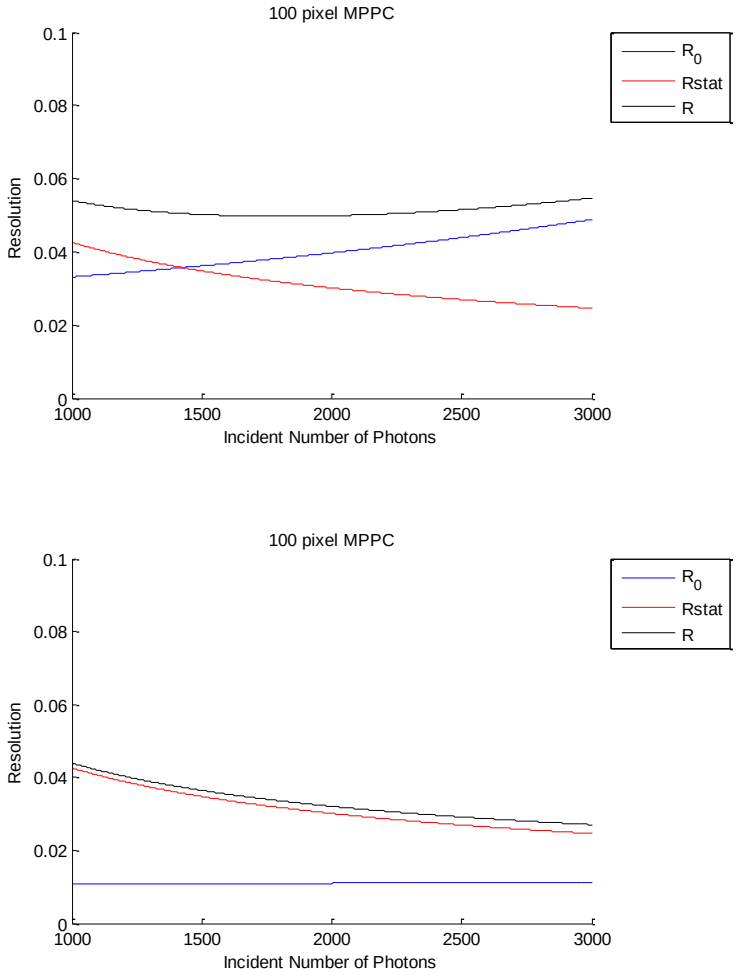

Fig. 89. The intrinsic amplitude resolutions of the 100 MPPC in response to a 1 MeV (gamma equivalent) scintillation event in 400 µm and 1 mm diameter YAG:Ce fibers were computed using (2.28). The top plot shows the effect from saturation resulting from fewer available pixels due to the surface area mismatch between a 400 µm fiber to a 1 mm^2 MPPC. The bottom plot shows the improvement of matching scintillator and MPPC areas. The contribution from saturation is R_0 while the contribution from counting statistics is Rstat. Note that the resolution values are reported as $\left(\sigma_E / E\right) = R_{FWHM} / 2.35$, not the FWHM.

As shown in Fig. 89, the impact on intrinsic resolution from MPPC saturation is drastically reduced if the YAG:Ce fiber diameters were matched to the dimensions of the MPPC active area. In fact, the 100 pixel MPPC becomes the best solution of the three available Hamamatsu models under these conditions. While using thinner fibers allows

for more inherent precision for particle tracking, no additional spatial interaction information is preserved by using scintillators with smaller cross-sections than the MPPC readout. Therefore, the best solution for continuation of this research is a 100 pixel Hamamatsu S10362-100C MPPC coupled to a 1 mm diameter YAG:Ce fiber.

For fibers other than YAG:Ce, the Birks' figure of merit of the scintillator can be used to approximate the best number of pixels for the application. Recall from Section II. 5. 5. that the intrinsic resolution described by (2.28) has an absolute minimum of $\alpha = 1.59$, where α is now defined as the mean number of photoelectrons per *effective* pixel defined as $\alpha = PDE \cdot N_{photons} / N_{pixels}^{eff}$. One can rewrite α in terms of the scintillating material's Birks' figure of merit, M, by

$$\begin{aligned} \alpha &= \frac{PDE \cdot N_{photons}}{N_{pixels}^{eff}} = \frac{PDE \cdot \varepsilon_{Fiber} \cdot L \cdot E_{\gamma} \cdot \tau_{recharge}}{N_{pixels} \cdot \tau_{shape}} \\ &= \frac{PDE \cdot \varepsilon_{Fiber} \cdot \tau_{recharge}}{N_{pixels} \cdot \zeta} \frac{L_S}{\tau} = \frac{PDE \cdot \varepsilon_{Fiber} \cdot \tau_{recharge}}{N_{pixels} \cdot \zeta} M \end{aligned} \tag{4.7}$$

where ε_{Fiber} is the efficiency of light collection, transmission, and escape in a single end of the scintillating fiber (which can be modeled in DETECT2000 and is approximately 15-20% for n=1.8 materials when using detector index matching fluid), and ζ is the length of integration time in terms of the number of scintillator decay time constants, τ. Typical ζ values range between 5 and 6. The total scintillation light yield, L_S, is a function of the light yield of the material, L (in units of photons per MeV), and the energy deposited by a 1 MeV (i.e. gamma equivalent) quantum of ionizing radiation, E_{γ}. By substituting the various MPPC parameters and scintillator Birks' figure of merit into

(4.7) and then into (2.28), one can determine which MPPC model will provide the best signal amplitude resolution for a given application.

As MPPC technology continues to improve, devices with even more pixels, higher PDEs and lower noise may usher in the end of scintillation counting using traditional PMTs. At some point, the achievable energy resolution of even low light yield scintillation detector systems may be limited by the intrinsic resolution of the scintillator rather than the material's light yield. Additionally, as garnet crystal growth using μ-PD continues to improve, the presence of anti-site defects and their resulting shallow charge carrier traps will diminish, thereby producing scintillators with faster and higher intensity fast decay components. Indeed, the future for this type of scintillation detector system is bright.

V. Conclusion, Summary, and Recommendations

The background, motivation, theory, methodology, and results of this research have been presented. The ability to calorimetrically measure and track gamma ray interactions in bundles of scintillating fibers has important applications in numerous fields ranging from medical imaging to national security. Compton imaging of SNM at standoff ranges is one such application. This research focused on predicting, modeling, and measuring the achievable energy and position resolutions in YAG:Ce fiber crystals using SiPMs for such an application.

Inorganic fiber scintillators coupled to highly efficient SiPMs is a promising new concept for a gamma ray detection system. Unfortunately, due to the inefficiency (i.e. low density, low effective Z) of the material and its small volume, no energy resolution could be measured using a single 400 µm YAG:Ce fiber with dual end MPPC readout. Radial dispersion of cerium activator concentration caused by growth via µ-PD is suspected to cause smearing of high gamma interactions due to the large range of recoil and photoelectrons in YAG:Ce.

Alpha and gamma radiation interactions in YAG:Ce fibers showed different scintillation decay times, as reported in literature. However, the fast and slow components did not change substantially as observed by Ludziejewski, *et al.*, and Moszynski, *et al.*; instead, only a change in relative decay component intensities was observed between alpha and gamma irradiation. Additionally, the alpha scintillation fast component was consistently measured above 113 ns in all fiber samples, much slower than reported values (e.g. 68-89 ns, depending on cerium concentration) for bulk YAG:Ce.

Photoluminescence and scintillation experiments showed effective attenuation lengths ranging from 10-25 cm in five different YAG:Ce fibers. The methodology employed, specifically using continuous laser illumination, is somewhat suspect due to photon pile up saturation; methodology improvements could be made by instead using a pulsed laser. Using scintillation from a 2.4 mm beam of alphas, position-of-interaction resolutions as low as 11 mm were measured in a YAG:Ce fiber using noisy, sub-optimal readout electronics; better shielding is required. Calculations have shown that position resolutions of less than 10 mm are achievable with the current system.

Several improvements to the current detector system are described in this thesis. First, simply replacing the 1600 pixel MPPC with a more efficient model could improve the overall position resolution by a factor of two. Secondly, fiber areas should match the SiPM area in order to maximize optical coupling and reduce the probability of saturation. The SiPM should be chosen to have a balance between dynamic range and efficiency, thereby optimizing the signal amplitude resolution. A formula based on Birks' figure of merit and SiPM parameters has been presented to aid in the selection of the best SiPM (i.e. in terms of smallest value of resolution, R) for a given application. The intrinsic SiPM resolution is given by

$$R = \frac{2.35}{\sqrt{N_{pixels}}}\sqrt{\frac{1}{\alpha}+\frac{\exp(\alpha)-1-\alpha}{\alpha^2 \cdot N_{pixels}}}$$

where (5.1)

$$\alpha = \frac{PDE \cdot \varepsilon_{Fiber} \cdot \tau_{recharge}}{N_{pixels} \cdot \zeta} M$$

where ε_{Fiber} is the trapping efficiency of the fiber, $\tau_{recharge}$ is the recharge time of the pixel, ζ is the integration time in terms of number of scintillator decays (e.g. 5-6), and M is the Birks' figure of merit defined by (2.5).

Although YAG:Ce is mechanically very stable, inexpensive, and easy to grow, other inorganic scintillating fiber materials may be better suited for Compton camera applications. Lutetium based scintillators (e.g. LYSO:Ce or LuAG:Ce) are an obvious choice for improved gamma detection efficiencies. Unfortunately, the intrinsic background from ^{176}Lu decay may prevent implementation in low count rate applications. The rare-earth aluminum perovskite crystals (e.g. YAP:Ce) have higher densities than the chemically similar garnets. They are also much faster and single-component, although less mechanically stable, scintillators (~20-30 ns). Oxyorthosilicates (e.g. LSO:Ce, YSO:Ce, GSO:Ce, and their mixes) are also more efficient and faster scintillators than YAG:Ce. One potentially useful oxyorthosilicate, GSO:Ce, is based on gadolinium which is higher Z than yttrium. Additionally, ^{157}Gd has the highest neutron capture cross-section of any stable nuclide. The 72 keV conversion electrons associated with 39% of the (n,^{157}Gd) reactions could be easily measured in the scintillator. GSO is known to be difficult to grow, cut, and polish. However, the mixture with other rare-earths may stabilize the crystal. Nonetheless, it is a material which should be considered in the detection of SNM, especially in an active interrogation application capable of time discrimination of gamma and neutron interactions.

Garnets are easy to grow and mechanically robust compared to perovskite or oxyorthosilicate oxide crystals. Perhaps, a gadolinium and yttrium mixed aluminum garnet (GdYAG:Ce) could produce a more efficient, combined gamma/neutron

scintillator. However, the anti-site defects associated with the single crystal rare-earth aluminum garnet scintillators form trapping sites which slow the transfer of energy and release charge to activator sites. The result is long scintillation pulses and afterglow. The fluorescence observed in the six YAG:Ce fiber crystal samples show significantly longer alpha scintillation fast decay components than in previous works. This could be a result of the saturation of activator sites, radial dispersion of activator in the region of alpha interaction in μ-PD fiber crystals, or excess Y_{Al} anti-site defects. More study of the properties of rare-earth aluminum garnets is required to isolate the cause of the observed slow scintillation decay in thin fibers.

Finally, the Monte Carlo scintillation photon tracking simulator, Monte Carlo SiPM photon detection simulator, and expanded circuit models developed for SiPMs could be integrated into a single product using a toolkit such as ROOT or GEANT4. This product could model real gamma ray sources and fully simulate the scintillation photon production and detection processes. The output of these simulations could be used to optimize system performances and isolate sources of excess noise.

Despite measuring worse-than-expected energy and position resolutions using dual fiber end MPPC readout of YAG:Ce fibers, the concept of an inorganic scintillating fiber and SiPM based particle tracking calorimeter remains a very promising area of research.

Appendix

A1. LYSO:Ce DETECT2000 Code

```
; DETECT2000 simulation of 1x1x12 mm3 LYSO crystal
; Brad Jones, Thesis, Oct 2010
; Materials:
;LYSO 1.82 ref index, 10-20 cm abs length = 100-200mm, 450 nm peak, 45ns tau
;Attenuation length, AD, increased to test optic theory
DMAT1,1.82NV,2000.AD,450.PLV,1DT,45.TAU

; Finishes and Examples:
DFIN1,PAINT,0.95RC
DFIN2,DETECT,1.46NV,1.QEV,PS

; Geometry:
DPT1,0.X,0.Y,6.Z
DPT2,0.X,0.Y,6.Z
DPT3,1.X,0.Y,0.Z
DPLN1,0.5X
DPLN2,-0.5X
DPLN3,0.5Y
DPLN4,-0.5Y
DPLN5,-6.Z
DPLN6,6.Z

; Components:
COMP1,MAT1
SURF2,FIN1,PLN2,XL
SURF1,FIN1,PLN1,XS
SURF4,FIN1,PLN4,YL
SURF3,FIN1,PLN3,YS
SURF5,FIN1,PLN5,ZL
SURF6,FIN2,PLN6,ZS

; Program Control:
FLAG,0FAST_QE,0VERBOSE
LIFE500.000000
FATES3
PROJ3,PT1,PT2,PT3,X1.001,Y1.001,BINX40,BINY40
TRACE0
;Light created between XS and XL in mm
GEN,MAT1,-0.50000XS,0.50000XL,-0.50000YS,0.500000YL,-6.000000ZS,6.000000ZL

; Program Execution
SEED924
RUN27500
END
```

A2. YAG:Ce DETECT2000 Code

```
; DETECT2000 simulation of 10 cm 400um YAG:Ce fiber crystal
; Brad Jones, Thesis, Oct 2010
; Materials:
;YAG 1.82 ref index, 10-20 cm abs length = 100-200mm, 550 nm peak, 70ns tau
;YAG:Ce alpha decay parameters from Mozynski NIM A398 p290
DMAT1,1.82NV,2000.AD,550.PLV,1DT,88.9TAU,0.149TAUW,458.5TAU,0.851TAUW

; Finishes and Examples:
DFIN1,PAINT,0.RC
DFIN2,POLISH
DFIN3,DETECT,1.46NV,1.QEV,PS

; Geometry:
DPT1,0.X,0.Y,52.Z
DPT2,0.X,0.Y,52.Z
DPT3,1.X,0.Y,0.Z
DPLN1,-51.Z
DPLN2,-50.Z
DPLN3,50.Z
DCYL1,0.200R

; Components:
COMP1,MAT1
SURF1,FIN3,PLN2,ZL
SURF2,FIN3,PLN3,ZS
SURF3,FIN2,CYL1,RS

; Program Control:
FLAG,0FAST_QE,0VERBOSE
LIFE500.000000
FATES3
PROJ3,PT1,PT2,PT3,X1.,Y1.,BINX40,BINY40
TRACE0

;Light created between XS and XL in mm, adjust ZS and ZL to move beam
GEN,MAT1,-0.20000XS,0.2000XL,-0.00000YS,0.000000YL,-0.000000ZS,-0.000000ZL

; Program Execution
SEED924
RUN17000
END
```

A3. YAG:Ce Stopping and Range of Ions in Matter (SRIM)

```
==========================================================
          Calculation using SRIM-2006
          SRIM version ---> SRIM-2008.04
          Calc. date   ---> January 09, 2011
==========================================================
Disk File Name = SRIM Outputs\Helium in  Y-Al- O
Ion = Helium [2] , Mass = 4.003 amu
Target Density =  4.5500E+00 g/cm3 = 9.2316E+22 atoms/cm3
======= Target  Composition ========
  Atom   Atom   Atomic    Mass
  Name   Numb   Percent   Percent
  ----   ----   -------   -------
   Y     39    015.00    044.93
   Al    13    025.00    022.73
   O     8     060.00    032.34
==================================
Bragg Correction = 0.00%
Stopping Units =  MeV / (mg/cm2)
See bottom of Table for other Stopping units

  Ion        dE/dx      dE/dx     Projected  Longitudinal   Lateral
 Energy      Elec.      Nuclear     Range     Straggling   Straggling
------------ ---------- ---------- ----------  ----------  ----------
  1.00 MeV   1.168E+00  1.571E-03   2.20 um     1689 A      2208 A
  1.10 MeV   1.145E+00  1.453E-03   2.38 um     1733 A      2276 A
  1.20 MeV   1.120E+00  1.352E-03   2.58 um     1777 A      2343 A
  1.30 MeV   1.093E+00  1.265E-03   2.77 um     1821 A      2410 A
  1.40 MeV   1.067E+00  1.190E-03   2.98 um     1866 A      2478 A
  1.50 MeV   1.040E+00  1.123E-03   3.18 um     1910 A      2545 A
  1.60 MeV   1.015E+00  1.065E-03   3.40 um     1956 A      2614 A
  1.70 MeV   9.894E-01  1.012E-03   3.61 um     2002 A      2683 A
  1.80 MeV   9.651E-01  9.646E-04   3.84 um     2050 A      2753 A
  2.00 MeV   9.192E-01  8.830E-04   4.30 um     2196 A      2897 A
  2.25 MeV   8.671E-01  7.996E-04   4.91 um     2414 A      3085 A
  2.50 MeV   8.203E-01  7.315E-04   5.56 um     2636 A      3282 A
  2.75 MeV   7.784E-01  6.747E-04   6.25 um     2863 A      3488 A
  3.00 MeV   7.409E-01  6.266E-04   6.97 um     3095 A      3706 A
  3.25 MeV   7.071E-01  5.853E-04   7.72 um     3332 A      3934 A
  3.50 MeV   6.767E-01  5.495E-04   8.51 um     3574 A      4172 A
  3.75 MeV   6.491E-01  5.180E-04   9.34 um     3821 A      4421 A
  4.00 MeV   6.240E-01  4.902E-04  10.20 um      4072 A      4680 A
  4.50 MeV   5.802E-01  4.430E-04  12.02 um      4933 A      5230 A
  5.00 MeV   5.431E-01  4.046E-04  13.97 um      5770 A      5820 A
  5.50 MeV   5.115E-01  3.727E-04  16.05 um      6595 A      6447 A
  6.00 MeV   4.840E-01  3.457E-04  18.25 um      7416 A      7111 A
  6.50 MeV   4.601E-01  3.226E-04  20.58 um      8237 A      7810 A
  7.00 MeV   4.389E-01  3.025E-04  23.01 um      9061 A      8543 A
  8.00 MeV   4.031E-01  2.694E-04  28.23 um      1.19 um     1.01 um
  9.00 MeV   3.748E-01  2.431E-04  33.87 um      1.46 um     1.18 um
 10.00 MeV   3.479E-01  2.217E-04  39.94 um      1.72 um     1.36 um
------------------------------------------------------------
 Multiply Stopping by       for Stopping Units
 -------------------      -------------------
 4.5498E+01                eV / Angstrom
 4.5498E+02               keV / micron
 4.5498E+02               MeV / mm
 1.0000E+00               keV / (ug/cm2)
 1.0000E+00               MeV / (mg/cm2)
 1.0000E+03               keV / (mg/cm2)
 4.9285E+01                eV / (1E15 atoms/cm2)
 4.7856E+00               L.S.S. reduced units
==========================================================
(C) 1984,1989,1992,1998,2008 by J.P. Biersack and J.F. Ziegler
==========================================================
```

Calculation using SRIM-2006
SRIM version ---> SRIM-2008.04
Calc. date ---> January 19, 2011

==========

Disk File Name = SRIM Outputs\Helium in Air, Dry (gas)

Ion = Helium [2] , Mass = 4.003 amu

Target Density = 1.2484E-03 g/cm3 = 5.0794E+19 atoms/cm3
Target is a GAS
======= Target Composition ========

Atom Name	Atom Numb	Atomic Percent	Mass Percent
C	6	000.01	000.01
O	8	023.18	025.06
N	7	075.53	071.48
Ar	18	001.28	003.45

==========
Bragg Correction = 0.00%
Stopping Units = MeV / (mg/cm2)
See bottom of Table for other Stopping units

Ion Energy	dE/dx Elec.	dE/dx Nuclear	Projected Range	Longitudinal Straggling	Lateral Straggling
1.00 MeV	1.873E+00	2.032E-03	5.26 mm	260.84 um	337.31 um
1.10 MeV	1.821E+00	1.875E-03	5.69 mm	269.96 um	344.71 um
1.20 MeV	1.765E+00	1.741E-03	6.14 mm	279.22 um	352.05 um
1.30 MeV	1.709E+00	1.627E-03	6.60 mm	288.69 um	359.42 um
1.40 MeV	1.653E+00	1.527E-03	7.07 mm	298.42 um	366.85 um
1.50 MeV	1.599E+00	1.440E-03	7.57 mm	308.42 um	374.40 um
1.60 MeV	1.548E+00	1.363E-03	8.07 mm	318.72 um	382.10 um
1.70 MeV	1.499E+00	1.294E-03	8.60 mm	329.32 um	389.97 um
1.80 MeV	1.452E+00	1.232E-03	9.14 mm	340.22 um	398.04 um
2.00 MeV	1.368E+00	1.126E-03	10.28 mm	380.20 um	414.82 um
2.25 MeV	1.276E+00	1.017E-03	11.79 mm	441.18 um	437.15 um
2.50 MeV	1.197E+00	9.287E-04	13.41 mm	501.88 um	461.10 um
2.75 MeV	1.129E+00	8.552E-04	15.13 mm	562.71 um	486.73 um
3.00 MeV	1.068E+00	7.931E-04	16.95 mm	623.92 um	514.09 um
3.25 MeV	1.015E+00	7.399E-04	18.87 mm	685.65 um	543.18 um
3.50 MeV	9.680E-01	6.937E-04	20.88 mm	748.00 um	574.02 um
3.75 MeV	9.254E-01	6.533E-04	23.00 mm	811.01 um	606.58 um
4.00 MeV	8.869E-01	6.175E-04	25.21 mm	874.75 um	640.84 um
4.50 MeV	8.196E-01	5.572E-04	29.90 mm	1.11 mm	714.42 um
5.00 MeV	7.626E-01	5.081E-04	34.96 mm	1.33 mm	794.55 um
5.50 MeV	7.136E-01	4.674E-04	40.38 mm	1.55 mm	881.02 um
6.00 MeV	6.710E-01	4.330E-04	46.17 mm	1.76 mm	973.66 um
6.50 MeV	6.334E-01	4.036E-04	52.30 mm	1.97 mm	1.07 mm
7.00 MeV	6.001E-01	3.781E-04	58.79 mm	2.19 mm	1.18 mm
8.00 MeV	5.434E-01	3.361E-04	72.81 mm	2.98 mm	1.40 mm
9.00 MeV	5.021E-01	3.028E-04	88.13 mm	3.70 mm	1.65 mm
10.00 MeV	4.633E-01	2.759E-04	104.73 mm	4.41 mm	1.92 mm

Multiply Stopping by	for Stopping Units
1.2484E-02	eV / Angstrom
1.2484E-01	keV / micron
1.2484E-01	MeV / mm
1.0000E+00	keV / (ug/cm2)
1.0000E+00	MeV / (mg/cm2)
1.0000E+03	keV / (mg/cm2)
2.4577E+01	eV / (1E15 atoms/cm2)
2.1453E+00	L.S.S. reduced units

==========

A4. Source Beam Width Calculations

Alpha Source

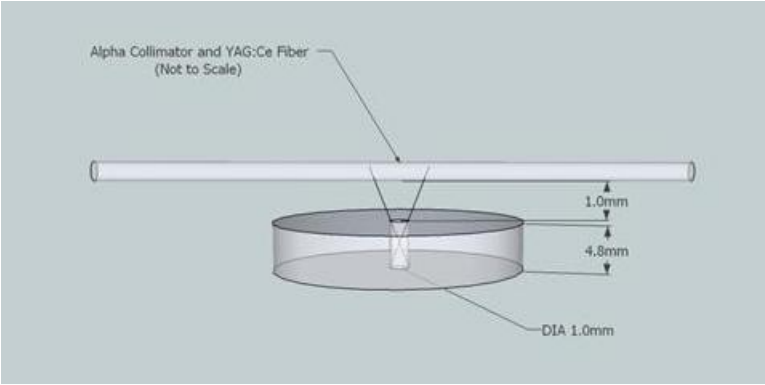

$$\frac{1\,\text{mm}}{4.8\,\text{mm}} = \frac{\text{BW}}{2\times 5.8\,\text{mm}}$$

$$\text{BW} = 2.4\,\text{mm}$$

Laser Source

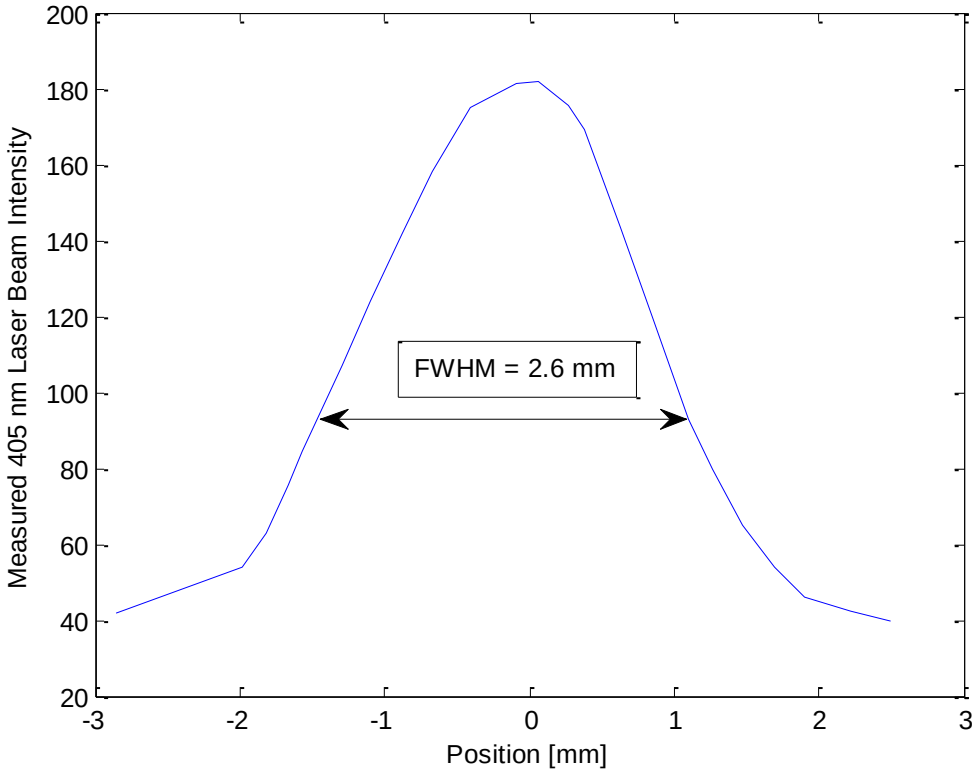

A5. MCNP5 Code

```
Compact Compton Camera Fiber Simulation
c Brad Jones
c 15 Jul 10
c
c Description: This model is of a single .4x100 mm right cylindrical YAG:Ce fiber crystal scintillator for use in the CCC.
c
   1     1  -4.55 -1 imp:p 1
   99    3  -0.0012 -100 1 imp:p 1
  100          0  100 imp:p 0

    1      rcc -5 0 0 10 0 0 .02
  100      rpp -11 11 -10 10 -2 2

mode p
*tr1 0 0 0  0 90 90  90 0 90  90 90 0
c Cerium doped YAG and LYSO
m1 39000 -.449 13000 -.2273 16000 -0.3217 58000 -0.002 $YAG:Ce 0.2% Ce
m2 71000 -0.66 39000 -0.082 16000 -0.066 8000 -.19 58000 -0.002 $LYSO:Ce 80% Lu 0.2% Ce
c Air
m3    6000  -0.000124 7000  -0.755268  8000 -0.231781  18000 -0.012827   $ C N O Ar
c
c 2.6MeV Source Definition
c sdef pos= -7 0 0 par=2 erg=d1 vec=0 -1 0 dir=1
c si1 L 2.6
c sp1 d 1.0

c 511 keV Source Definition
c sdef pos= -7 0 0 par=2 erg=d1 vec=0 -1 0 dir=1
c si1 L 0.511
c sp1 d 1.0
c
c 662 keV Source Definition
sdef pos= -7 0 0 par=2 erg=d1 vec=1 0 0 dir=1
si1 L 0.662
sp1 d 1.0
c
c Doppler Broadening Off
c phys:p 4j 1
NPS 100000000
c
c Tally specification files
f8:p 1
e8 0.0100000000000000            0.0200000000000000 0.0300000000000000
              0.0400000000000000 0.0500000000000000 0.0600000000000000
              0.0700000000000000 0.0800000000000000 0.0900000000000000
              0.100000000000000  0.110000000000000  0.120000000000000
              0.130000000000000  0.140000000000000  0.150000000000000
              0.160000000000000  0.170000000000000  0.180000000000000
              0.190000000000000  0.200000000000000  0.210000000000000
              0.220000000000000  0.230000000000000  0.240000000000000
              0.250000000000000  0.260000000000000  0.270000000000000
              0.280000000000000  0.290000000000000  0.300000000000000
              0.310000000000000  0.320000000000000  0.330000000000000
              0.340000000000000  0.350000000000000  0.360000000000000
              0.370000000000000  0.380000000000000  0.390000000000000
              0.400000000000000  0.410000000000000  0.420000000000000
              0.430000000000000  0.440000000000000  0.450000000000000
              0.460000000000000  0.470000000000000  0.480000000000000
              0.490000000000000  0.500000000000000  0.510000000000000
              0.520000000000000  0.530000000000000  0.540000000000000
              0.550000000000000  0.560000000000000  0.570000000000000
              0.580000000000000  0.590000000000000  0.600000000000000
              0.610000000000000  0.620000000000000  0.630000000000000
              0.640000000000000  0.650000000000000  0.660000000000000
```

0.670000000000000 0.680000000000000 0.690000000000000
0.700000000000000 0.710000000000000 0.720000000000000
0.730000000000000 0.740000000000000 0.750000000000000
0.760000000000000 0.770000000000000 0.780000000000000
0.790000000000000 0.800000000000000 0.810000000000000
0.820000000000000 0.830000000000000 0.840000000000000
0.850000000000000 0.860000000000000 0.870000000000000
0.880000000000000 0.890000000000000 0.900000000000000
0.910000000000000 0.920000000000000 0.930000000000000
0.940000000000000 0.950000000000000 0.960000000000000
0.970000000000000 0.980000000000000 0.990000000000000
1 1.01000000000000 1.02000000000000
1.03000000000000 1.04000000000000 1.05000000000000
1.06000000000000 1.07000000000000 1.08000000000000
1.09000000000000 1.10000000000000 1.11000000000000
1.12000000000000 1.13000000000000 1.14000000000000
1.15000000000000 1.16000000000000 1.17000000000000
1.18000000000000 1.19000000000000 1.20000000000000
1.21000000000000 1.22000000000000 1.23000000000000
1.24000000000000 1.25000000000000 1.26000000000000
1.27000000000000 1.28000000000000 1.29000000000000
1.30000000000000 1.31000000000000 1.32000000000000
1.33000000000000 1.34000000000000 1.35000000000000
1.36000000000000 1.37000000000000 1.38000000000000
1.39000000000000 1.40000000000000 1.41000000000000
1.42000000000000 1.43000000000000 1.44000000000000
1.45000000000000 1.46000000000000 1.47000000000000
1.48000000000000 1.49000000000000 1.50000000000000
1.51000000000000 1.52000000000000 1.53000000000000
1.54000000000000 1.55000000000000 1.56000000000000
1.57000000000000 1.58000000000000 1.59000000000000
1.60000000000000 1.61000000000000 1.62000000000000
1.63000000000000 1.64000000000000 1.65000000000000
1.66000000000000 1.67000000000000 1.68000000000000
1.69000000000000 1.70000000000000 1.71000000000000
1.72000000000000 1.73000000000000 1.74000000000000
1.75000000000000 1.76000000000000 1.77000000000000
1.78000000000000 1.79000000000000 1.80000000000000
1.81000000000000 1.82000000000000 1.83000000000000
1.84000000000000 1.85000000000000 1.86000000000000
1.87000000000000 1.88000000000000 1.89000000000000
1.90000000000000 1.91000000000000 1.92000000000000
1.93000000000000 1.94000000000000 1.95000000000000
1.96000000000000 1.97000000000000 1.98000000000000
1.99000000000000 2 2.01000000000000
2.02000000000000 2.03000000000000 2.04000000000000
2.05000000000000 2.06000000000000 2.07000000000000
2.08000000000000 2.09000000000000 2.10000000000000
2.11000000000000 2.12000000000000 2.13000000000000
2.14000000000000 2.15000000000000 2.16000000000000
2.17000000000000 2.18000000000000 2.19000000000000
2.20000000000000 2.21000000000000 2.22000000000000
2.23000000000000 2.24000000000000 2.25000000000000
2.26000000000000 2.27000000000000 2.28000000000000
2.29000000000000 2.30000000000000 2.31000000000000
2.32000000000000 2.33000000000000 2.34000000000000
2.35000000000000 2.36000000000000 2.37000000000000
2.38000000000000 2.39000000000000 2.40000000000000
2.41000000000000 2.42000000000000 2.43000000000000
2.44000000000000 2.45000000000000 2.46000000000000
2.47000000000000 2.48000000000000 2.49000000000000
2.50000000000000 2.51000000000000 2.52000000000000
2.53000000000000 2.54000000000000 2.55000000000000
2.56000000000000 2.57000000000000 2.58000000000000
2.59000000000000 2.60000000000000 2.61000000000000
2.62000000000000 2.63000000000000 2.64000000000000
2.65000000000000 2.66000000000000 2.67000000000000
2.68000000000000 2.69000000000000 2.70000000000000

A6. YAG:Ce Alpha Decay Profile Data

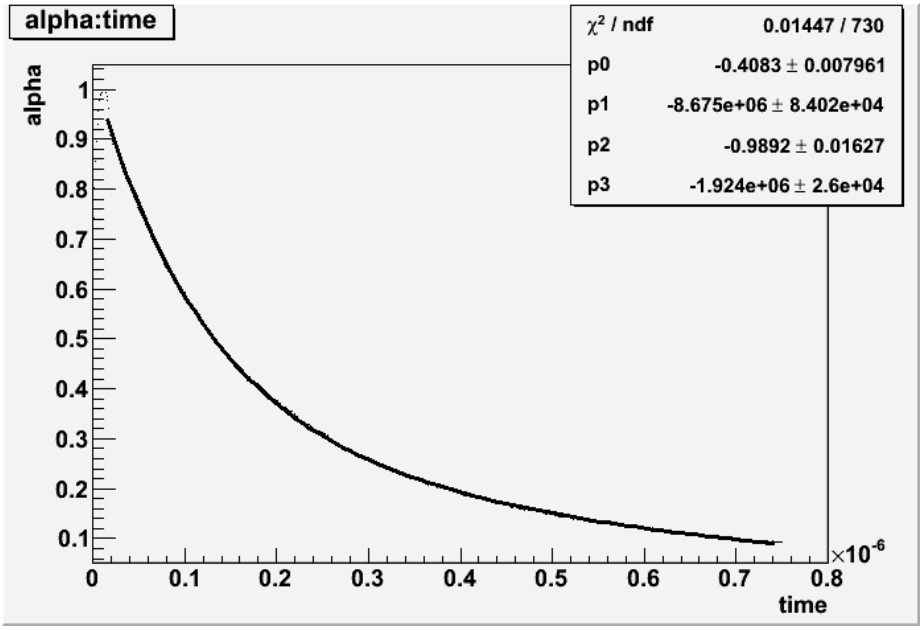

Fiber F1 decay profile data and ROOT two exponential decay fitting parameters.

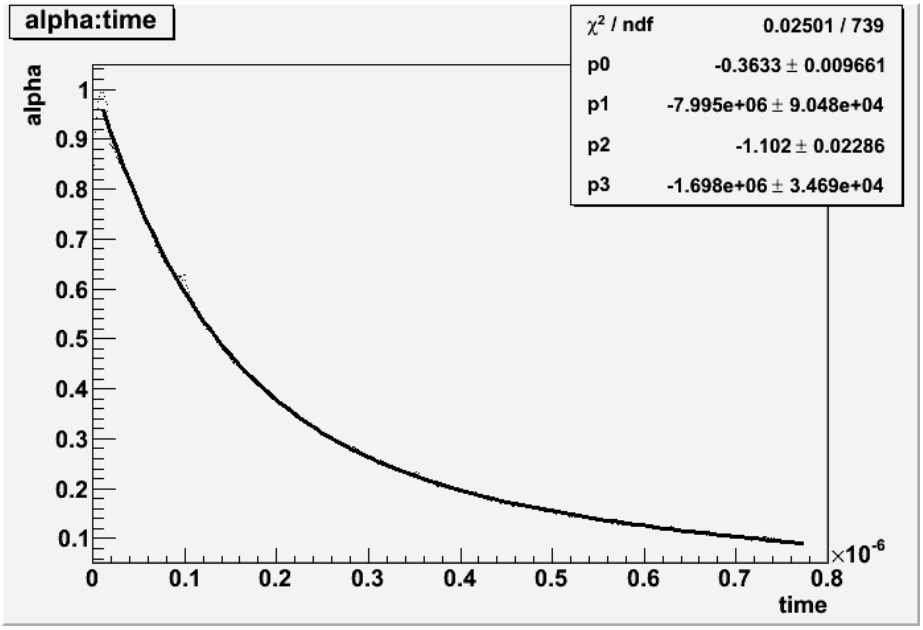

Fiber F2 decay profile data and ROOT two exponential decay fitting parameters.

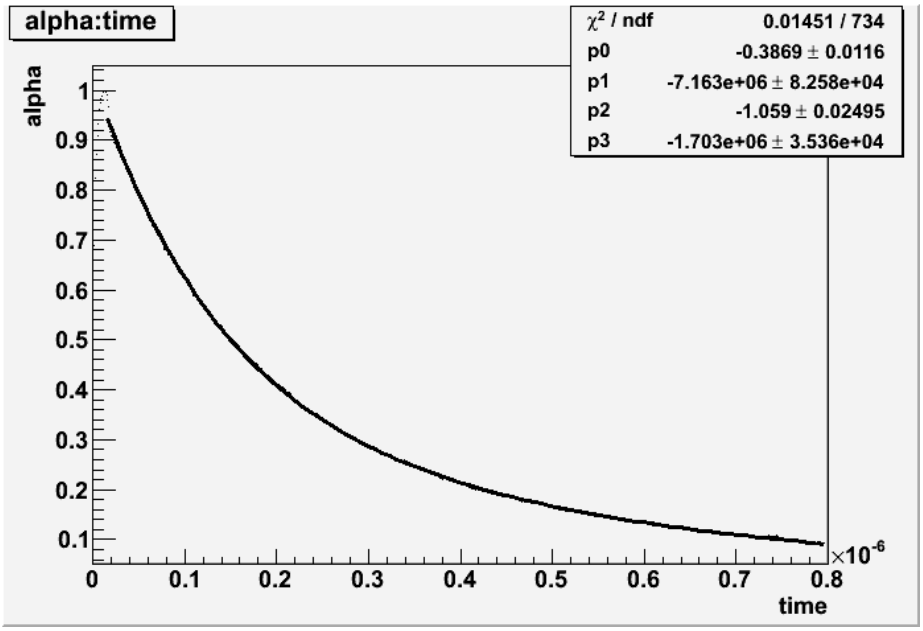

Fiber F3 decay profile data and ROOT two exponential decay fitting parameters.

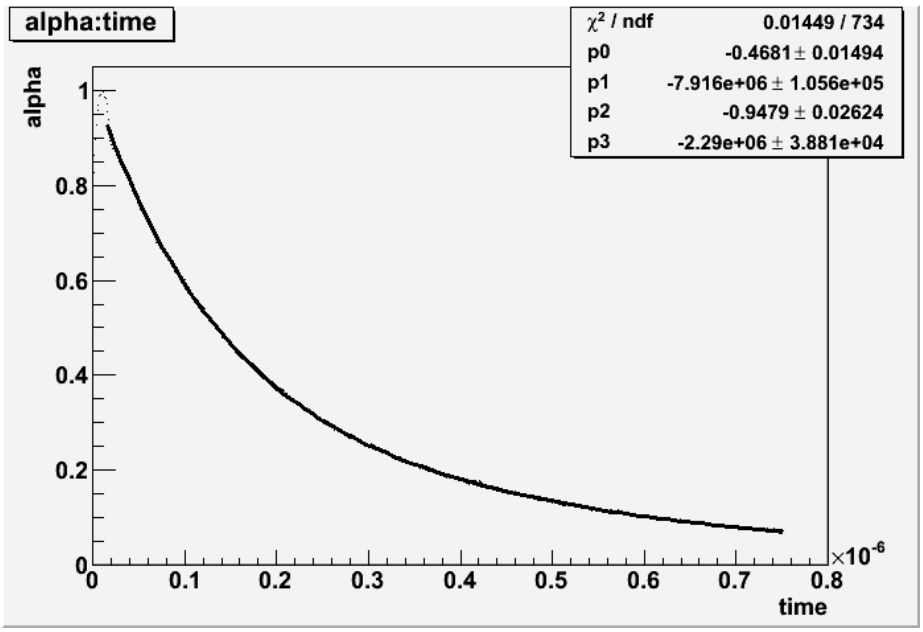

Fiber F4 decay profile data and ROOT two exponential decay fitting parameters.

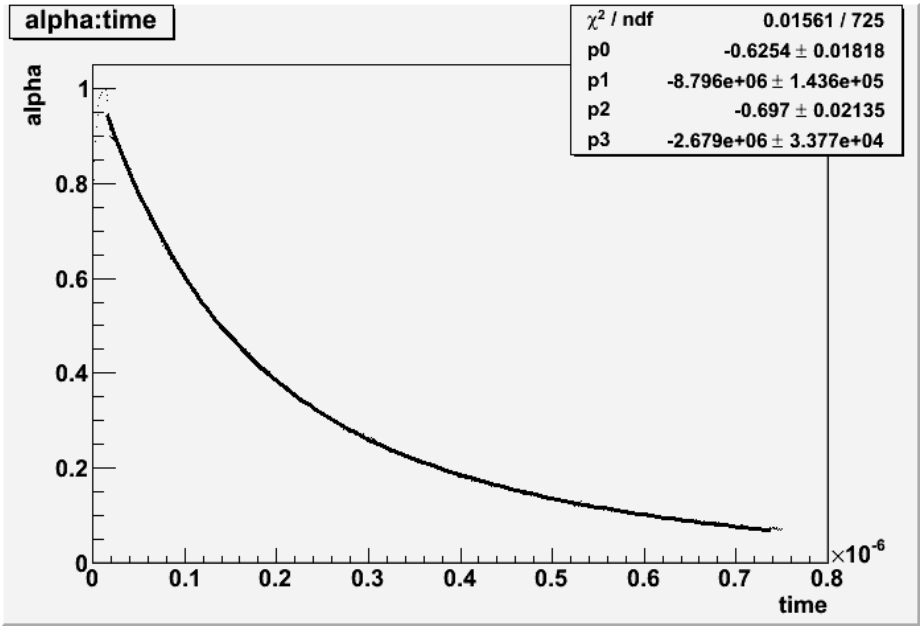

Fiber F5 decay profile data and ROOT two exponential decay fitting parameters.

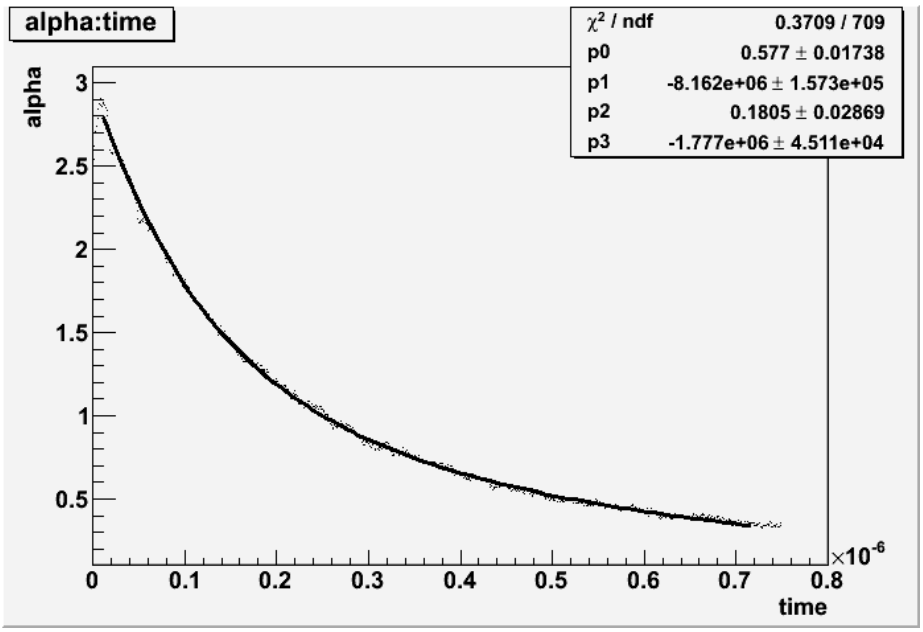

Fiber F6 decay profile data and ROOT two exponential decay fitting parameters.

Bibliography

[1] United States Department of Defense, "Nuclear Posture Review," April 2010.

[2] Guangzhi Sun and Ximeng Chen, "Development of a type of a one-dimensional position-sensitive scintillator– fiber detector for X-ray backscatter imaging," *Nuclear Instruments and Methods in Physics Research*, vol. A 594 , pp. 61– 65, June 2008.

[3] Fibercryst. (2010, May) Scintillating Fiber Products. [Online]. http://www.fibercryst.com/product_details.php?id=345&product_name=Scintillating+fibers

[4] Masahiro Teshima and Caroline Terquem, "Study of Silicon Photomultipliers," Max Planck Institute for Physics, 2004.

[5] Gene Aloise, "Recent Testing Raises Issues About the Potential Effectiveness of Advanced Radiation Detection Portal Monitors," General Accounting Office, 2009.

[6] Carolyn Lehner, "4-Pi Compton Imaging Using a Single 3-D Position Sensitive CdZnTe Detector," University of Michigan, 2004.

[7] Carolyn Lehner, "4-Pi Compton Imaging Using a Single 3-D Position Sensitive CdZnTe Detector," University of Michigan, Ann Arbour, MI, Dissertation 3139215, 2004.

[8] Glenn Knoll, *Radiation Detection and Measurement*, 3rd ed. New York: John Wiley & Sons, 2000.

[9] A. Zoglauer, R. Andritschke, and G. Kanbach, "Image Reconstruction for the MEGA Telescope," Max Planck Institute for Extraterrestrial Physics, Garching, Germany, 2004.

[10] Piotr A Rodnyi, *Physical Processes in Inorganic Scintillators*. Boca Raton, FL: CRC Press, 1997.

[11] D. R. Vij, *Luminescence of Solids*. New York, USA: Plenum Press, 1998.

[12] M. Nikl, A. Vedda, and V.V. Laguta, "Energy Transfer and Storage Processes in Scintillators: The Role and Nature of Defects," *Elsevier*, vol. 42, pp. 509-514, 2007.

[13] Yu Zorenko, et al., "Time-resolved luminescent spectroscopy of YAG:Ce single crystal and single crystalline films," *Elsevier*, vol. 45, pp. 395-397, 2010.

[14] D. E. Persyk, et al., "Research on pure sodium iodide as a practical scintillator," *IEEE Trans. on Nucl. Sci.*, vol. NS-27, pp. 168-171, Feb 1980.

[15] Martin Nikl, "Scintillation detectors for x-rays," *Institute of Physics Publishing*, vol. 17, pp. R37-R54, Feb 2006.

[16] P. Iredale, "The effect of the nonproportional response of NaI(Tl) crystals to electrons upon the resolution for gamma rays," *Nucl. Instrum. Methods*, vol. 82, p. 269, 1961.

[17] P. Dorenbos, J. T. M. de Haas, and C. W. E. van Eijk, "Non-Proportionality in the

Scintillation Response and the Energy Resolution Obtainable with Scintillation Crystals," *IEEE Trans. on Nucl. Sci.*, vol. 42, no. 6, pp. 2190-2202, December 1995.

[18] M. Balcerzyk, et al., "Intrinsic energy resolution and nonlinearity of some contemporary scintillators," Soltan Institute for Nuclear Studies, Otwock, Poland,.

[19] M. Balcerzyk, M. Moszynski, and M. Kapusta, "Energy resolution of contemporary scintillators. Quest for high resolution, proportional detector," Soltan Institute for Nuclear Studies, Otwock, Poland,.

[20] E. Zych, C. Brecher, and J. Glodo, "Kinetics of cerium emission in a YAG:Ce single crystal: the role of traps," *J. Phys.: Condens. Matter*, vol. 12, pp. 1947-1958, 2000.

[21] Philippe Anfré, "Localisation des interactions de rayonnements ionisants sur des fibres monocristallines scintillatrices," University of Lyon, Lyon, France, PhD Thesis 2007.

[22] I. Vilardi, et al., "Optimization of the effective light attenuation length of YAP:Ce and LYSO:Ce crystals for a novel geometrical PET concept," *Nuclear Instruments and Methods*, vol. A564, no. 1, pp. 506-514, August 2006.

[23] Saint-Gobain. (2010, February) Saint-Gobain Scintillation Products. [Online]. http://www.detectors.saint-gobain.com/

[24] A. Ferrer, et al., "Study of very long scintillating fiber TOF detector. Application to the Tau-Charm-Factory," *Nuclear Instruments and Methods in Physics Research Section A*, vol. 371, no. 3, pp. 397-405, March 1996.

[25] M. Kuhlen, "Timing properties of long scintillation counters based on scintillating fibers," *Nuclear Instruments and Methods in Physics Research Section A*, vol. 301, no. 2, pp. 223-229, March 1991.

[26] CERN. (2011, Jan) GEANT4 User Guide. [Online]. http://geant4.web.cern.ch/geant4/G4UsersDocuments/UsersGuides/ForApplicationDeveloper/html/index.html

[27] G. Menzer, "Die Kristallstruktur von Granat," *Z. Kristallogr*, vol. 63, pp. 157-158, 1926.

[28] Tsuguo Fukada and Valery I. Chani, *Shaped Crystals: Growth by Micro-Pulling-Down Technique*. New York, USA: Springer Berlin Heidelberg, 2007.

[29] M. M. Kuklja, "Defects in yttrium aluminium perovskite and garnet crystals; atomistic study.," *J. Phys. Condens Matter*, vol. 12, pp. 2953-2967, 2000.

[30] M. Moszynski, et al., "Properties of the YAG:Ce scintillator," *Nuclear Instruments and Methods*, vol. A 345, pp. 461-467, 1994.

[31] C. W. E. van Eijk, et al., "Ce3+ doped inorganic scintillators," *Nuclear Instruments and Methods*, vol. A 348, pp. 546-550, 1994.

[32] T. Ludziejewski, et al., "Investigation of some scintillation properties of YAG:Ce crystals," *Nuclear Instruments and Methods*, vol. A 398, pp. 287-294, 1997.

[33] F. A. Selim, et al., "Identification of defects in Y3Al5O12 crystals by positron

annihilation spectroscopy," *Applied Physics Letters*, vol. 91, no. 10, 2007.

[34] W. Chewpraditkul, "Scintillation Properties of LuAG:Ce, YAG:Ce and LYSO:Ce Crystals for Gamma-Ray Detection," *IEEE Trans. on Nucl. Sci.*, vol. 56, no. 6, pp. 3800-3805, Dec 2009.

[35] S. Baccaro, et al., "Scintillation properties of YAP:Ce," *Nuclear Instruments and Methods*, vol. A 361, pp. 209-215, 1995.

[36] Philippe Anfre, et al., "Evaluation of Fiber-Shaped LYSO for Double Readout Gamma Photon Detection," *IEEE Trans. on Nucl. Sci.*, vol. 54, no. 2, pp. 391-397, April 2007.

[37] James E. Turner, *Atoms, Radiation, and Radiation Protection*, 2nd ed. New York City, USA: Wiley-Interscience, 1995.

[38] Didier Perrodin. (2010, Nov) Email Correspondence.

[39] Rayko Simura, Akira Yoshikawa, and Satoshi Uda, "The radial distribution of dopant (Cr, Nd, Yb, or Ce) in yttrium aluminum garnet (Y3Al5O12) single crystals grown by the micro-pulling-down method," *Journal of Crystal Growth*, vol. 311, pp. 4763-4769, 2009.

[40] C. Dujardin, et al., "LuAG:Ce fibers for high energy calorimetry," *Journal of Applied Physics*, vol. 108, pp. 013510:1-7, 2010.

[41] D. Schlyer, et al., "Development of a simultaneous PET/MRI scanner," in *IEEE Nuclear Science Symposium*, 2004, pp. 3419-3421.

[42] Kristen A. Wangerin, et al., "Passive Electrical Model of Silicon Photomultipliers," in *IEEE Nuclear Science Symposium*, 2009, pp. 4906-4913.

[43] F. Corsi, et al., "Modelling a silicon photomultiplier (SiPM) as a signal source for optimum front-end design," *Nuclear Instruments and Methods*, vol. 572, no. 1, pp. 416-418, March 2007.

[44] Stefan Seifert, et al., "Simulation of Silicon Photomultiplier Signals," *IEEE Trans. on Nucl. Sci.*, vol. 56, no. 6, pp. 3726-3723, Dec 2009.

[45] Hamamatsu. (2010, May) Silicon Photomultiplier Series. [Online]. http://sales.hamamatsu.com/en/products/solid-state-division/si-photodiode-series/mppc.php

[46] SensL. (2010, May) SensL Products. [Online]. http://sensl.com/products/silicon-photomultipliers/spmarray4/

[47] N. Pavlov, et al., "Gamma spectroscopy using a silicon photomultiplier and a scintillator," in *IEEE Nuclear Science Symposium*, 2005, pp. 173-180.

[48] A. Stoykov, et al., "On the limited amplitude resolution of multipixel Geiger-mode APDs," *Institute of Physics*, June 2007.

[49] P. Buzhan, et al., "An Advanced Study of Silicon Photomultiplier," *ICFA Instrumentation Bulletin*.

[50] Erik B. Johnson, et al., "Energy Resolution in CMOS SSPM Detectors Coupled to an LYSO Scintillator," *IEEE Trans. on Nucl. Sci.*, vol. 56, no. 3, pp. 1024-1032, June 2009.

[51] Cadence Design Systems. (2010, November) Orcad Capture PSPICE v16.3 Student Version. Windows Executable.

[52] L. Pidol, et al., "High efficiency of lutetium silicate scintillators, Ce-doped LPS, and LYSO crystals," *IEEE Trans. on Nucl. Sci.*, vol. 51, no. 3, pp. 1084-1087, June 2004.

[53] C. Moisan, F. Cayouet, and G. McDonald, "DETECT2000: The Object Oriented C++ Language Version of DETECT, A Program for Modeling Optical Properties of Scintillators," Department of Electrical and Computer Engineering, Laval University, Quebec City, Quebec, Canada, 2000.

[54] C. Moisan, F. Cayouet, and G. McDonald, "DETECT2000: The Object Oriented C++ Language Version of DETECT; A Program for Modeling Optical Properties of Scintillators," Laval University, Quebec City, Quebec, Canada, User's Manual 2000.

[55] NIST. (2010, Dec) NIST ASTAR. [Online]. http://physics.nist.gov/PhysRefData/Star/Text/ASTAR.html

[56] James Ziegler. (2011, February) Particle Interactions with Matter. [Online]. www.srim.org

[57] The ROOT Team. (2011, February) ROOT: An Object-Oriented Data Analysis Framework. [Online]. root.cern.ch

[58] M. Moszynski, et al., "Large Size LSO:Ce and YSO:Ce Scintillators for 50 MeV Range Gamma Ray Detector," Soltan Institute for Nuclear Studies, Swierk-Otwock, Poland,.

[59] Omega Piezo. (2011, Jan) Omega Piezo Crystal Scintllators. [Online]. http://www.omegapiezo.com/crystal_scintillators.html

[60] Proteus Crystals. (2011, Jan) LYSO from Proteus. [Online]. http://www.apace-science.com/proteus/lyso.htm#top

[61] D.J. van der Laan, et al., "Using Cramer-Rao Theory Combined with Monte Carlo Simulations for the Optimization of Monolithic Scintillator PET Detectors," *IEEE Trans. on Nucl. Sci.*, vol. 53, no. 3, pp. 1063-1070, June 2006.

[62] G. Hull, et al., "Light collection optimization in scintillator-based gamma-ray spectrometers," *Nuclear Instruments and Methods*, vol. A588, pp. 384-388, 2008.

[63] S.R. Chery, et al., "Collection of scintillation light from small BGO crystals," *IEEE Trans. on Nucl. Sci.*, vol. 42, no. 4, pp. 1058-1063, Aug 1995.

[64] Paul Barton, et al., "Scintillator Geometry and Surface Treatment for Readout by a Small Area Silicon Photomultiplier," in *IEEE Nuclear Science Symposium Conference Record*, 2007, pp. N24:122-127.

[65] E. Mihokova, et al., "Luminescence and scintillation properties of YAG:Ce single crystal and optical ceramics," *Journal of Luminescence*, vol. 126, pp. 77-80, June 2006.

[66] E. Zych, et al., "Luminescence properties of Ce-activated YAG optical ceramic scintillator materials," *Journal of Luminescence*, vol. 75, pp. 193-203, 1997.

[67] Monte Carlo Codes Group - Los Alamos National Laboratory. (2011, February) MCNP - A General Monte Carlo N-Particle Transport Code Version 5. [Online]. mcnp-green.lanl.gov

[68] Sherbrooke University Department of Electrical and Computer Engineering. (2011, February) CASINO: monte CArlo SImulation of electroN trajectories in sOlids. [Online]. http://www.gel.usherbrooke.ca/casino/index.html

[69] Dominique Drouin, et al., "CASINO V2.42 - A Fast and Easy-to-use Modeling Tool for Scanning Electron Microscopy and Microanalysis Users," *Scanning*, vol. 29, pp. 92-101, 2007.

[70] J. B. Birks, *The Theory and Practice of Scintillation Counting*. Oxford: Pergamon Press, 1964.

[71] Kelly Rakes, "Evaluating the Response of Polyvinyl Toluene Scintillators Used in Portal Detectors," Air Force Institute of Technology, Masters Thesis 2008.

[72] C. L. Melcher and J. S. Schweitzer, "A promising new scintillator: Cerium doped lutetium oxyorthosilicate," *Nucl. Instrum. Methods Phys. res.*, no. A314, p. 212, 1992.

[73] "Crystal Growth and Scintillation Properties of Strontium Iodide Scintillators," *IEEE Trans. on Nucl. Sci.*, vol. 56, no. 3, pp. 869-872, June 2009.

[74] Paul Barton, et al., "Effect of SSPM surface coating on light collection efficiency and optical crosstalk for scintillation detection," *Nuclear Instruments and Methods in Physics Research A*, vol. A610, pp. 393-396, 2009.

[75] NIST. (2010, Dec) ESTAR. [Online]. http://physics.nist.gov/PhysRefData/Star/Text/ESTAR.html

[76] A. Nassalski, et al., "Multi Pixel Photon Counters (MPPC) as an Alternative to APD in PET Applications," *IEEE Transactions on Nuclear Science*, vol. 57, no. 3, pp. 1008-1014, June 2010.

REPORT DOCUMENTATION PAGE			*Form Approved OMB No. 074-0188*

1. REPORT DATE *(DD-MM-YYYY)*	2. REPORT TYPE	3. DATES COVERED *(From – To)*
24-03-2011	Master's Thesis	June 2010 – March 2011

TITLE AND SUBTITLE	5a. CONTRACT NUMBER
Investigation of YAG:Ce Scintillating Fiber Properties Using Silicon Photomultipliers	5b. GRANT NUMBER
	5c. PROGRAM ELEMENT NUMBER
AUTHOR(S)	5d. PROJECT NUMBER
Jones, Bradley S., 1st Lt USAF	5e. TASK NUMBER
	5f. WORK UNIT NUMBER

7. PERFORMING ORGANIZATION NAMES(S) AND ADDRESS(S)	8. PERFORMING ORGANIZATION REPORT NUMBER
Air Force Institute of Technology Graduate School of Engineering and Management (AFIT/ENP) 2950 Hobson Way, Building 640 WPAFB OH 45433-8865	AFIT/GNE/ENP/11-M11
9. SPONSORING/MONITORING AGENCY NAME(S) AND ADDRESS(ES) Mr. William Ulicny DHS/DNDO 245 Murray Dr B410 Washington D.C., 20528	10. SPONSOR/MONITOR'S ACRONYM(S) DHS 11. SPONSOR/MONITOR'S REPORT NUMBER(S) HSHQDC-08-X-00641

12. DISTRIBUTION/AVAILABILITY STATEMENT
APPROVED FOR PUBLIC RELEASE; DISTRIBUTION UNLIMITED.

13. SUPPLEMENTARY NOTES

14. ABSTRACT
The properties of thin, cerium activated, yttrium aluminum garnet (YAG:Ce), scintillating fiber-shaped crystals were investigated for particle tracking and calorimetric applications such as Compton imaging of Special Nuclear Material from remote platforms at standoff ranges. Silicon photomultipliers (SiPMs) are relatively new, efficient, single photon sensitive, solid-state photodiode arrays which are well suited for the readout of scintillating fibers. Using SiPMs, the scintillation decay time profiles of six 400 μm YAG:Ce fiber crystals were measured under alpha and gamma irradiation. Interestingly, the observed decay times in the thin fibers were substantially slower than values for bulk single crystal YAG:Ce reported in open scientific literature; possible explanations are explored. Both laser induced photoluminescence and alpha scintillation measurements were conducted to estimate the effective attenuation length of the YAG:Ce fibers. Using the measured attenuation lengths, position-of-interaction measurements were conducted to determine the achievable position resolution in YAG:Ce fibers using dual fiber end SiPM readouts. The measured results are compared to theoretical calculations and Monte Carlo simulations. Finally, improvements to the detector concept, including a formula to determine the best SiPM model based on device parameters and the Birks' figure of merit of the scintillating material, are presented.

15. SUBJECT TERMS
Scintillating fibers; YAG:Ce single crystal fibers; Silicon Photomultipliers

16. SECURITY CLASSIFICATION OF:			17. LIMITATION OF ABSTRACT	18. NUMBER OF PAGES	19a. NAME OF RESPONSIBLE PERSON
a. REPORT	b. ABSTRACT	c. THIS PAGE			Benjamin Kowash, Maj, USAF ADVISOR
U	U	U	UU	197	19b. TELEPHONE NUMBER *(Include area code)* (937) 255-3636, ext 4571 (benjamin.kowash@afit.edu)

Standard Form 298 (Rev. 8-98)
Prescribed by ANSI Std. Z39-18